UNIVERSITÀ DELLA CALABRIA

UNIVERSITA' DELLA CALABRIA

Dipartimento di Ingegneria Informatica, Modellistica, Elettronica e Sistemistica
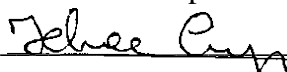
Dottorato di Ricerca in
Information and Communication Engineering For Pervasive Intelligent Environments

CICLO
XXIX

mm-Wave Antennas For Satellite And Mobile Communications

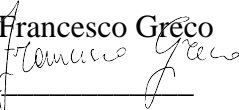**Settore Scientifico Disciplinare Campi Elettromagnetici**

Coordinatore: Ch.mo Prof. Felice Crupi

Firma _____

Supervisore/Tutor: Ch.mo Prof. Giandomenico Amendola

Firma_____

Dottorando: Dott. Francesco Greco

Firma_____

List of figures

List of Acronyms

Fixed Satellite Service	**FSS**
Mobile Satellite Service	**MSS**
Broadcasting Mobile Satellite Service Satellite Service	**BSS**
Earth Exploration Satellite Service	**ESS**
Space Research Service	**SRS**
Space Operation Service	**SOS**
Radiodetermination Satellite Service	**RSS**
Inter-Satellite Service	**ISS**
Amateur Satellite Service	**ASS**
International Telecomunication Union	**ITU**
Direct-to-Home	**DTH**
Global Positioning System	**GPS**
Maximum usable frequency	**MUF**
Optimum Working Frequency	**OWF**
Low-Earth-Orbit	**LEO**
Medium-Earth-Orbit	**MEO**
Geostationary-Earth-Orbit	**GEO**
Satcom-On-the-Move	**SOTM**
Carrier-to-noise-ratio	**CI**
Adjacent Satellete Interference	**ASI**
Equivalent Isotropic Radiated Power	**EIRP**
Local Area Network	**LAN**
High Frequency Structure Simulator	**HFSS**

Abstract

Ever growing demands for higher data rate and bandwidth are pushing wireless applications to millimetre-wave band (3-300GHz), where sufficient bandwidth is available and high performance can be achieved without using complex modulation systems. In addition to Telecom applications, millimetre-wave bands has enabled novel short range and long range radar sensors for automotive as well as high resolution imaging systems for medical and security. The major obstacle for the wide deployment of commercial wireless and radar systems in this frequency range is the high cost of the overall system. The main object of this work is to investigate and to develop different type of antenna that could be applied in satellite communications, in the future fifth generation of mobile networks and on radar automotive systems. In particular, in the present thesis, four antennas have been developed.

A dual band dual polarized antenna array for Satcom-On-The-Move application that gives the possibility to obtain a fixed beam on the frequency range 19-21GHz (Rx band) and 29-31GHz (Tx band). This structure could be used in association with a fully mechanical pointing system.

A Reflector terminal in the Q/V bands that could be use on the backhaul point of the 5G future architecture. A Ka band scaled version of the antenna has been realized and measured proving that it can be a valid solution for compact earth terminals. A novel reflectarray with potential applications in both satellite communications and high speed point-to-point radio links.

Finally, a 77GHz transmit-array antenna mounted on a QFN package. This kind structure, due to the compact dimensions, could be represent a possible solution for automotive radar system.

1. Antenna Needs for future Applications at Millimeter Waves

The main factor that influences the adoption of frequency bands up to mm-wave is the available spectrum. In fact, the always increasing volume of data to be exchanged calls for larger and larger bandwidth which are available only in high frequency ranges. For this reason the spectrum of frequency called millimetre wave (>30GHZ) is currently being studied and used in new, high performance data links. The list of applications which rely on millimetre wave band is already long. Satellite communications at K/Ka occupies from 17.7GHz to 21.2GHz in RX and from 27.5GHz to 31GHz in TX mode. Band around 40GHz is typically used for cellular backhaul and long-distance links, providing data rates that are in the range of several hundred Mb/s. Gb/s data rates, have been realized at 60GHz, 70GHz an 80GHz in system currently available. Other than communications applications, millimetre waves have found applications in automotive radars that operate in the band 76GHz-77GHz for long range radars while the band 77GHz-81GHz is allocated to short-range radar.

In this chapter is presented a brief description of the applications for which the antennas presented in the following parts of this thesis have been designed. The description, rather than exhaustive, focus on a few aspects that are considered critical in the design phase.

1.1. Satcom on The Move (K/Ka- band)

In addition to Ku-band, Ka-band is nowadays available in the following frequency ranges: 27.5 to 31.0GHz uplink and 17.7 to 21 GHz downlink For this band, new design solutions and technologies, adopted by terminal equipment manufacturers, allowed the development of more spectrally efficient, ultra-small terminals that can provide broadband. This is true for both mobile (Satcom On The Move) and fixed applications. The design of antennas for satellite communications have to satisfy several requirements. In general, they have to provide TX and RX operations, support circular polarization (if required) and to be efficient to satisfy the requirements on the radiated EIRP and G/T. Another important specification is relevant to the unwanted interference towards adjacent satellites (ASI-Adjacent Satellite Interference), which is expressed in terms of power spectral density masks within which the power radiated by the antenna has to stay.

Technical and operational characteristics for Satcom on the Move are different from those of fixed satellite communications. One of the most important, is the small antenna size that is necessary to operate from a moving vehicle, aircraft or vessels. A small size is mandatory because the antenna has to be mounted on a tracking system that is required to maintain accurate pointing to the target satellite at all times. However, as vehicles move, there is always a probability that antenna-pointing errors may occur for small fractions of time, thus leading to an increase of interference toward other co-frequency neighbouring satellites or other radio-systems. This possibility requires that systems have to be designed and operated rigorously to minimize interference and comply with established regulations. As it was already stated, the reduction of interfering signals towards adjacent satellite is a fundamental issue. Early satellite communications systems

utilized rather large earth terminal antennas with very high discrimination to and from adjacent satellite. SOTM terminal are so small that they have exactly the opposite effect. In fact, the small aperture size offers relatively large beam-width towards the satellite of interest and simultaneously radiate a significant amount of energy towards adjacent satellite [1].

The need of compact antenna is not limited to SOTM applications. In fact, there are applications calling for fixed earth terminals with a reduced size. This is the case of man transportable terminal used in defence and security applications which are normally carried by a single operator in difficult conditions. The design of such antennas shares many difficulties with the design of SOTM radiators. In particular, as in the SOTM case, they have to provide dual band operations, comply with radiation masks to avoid interference on the adjacent satellites and to be efficient to satisfy the requirements on the radiated EIRP and G/T.

In the following chapters two antennas will be presented that have the potential to satisfy the requirements discussed previously: a printed antenna with dual band (19-21GHz and 29-31GHz) capabilities for TX/RX operations and two polarizations per band; a compact low profile reflector TX/RX antenna which complies with power density masks. As a further study the potential use of a reflectarray based antenna has been evaluated.

1.2.   High speed Millimeter Waves link

The problem of providing the EIRP calculated by link budgets and, at the same time to radiate into the prescribed Power Density Masks, is not limited to satellite communications but has to be faced also in the design of antennas for point-to-point terrestrial radio link. The availability of high- speed radio links is fundamental

for the operation of the current mobile networks and it will be even more important in the future systems (5g). In fact, the current fourth generation for mobile communications already uses advanced technology, such as orthogonal frequency division multiplexing (OFDM) or multiple input multiple output (MIMO), in order to achieve spectral efficiency close to theoretical limits in terms of bits per second per Hertz per cell [2]. One possibility to increase the capacity per geographic area is to deploy many smaller cells such as femtocells and heterogeneous networks. However, because capacity can only scale linearly with the number of cells, small cells alone will not be able to meet the capacity required to accommodate an increase of orders of magnitude in mobile data traffic as required by new applications. In this case, the only option is to recur to millimetre waves base stations (MMB). In order to ensure good coverage base stations at millimetre waves need to be deployed with higher density than macro-cellular base stations. The transmission and reception in an MMB system are based on narrow beams, which suppress the interference from neighbouring MMBs and extend the range of an MMB link. This allows significant overlap of coverage among neighbouring base stations. Unlike cellular systems that partition the geographic area into cells with each cell served by one or a few base stations, the MMBs form a grid with a large number of nodes to which a mobile station can attach. This possible solution has the advantage to eliminate the problem of poor link quality at the cell edge that is inherent in cellular system and enables high-quality equal grade of service. However, the main disadvantages is that MMB have to be networked between them and to the overall system with high speed links. To avoid the considerable costs of a system based on optical fibers, a network of point-to-point radio links may prove an effective solution. For this reason, it is possible to forecast that a growing number of high speed point to

point links will be deployed in the future. This will push more attention on low cost, efficient mmw antennas able to comply with regulations on power density masks. In this thesis, the compact antenna design already mentioned in the previous section is adopted to design a Q/V band antenna for high speed point-to-point link.

1.3.   Radar automotive applications

The focal point of the next generation of wireless and sensing systems is to obtain a reconfigurable antenna beam forming. High gain pencil-beam or multi-beam synthesis is essential to many systems including satellite communications, cellular base stations, remote sensing, point-to-point terrestrial links, deep-space communication links and radars automotive. Focusing the attention on radar automotive applications, this sector will reach an inflection point which the control of vehicles, in a not too distance future, radars will be used in lane, blind spot detection, adaptive cruise control, collision warning and pedestrian detection. It is projected that by the year 2020, traffic congestion in many cities around the world will reach unresolvable levels unless vehicles incorporate autonomous control to coordinate the movements for optimum traffic flow. The frequency band of 77GHz has proven to be attractive of automotive radar-based safety applications, including for adaptive cruise control, blind-spot detection, emergency braking, forward collision warning and rear collision protection are some automotive applications, which are based on high performance radar sensors. A conventional approach to realize beam scanning radar sensor is to use phased array antennas. They provide electronic flexibility in exciting the elements, allowing for reconfiguration and scanning of the beam pattern in real

time. Although phased array antennas are capable of providing a wide beam steering angle, the disadvantage is that each array element needs to be connected to a dedicate transceiver module. Furthermore, phased arrays diminish in efficiency at millimetre-wave frequencies due to use of transmission-line feeding networks which become increasingly loss at high frequencies and also phased arrays have the drawbacks of high costs and bulky structure.

 In the last chapter of this thesis is presented the design of a highly integrated transmitarray antenna at 77GHz which is conceived to give a low cost solution for the new generation of automotive radars.

2. A Dual Band, Dual Polarized array for Ka band Satcom on the Move terminals

2.1. State of the art

During the recent years, a large numbers of terminals for Satcom-On the Move applications were studied and produced. This kind of terminals must to be able to operate in regions with undeveloped infrastructure, distant from big cities, but still in areas of satellites services. Key element of the SOTM terminal is antenna which should have to satisfy the following restrictions [3] :

- A narrow beam to receive/transmit wideband signals from/to the satellite

- Satellite tracking capabilities for SOTM operation

- Low sidelobes meeting ITU Rec

- Low profile and streamline design

- Small size and weight

- Low power consumption

- High reliability

In order to satisfy all of these features, three classes of SOTM antennas can be specified: antennas with two-dimensional mechanical scanning; antennas with two-dimensional electrical scanning and systems with combined scanning, where the scanning is electrical in the elevations plane and it is mechanical in the azimuth plane. The solution currently available is the fully mechanical one, even if there are examples of the other kind of antennas reported in literature. The direct line-of-sight between the earth terminal and the satellite requires the

terminal antenna to see from horizon to overhead in elevation and 360° in azimuth angle, with total hemispherical coverage. This is realized by mounting the antenna on a moveable platform. The pointing mechanism has also stringent requirements as well because, in spite of constant vibrating, pitching, rolling and yawing the Mobile SatCom antenna's narrow radiation beam must be pointed accurately to satellite. Furthermore, mobile antenna have to satisfy the requirements of robustness, easy installation and reasonable cost. While antennas installed on ships or large vessels do not need too much space, terminal mounted on terrestrial vehicles and aircraft need smaller and aerodynamic antenna.

Other than the challenges posed by mechanical steering which requires radiator as small and light as possible, the electrical design is cumbersome by itself. In fact, to reduce its size, the antenna has to support TX and RX operations on a single radiating surface, to provide polarization switching and have good efficiency.

In the following is presented the design of a printed antenna array which operates on the frequency bands allocated to K/Ka band satellite communications (RX:19.1GHz-20.1GHz-TX:29GHz-31GHz) able to support polarization switching. The main challenges are to design a self diplexing radiating elements, able to cover both TX and RX bands, and to identify a lattice which can accommodate the dual band elements while avoiding the onset of grating lobes

2.2.   Dual-Bands, Dual-Polarized array antenna

The design of an array able to integrate both Tx and Rx operation in a single aperture is difficult to realize but it is essential. Two solutions may be take into account: array of elements with a bandwidth large enough to cover both Tx and Rx or a arrays od dual-band elements. The first solution has been largely explored [4]. For example, arrays of tightly coupled dipoles with ultra wideband performance have been recently studied [5] for Ku-band SOTM showing excellent scanning behaviour in a wide angular range. However, this approach has two main problems which surfaces even in the case of fixed beam antennas which are not designed for electronic beam steering. The reduced cell size results in an increased number of elements and, consequently, in a excessively complex Beam Forming Network. Secondly, an element covering bot TX and RX bands would need some mechanism to isolate the two bands which would make more complex the design. To avoid these problems, a configuration of radiating element based on coaxial printed rings was chosen [6]. This kind of element is preferred because it is naturally self diplexing, i.e. it provides a good TX/RX isolation while showing enough bandwidth and good efficiency. Also it permits the design of independent TX and RX BFN which can be realized at different levels of the stack up so ensuring good isolation.

2.2.1. Radiating element

The radiating element is designed to have dual-band operations, 19-21GHz (Rx band) and 29-31GHz (Tx band) and it is shown in Fig. 2.1 and in Fig. 2.2. It is composed of two nested radiators and it is based on the design presented in [6]. The outer radiator is a coaxial structure formed by a cage of metalized via holes

and it operates on the Rx band. The inner radiator is actually a circular waveguide operating in Tx band. The ring of via-holes forms a conducting wall that helps to minimize the impact of mutual coupling effects. The two radiators are fed with different techniques. In the Rx band a stripline feed is used, where strips enter into the radiator between adjacent via-holes. Dual polarization is obtained placing the feeding network at different levels to obtain a good isolation between the two polarizations. As it can be seen, two feed are used for each line to enforce linear polarization and to improve isolation. The inner radiator is fed with two microstrip on the lower ground plane coupled to two orthogonal slots placed in T configuration. Notice that the Rx feeding lines for the two polarizations are physically isolated between them and from the Tx feeding lines. The overall thickness of the antenna is about 2.5mm.
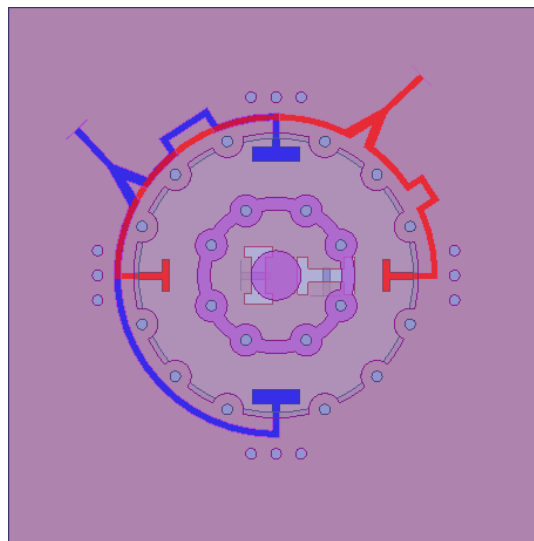
Fig. 2.1 - Dual-Bands, Dual-polarized radiating element

20GHz radiating element

30GHz radiating element

Shorting pins

Ground with coupled slot
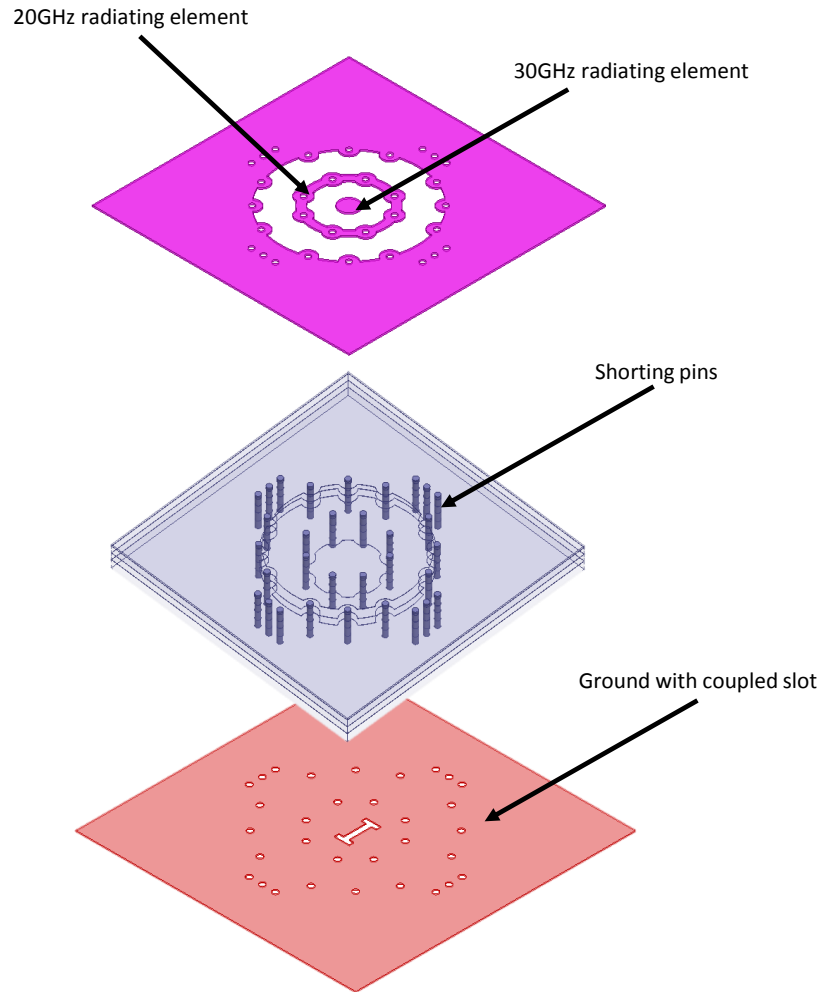
Fig. 2.2 - Dual band single element geometry

	Outer ring	**Inner Ring**	**Thickness**
Dual Band Dual Polarized antenna	8mm	3.5mm	2.56mm

Tab 2.1 – Characteristics of the antenna

The Rx radiator has a gain of approximately 7dBi and a flat behaviour on the overall band of interest, while the gain of the Tx radiator is 6dBi. This higher value of the gain in Rx band is related to the shorted pin near feeding line that both increase the isolation and gain level. In the figure listed below (Fig. 2.3 and Fig. 2.4) are reported the reflection coefficient and the coupling between Tx and Rx

elements. The geometry of both antennas was optimized to obtain a good impedance match to 50Ω in the whole bands without requiring additional matching networks. As it is shown, the two antenna are highly isolated especially in the lower band because at this frequency the inner radiator is in cut-off.
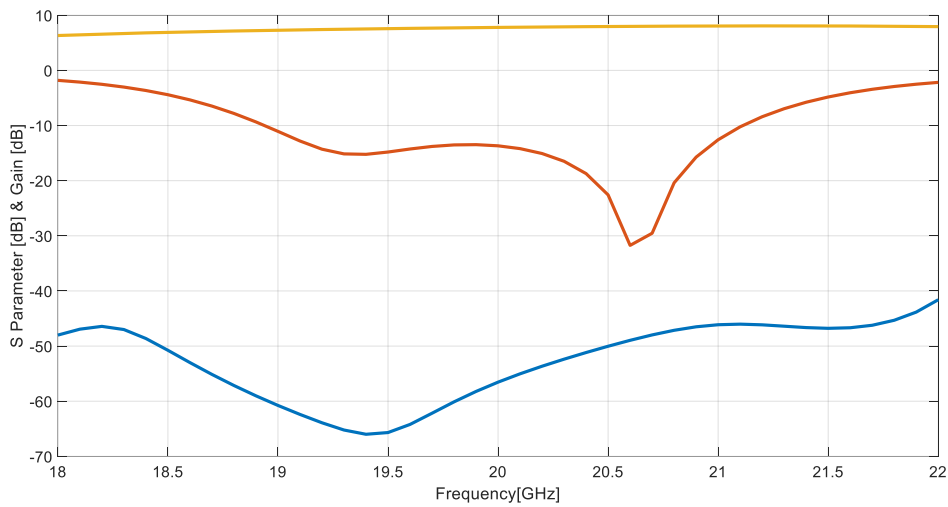
Fig. 2.3 - Simulated S parameters and Gain of the Rx radiator
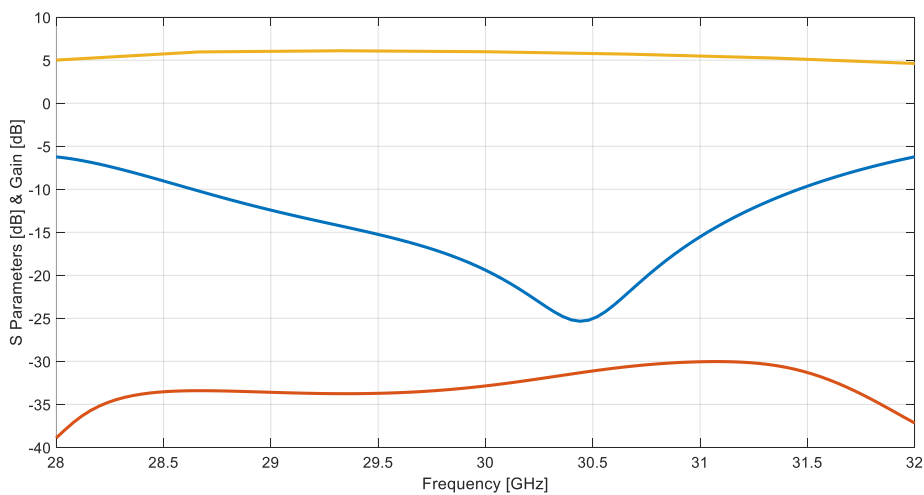
Fig. 2.4 - Simulated S parameters and Gain of the Tx radiator

2.2.2. Antenna array

If the distance of the elements is too large, grating lobes may appear on the radiation pattern of the antenna. As it is known, grating lobes are unwanted radiation peaks pointing at directions not collinear to the main beam, and are related to the element spacing. The well known formula

$$d < \lambda(1 + \sin\theta)$$

gives an upper bound to the inter-element distance before grating lobes appear. At θ=0°, the separation d can be large as λ before the onset of the first grating. However, this constraint related to the inter element spacing is theoretical, in fact during the design procedure d<0.9 λ is normally considered as the maximum value that inter element spacing could assume. Considering the present work, the diameter of the outer radiator is 8mm, as reported in Tab. 2.1. This mean that it is not possible to utilize a rectangular lattice array, otherwise grating lobes will appear in the radiation pattern. According to this restriction, a triangle lattice configuration was adopted. Using this configuration, the grating lobes occur when:

$$d < 1.15\lambda/(1 + sin\theta)$$

allowing more space to accommodate the radiating elements. In Fig. 2.5 it is shown the array of elements placed in the triangular lattice. Also visible are the BFN which feed independently the dual polarized TX and RX elements
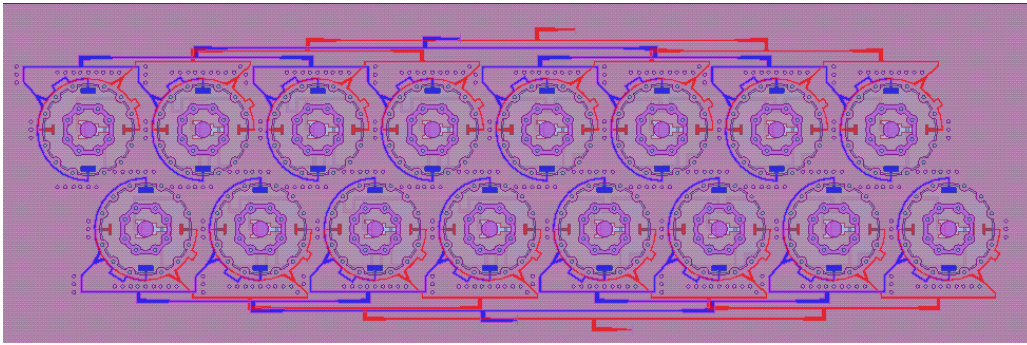
Fig. 2.5 - Dual bands, Dual-polarized array antenna

The radiating element were designed in view of their integration in a dual-band dual-polarization array antenna. In Fig. 2.6 a cross sectional view of the array is reported. The array antenna has been designed in order to obtain a good isolation between both different polarizations and different bands. For this reason, during the design of the array structure, it was adopted a different solution for the feeding network of the Tx elements. In particular, one polarization was fed by a microstrip-feeding network on the lower ground plane coupled with the antenna through a slot while the other polarization was fed through a stripline feeding network such as the feeding network of the Rx element. Thanks to this solution, it was possible to isolate all the different source and to realize a 8x2 array antenna (Fig. 2.7). To obtain an easier integration with electronic components in the future, vertical transition were used. In this way all the input were placed on the same layer of the microstrip line (Fig. 2.7).

Vertical polarization Rx band

Horizontal polarization Rx band

Vertical polarization Rx band

Horizontal polarization Rx band
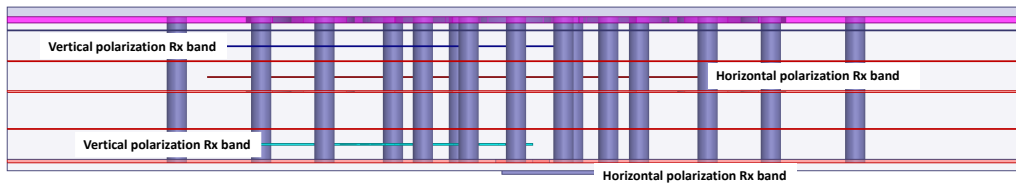
Fig. 2.6 - Stack-Up of the array antenna

Vertical transition Rx band

Vertical transition Tx band
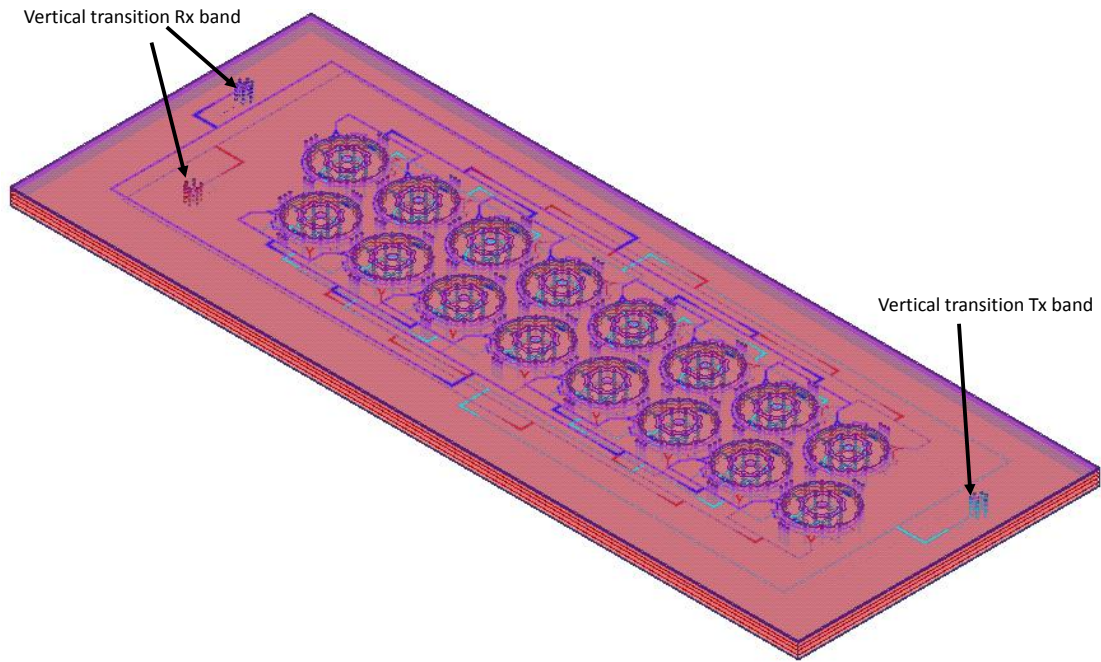
Fig. 2.7 - Section view of the Dual Band, Dual polarized array antenna

Simulation results of the array are shown in Fig. 2.8 and Fig. 2.9. As it can be observed, for the Tx and Rx configurations of the array antenna results present a good matching both E and H plane. It is also possible to notice good isolation between both different polarizations and different bands, as it was requested.
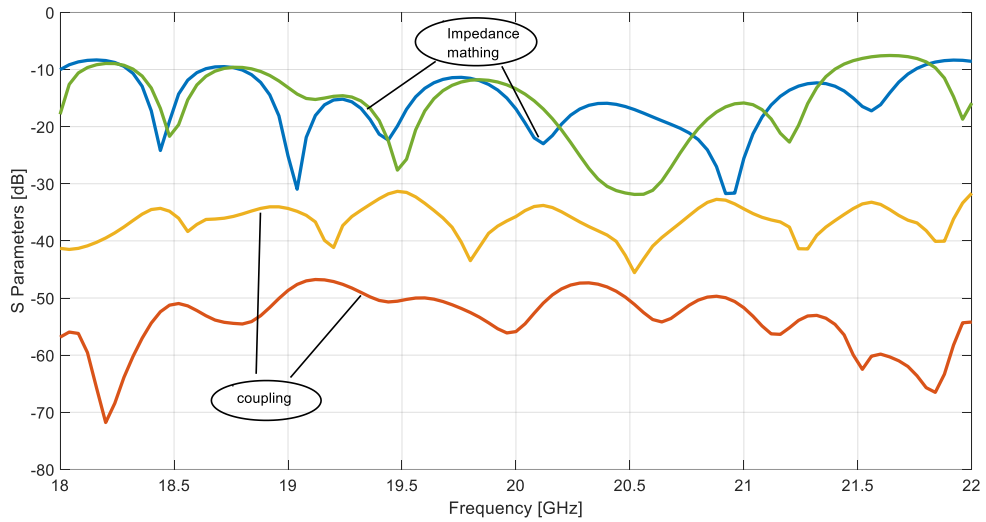
Fig. 2.8 - Simulated S-parameters in Rx band of the array configuration
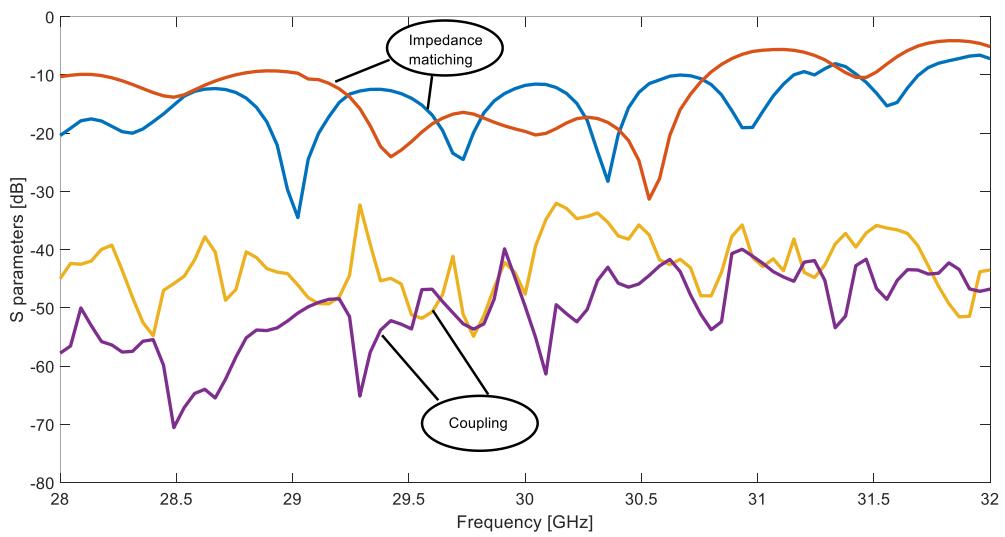
Fig. 2.9 - Simulated S-parameters in Tx band of the array configuration

The co-polar and cross-polar radiation pattern along E-plane and H-plane were simulated both for Rx and Tx elements as shown in Fig. 2.10 and Fig. 2.11, respectively. In both case, co-polar radiation patterns present a good behaviour with a broad beam well defined and without the presence of grating lobes as we

expected. A gain of 17dBi for Rx configuration and 18dBi was obtained for Tx configuration, respectively. In both operational bands the cross polarization level are well below 30dBi.
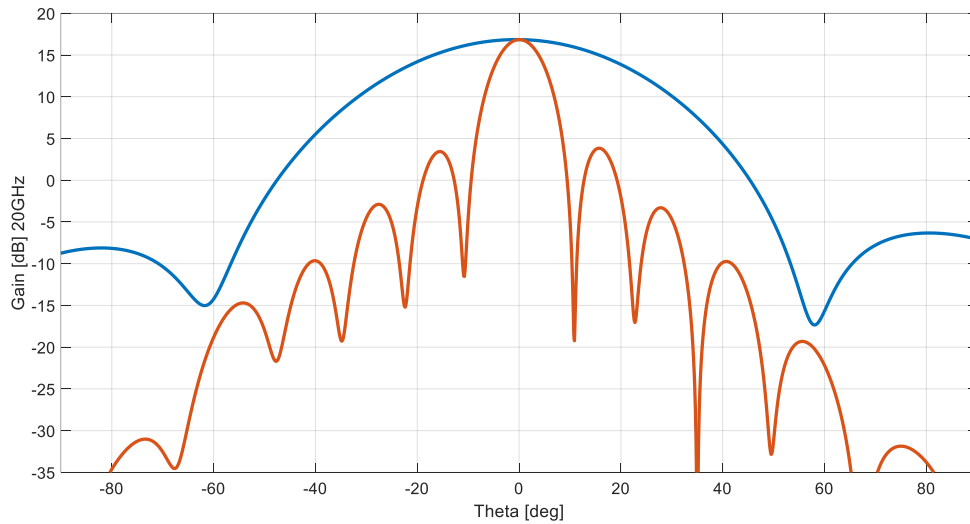
Fig. 2.10 - Radiation pattern at 20GHz
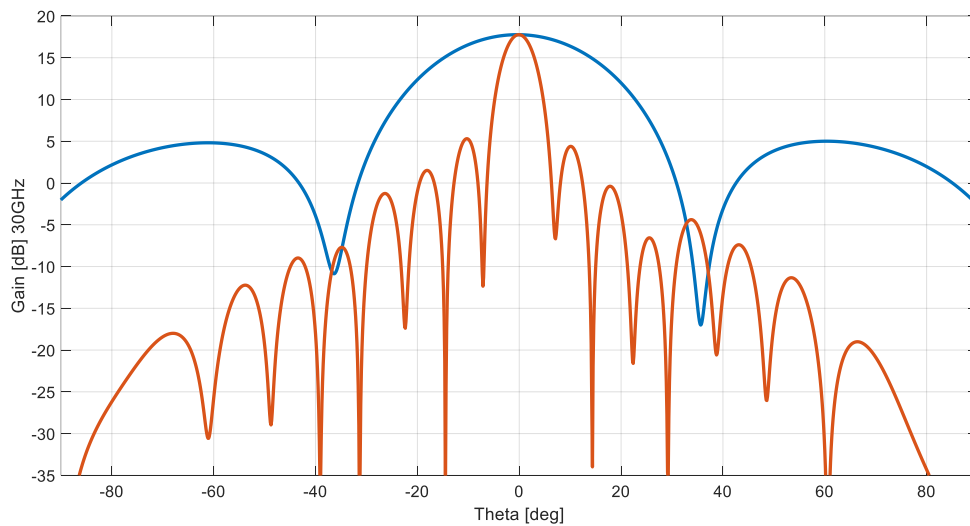
Fig. 2.11 - Radiation pattern at 30GHz

The good polarization purity of the radiating elements at both bands and the good isolation between different polarizations, make this antenna suitable also to

radiate or receive circularly polarized signals. In Fig. 2.12 and Fig. 2.13 are reported the radiation diagram of the RHCP and LHCP polarization.
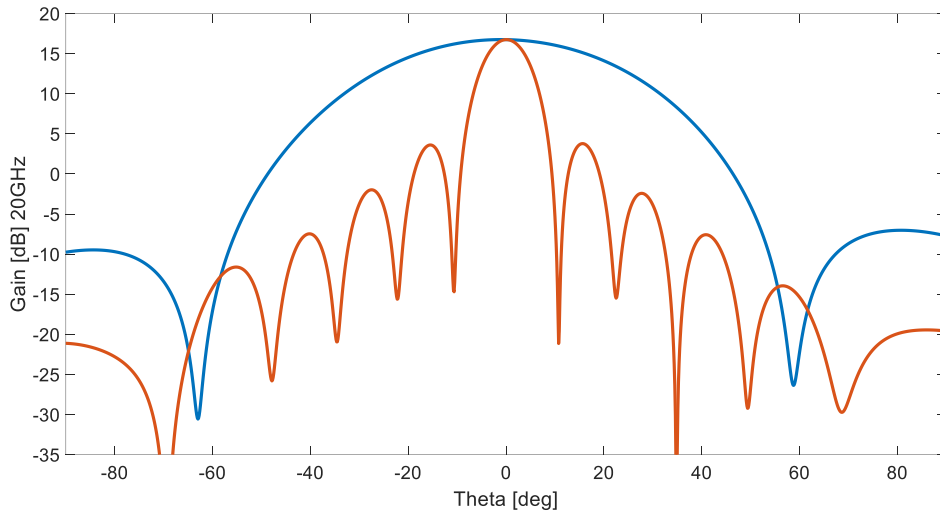
Fig. 2.12 - RHCP radiation pattern at frequency of 20GHz
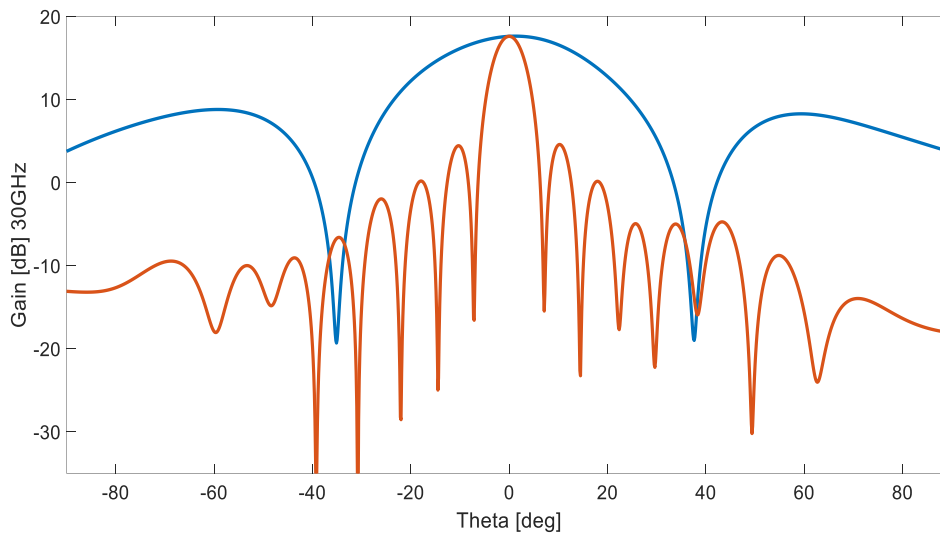
Fig. 2.13 - RHCP radiation pattern at frequency of 30GHz

2.2.3. Measurements

At this stage only a prototype of the single radiating element has been realized. The antenna has been fed with Huber-Suhner MMX connectors which is soldered at lowest layer of the stack up. A MMPX connector – K connector transition was

used to connect the antenna to the Network Analyzer. The antenna is shown in Fig. 2.14, Fig. 2.15 and Fig. 2.16.
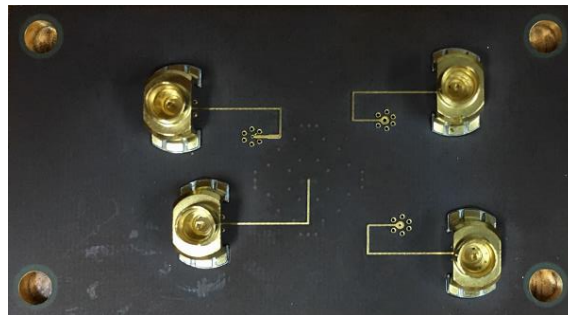
Fig. 2.14 - Bottom view of the antenna
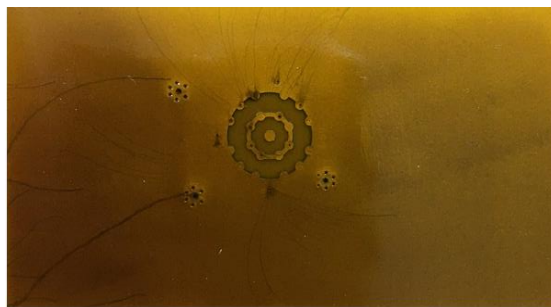
Fig. 2.15 - Top view of the antenna
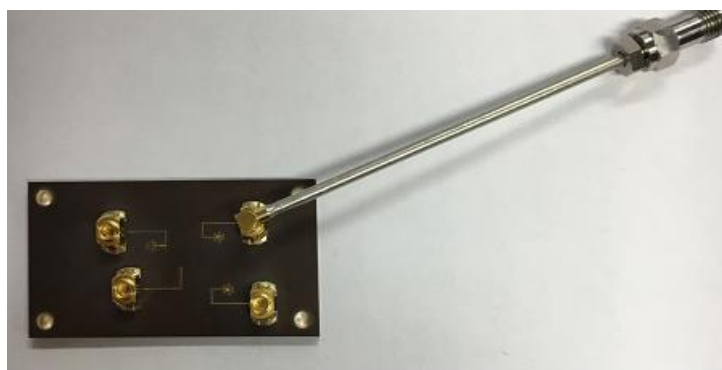
Fig. 2.16 - Antenna with MMPX to K transition

Only the performance of S-parameters and gain of the single radiator have been measured.

The antenna was not measured in an anechoic chamber but it was realized a measurement setup on a bench. The antenna and a wideband horn were

positioned one in front of the other at a distance of 64cm which, considering that the longest side of the horn is 8cm, is in the horn far field The characteristics of the wide band horn are reported in the Tab. 2.2 .

Frequency [GHz]	Gain [dBi]	Frequency [GHz]	Gain [dBi]
15	15.3	28	19.5
17	16.8	30	19.7
18	17.5	32	19.1
19	17.8	34	19.3
20	18.2	35	19.2
21	18.8	36	19.1
22	18.9	38	18

Tab. 2.2 - Gain of the wide band horn

The overall system was shielded with absorbers. In Fig. 2.17 and Fig. 2.18 are shown the gain of the two polarizations of radiator. As it can be seen, measured gain present a frequency shift with respect to the simulated results. This behaviour is also clear in the trend of the S-parameters showed in Fig. 2.19 and Fig. 2.20. The values of the gain reported in Fig. 2.17 and Fig. 2.18 do not take into account the losses due to the connectors (0.35db) and transition (0.4dB) necessary to connect the antenna to the network analyser.
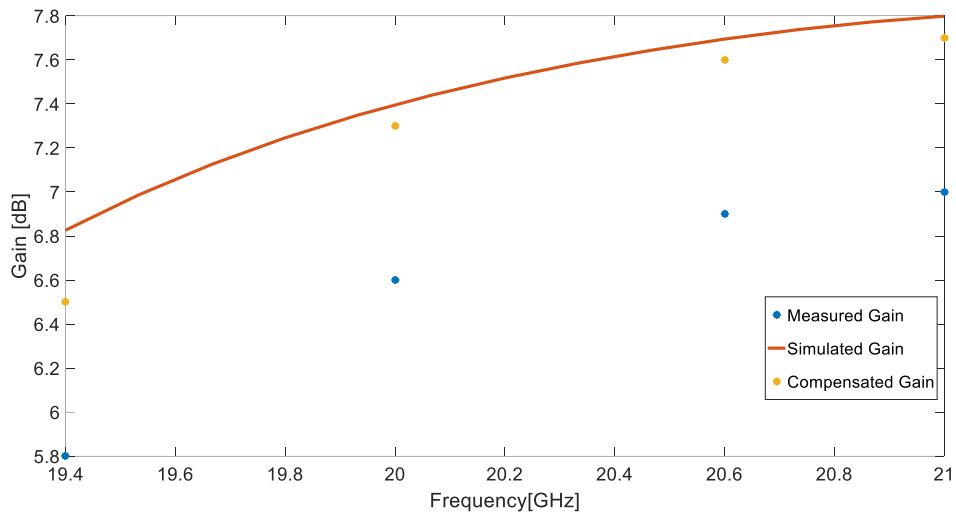
Fig. 2.17 - Gain of the horizontal polarization in Rx band
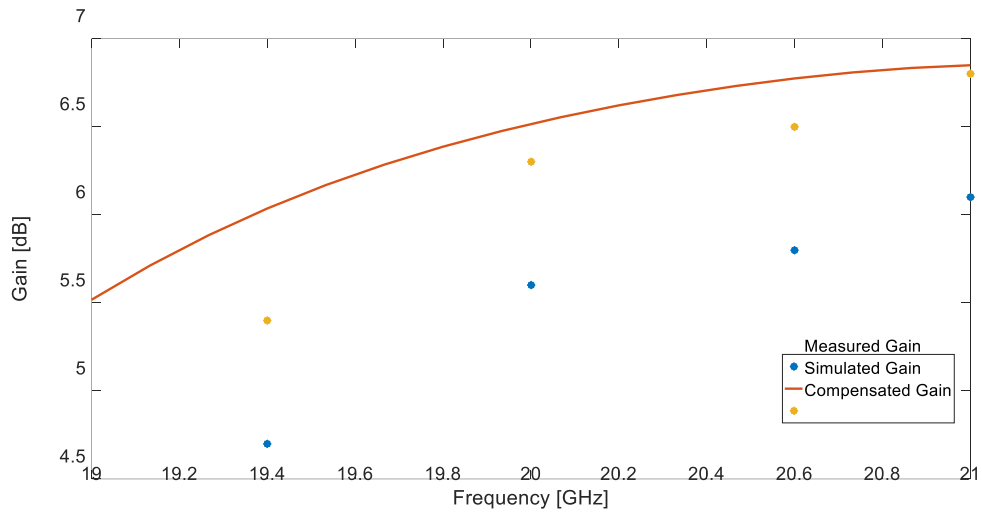
Fig. 2.18 - Gain of the vertical polarization in Rx band
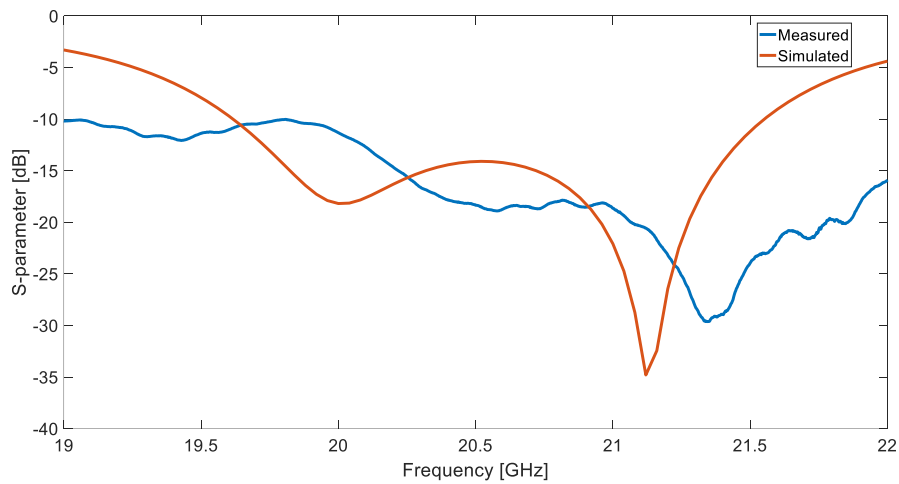
Fig. 2.19 - Vertical polarization in Rx band
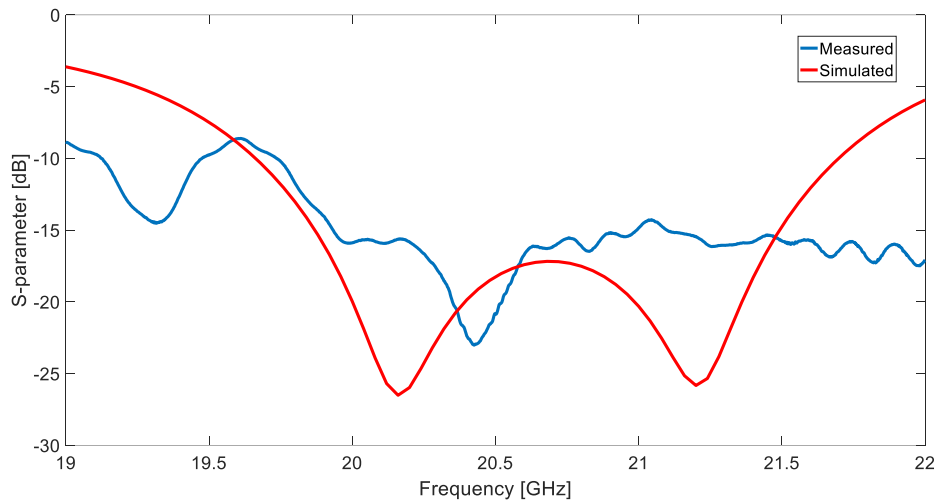
Fig. 2.20 - Horizontal polarization in Rx band

In Fig. 2.21 and Fig. 2.22 are shown the measured parameters in the Tx band. Even in this case, it is possible to observe a frequency shift.
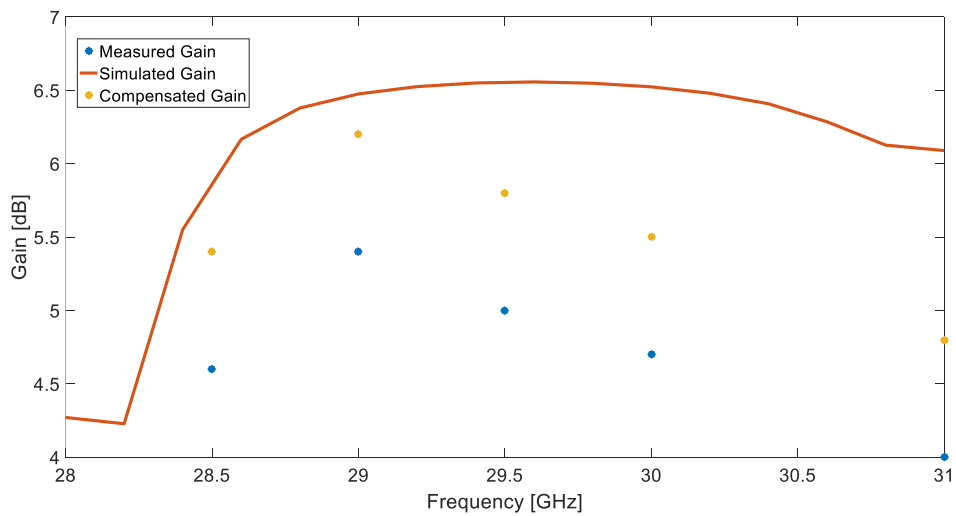
Fig. 2.21 - Gain of the horizontal polarization in Tx band
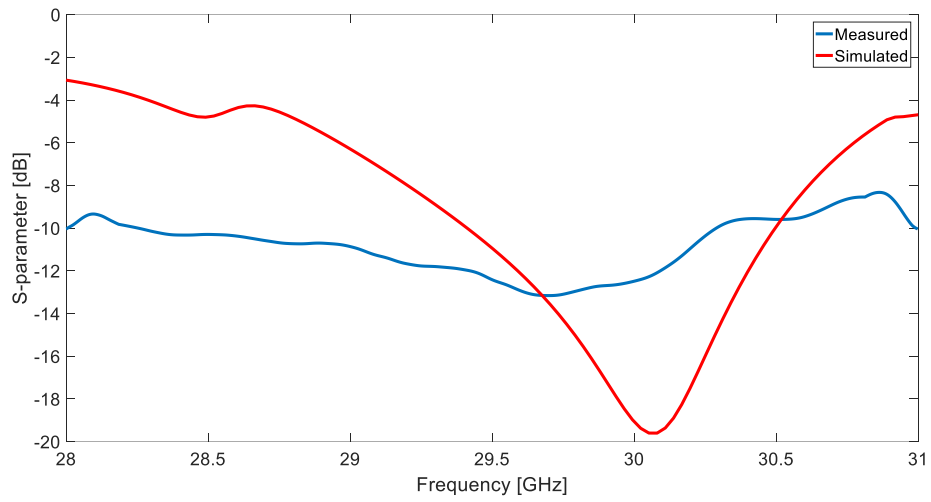
Fig. 2.22 - S parameters of the horizontal polarization in Tx band

The frequency shift observed both in the measurements in Rx band and in Tx band are related to the manufacturing process. For the same reasons the vertical polarization TX resulted compromised and results are not shown here.

3. Cylindrical Reflector Antenna for wireless communication systems

3.1.   State of the Art

During the last years, the need of new mobile services and communication systems led to an overcrowded frequency spectrum. The allocation of the mm-Wave frequency is seen as a solution to this problem in both satellite and terrestrial communications. As far as satellite communications are concerned, the shift towards higher frequencies is shown by the number of high power Ka band satellites that has spawn the development of high performance user terminals with typology and size that change considerably according to the applications. As an example, a new breed of Satcom-On-The-Move (SOTM) terminals have been presented by several companies to offer internet services on vehicles, ships and airplanes. These terminals have to use high efficiency antennas of reduced size and weight to be mounted on mechanical pointing systems, as it was already discussed in the previous chapter. Earth fixed terminals do not pose the same constraints in weight and size as SOTM antennas. However, there are applications, like defence and security, where reduced size, light weight, man transportable terminals, quick to be deploys are needed. These antennas are usually very cumbersome to design as they have to provide good efficiency and compliance with challenging EIRP density masks on the satellite Geostationary

Orbit (GSO) plane, while maintaining a radiating surface as small as possible. For this reason arrays of waveguide radiators or reflector antennas are used.

Similar challenges are faced when designing antennas for point to point (fixed beam) mm-Wave wireless links to be used in backhaul system for the current or the next generation of mobile communications (5G). As an example, the architecture of 5G will be composed by heterogeneous wireless network macro-cells overlaid by mmW small-cells deployed in dense user areas (Fig. 3.1). In this scheme, mmW small-cell Access-Point (APs) will support massive data exchanges for mobile users with very high data rates, low latency, low interferences and low power consumption per bit. These AP will be connected between themselves and to the cellular network through high-capacity backhaul/fronthaul links which may be implemented over optical fibre or mmW poit-to-point wireless links.
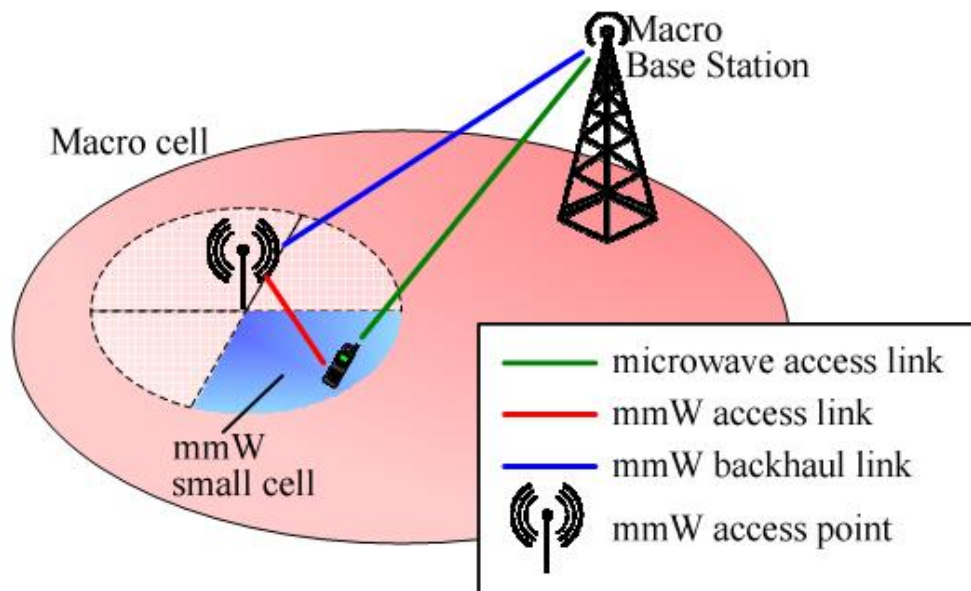
Fig. 3.1 - 5G hybrid radio access architecture with a macro-cell providing microwaves access, mmW small cells and mmW backhaul.

The utilization of mmW terminals in backhaul links give the possibility to obtain high data rates without extreme increase in spectral efficiency in contrast to

centimetre wave cellular systems with highly complex techniques aimed at predominately achieving a higher spectral efficiency due to much smaller available bandwidths. These wireless links are capable of replacing fiber optics, because they are less costly and easier to deploy [7]. As in the case of satellite communications, they are required to be mechanically small, of high gain and suitable for integration with the radio. Microstrip circuits are appropriate for integration with active MMIC components, but they suffer from higher losses with increasing frequency as well as from the presence of cavity resonances when packaged. For these reasons, similarly to satellite communications, arrays of waveguides and reflector are the most common solutions.

Arrays and reflectors are both good solutions but none of them can be considered as optimal. Gain and overall efficiency of an array antenna depends mainly on the losses of the feed network. An array of metallic waveguide radiators may reach an aperture efficiency up to 80% when using a parallel fully branched (i.e. corporate) feed network. However, arrays of waveguides requires the design of complex feeding network which may become very challenging if multiband operation and beam tapering are required.

The efficiency of reflector antennas may be high due to their low losses, but reflectors suffer of spill over loss and non-uniform illumination, and they are not low profile. However, reflectors are simpler than array to build and they may be made lighter when carbon fiber or resins are used to build the reflecting surface. One well known issue of both structures is the fulfilment of regulations on radiated power density masks. To make radiation patterns complaining with regulations is not an easy task and usually the solution adopted is to use larger aperture to have narrower beams. Array with highly tapering BFN may be designed with a loss of efficiency and considerably increased complexity. However, arrays allows

for a simpler and effective solution exploiting the natural tapering observed considering the radiation pattern along the diagonal of a rectangular aperture.

The reflector antennas are normally easier and cheaper to build and limit the complexity to the design of the feed. The most commonly used reflectors are axially-symmetric dual reflector antennas, typically Cassegrian and Gregorian systems [8], or their "displaced axis" or "ring focus" variants [9], [10], [11]. In these cases, a low profile may be obtained considering "deep dish" with reduced f/D ratio (<0.3). These antennas normally adopt self supported re-irradiating feed, like hat feed and splash plate feed, which do not use supports to improve blockage loss. However, the design of a feed able to ensure a good efficiency and fulfilling mask requirements at the same time is cumbersome, in particular when dual band operation have to be obtained.

In this chapter, a novel antenna which reduce the complexity and the cost related to the manufacture of an array is proposed. The terminal is based on a cylindrical reflector antenna .This solution retain the simplicity of the reflectors and alleviates the design of the feed. In fact, as it is in the case of arrays, the rectangular aperture of the cylindrical reflector can be used to exploit the radiation tapering on the diagonal plane. As an example, in the case of the satellite communications, power density masks are fulfilled by simply orienting the diagonal of the antenna on the satellite, without lengthy feed optimisation.

3.2. Cylindrical Reflector antenna

A picture of the cylindrical reflector is shown in Fig. 3.2. The reflector is fed with a parallel plate in which a TEM mode is excited. The parallel plate radiate toward a corrugated hat feed which direct the field on the cylindrical reflector.
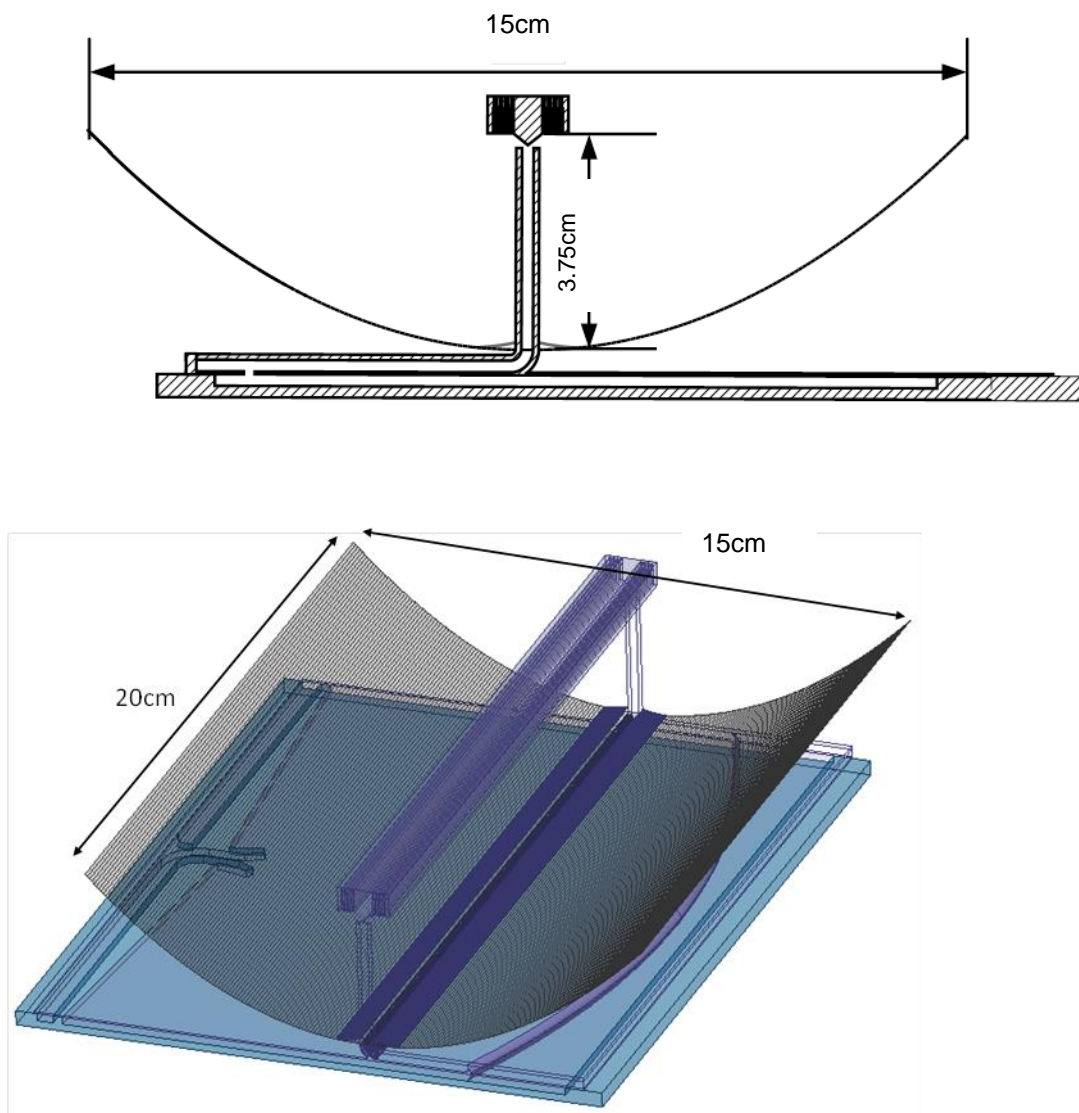
Fig. 3.2 Structure of Cylidrical Reflector

The antenna is linearly polarized, circular polarization may be achieved with the help of a printed polarizer placed on top of the reflector. The structure is

essentially composed by three parts: the parallel plate, the hat feed and the reflector. In the following the design of the three blocks will be described.

3.2.1. Parallel Plate

The hat feed is illuminated by a parallel plate waveguide fed with a rectangular horn. Due to the strong linear polarization of the feed, the radiation pattern on the antenna can be considered and optimized independently on the two principal planes. To obtain a flat field distribution to illuminate the hat feed, a parallel plate waveguide structure is used to feed the antenna.
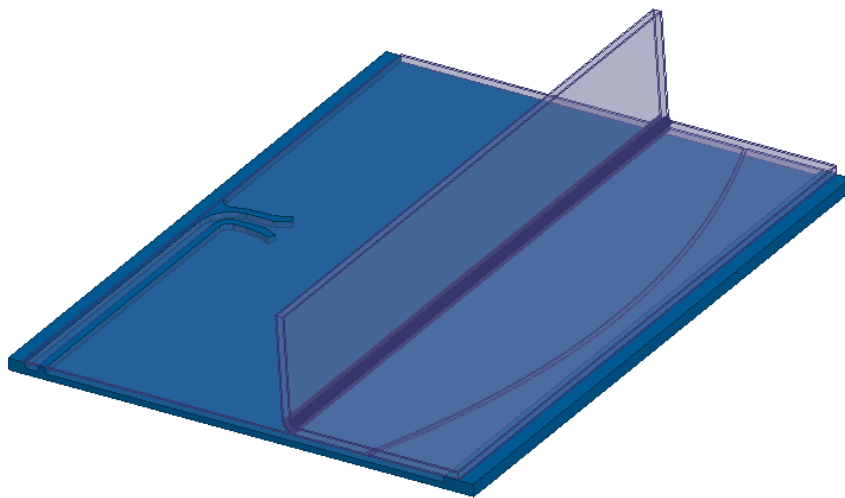
Fig. 3.3 - Parallel plate structure

As shown in Fig.3.3, the parallel plate waveguide is composed by two different levels. In the first one, a horn antenna illuminates the parabolic reflector place in the ppw. The wave reflected by the parabolic reflector propagates to the second level through a coupling slot located between the two layers. In this way, it is possible to have a distribution field without the blockage effect. The PPW and the feeding horn have been optimized to have a flat field distribution and good taper

to reduce side lobes. In Fig.3.4, it is shown the field pattern inside the parallel plate top layer at the frequencies of 40GHz and 60GHz. As it is possible to see, the field distribution is quite flat along the aperture.
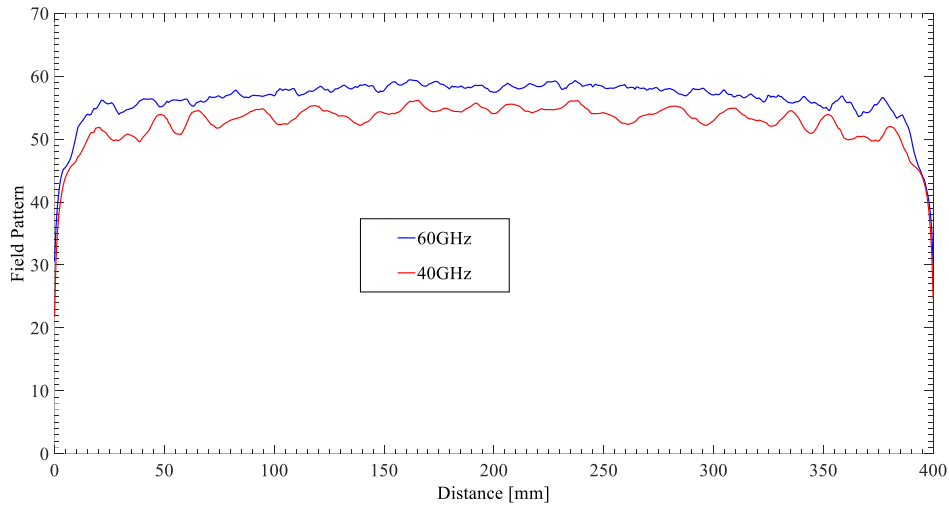
Fig. 3.4 Field distribution inside the PPW

In Fig. 3.5 is shown the radiated field corresponding to the field distribution reported in Fig. 3.4.
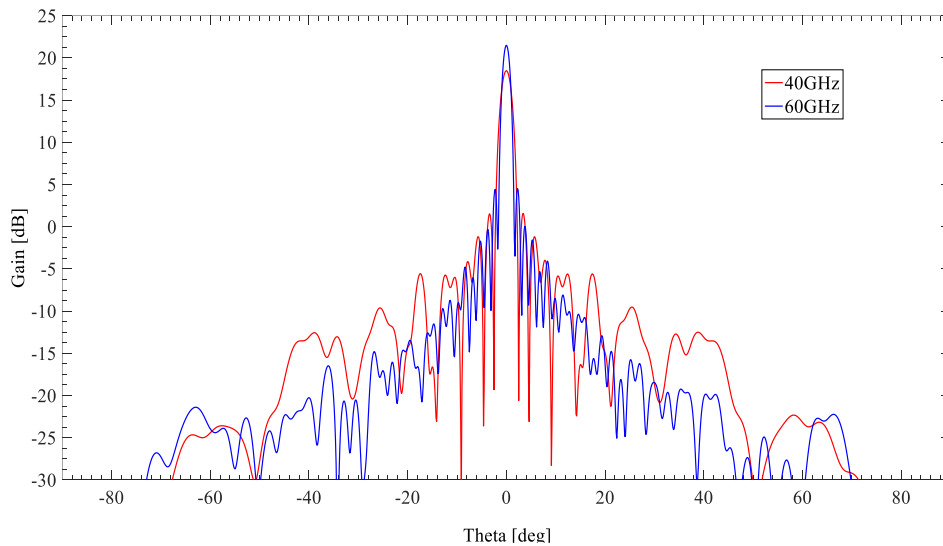
Fig. 3.5 - Radiation Pattern of the PPW

3.2.2. Hat Feed

3.2.2.1.   General considerations

Hat feeds (Fig. 3.6) are self-supported, rear irradiating feed that have many advantages such as low side lobes level, low spillover losses and no blockage or scattering from support struts. A classic version of the hat feed is composed by a waveguide (the neck), a dielectric spacing (the head) and a corrugated structure (the hat). The corrugation of the hat brim is traditionally λ/4 deep causing the normal component of the E-field to be zero along the brim. To understand the behaviour of the Hat feed, let consider the definition of electromagnetic soft and hard surface.
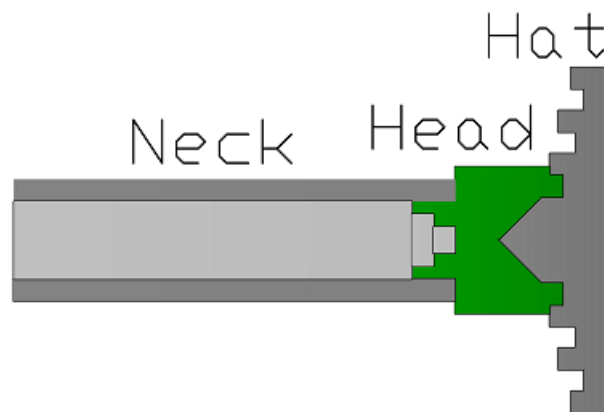
Fig. 3.6 - Profile of the Hat Feed with its three main parts

Considering the boundary conditions of the E-field it is possible to define soft and hard surface for electromagnetic propagation. The electromagnetic soft and hard surfaces have polarizations independent boundary conditions (at the centre frequency) in contrast to a metallic conductor that has different boundary conditions for the tangential and normal components of the E-field. The soft and hard surfaces are realised by providing a metal conductor by an anisotropic surface impedance. This can be obtained by providing it with corrugations, or with

a strip-loaded dielectric layer. Generally, the hard surface will support waves with a maximum value of the E-field at the surface for any polarization, whereas the soft surface makes the amplitude of the E-field zero at the surface (Fig. 3.7).

Soft STOP surface (left)   **Hard GO surface (right)**

**Transverse
air-filled corrugations**   **Longitudinal
dielectric-filled corrugations**
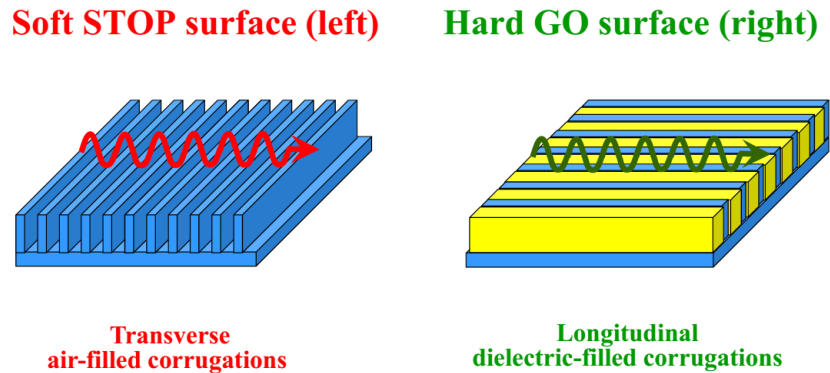
Fig. 3.7 - Hard and soft surface structure

To understand how a soft surface works, let us now consider electromagnetic waves, and write the E-field as

$$\vec{E} = E_t\hat{t} + E_l\hat{l} + E_n\hat{n}$$

Where $\hat{n}$ is the unit normal to the surface, and $\hat{t}$ and $\hat{l}$ are unit vectors tangential to it with $\hat{t}$ normal to the direction of propagation of the wave and $\hat{l}$ normal to $\hat{t}$ and directed along the projection of the direction of propagation along surface. Thereby $\hat{t}$ and $\hat{n}$ specify transverse directions, and $\hat{l}$ specifies the longitudinal direction (Fig. 3.8).
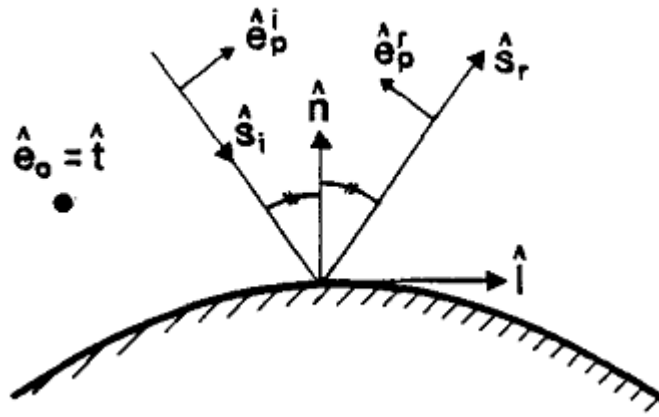
Fig. 3.8 - Ray-fixed coordinate system

We let $\hat{l}$, $\hat{t}$ and $\hat{n}$ form a righthand orthogonal coordinate system. The boundary condition of a perfect conductor is the tangential components of the total E-field at any regular point of the scattering surface be zero:

$$E_t = E_l = 0$$

If the conductor is located in a homogeneous dielectric (i.e. with constant permittivity) it is possible to use the previous conditions and Maxwell's equations $\vec{V} \cdot \vec{E} = 0$ to show that $\partial E_n / \partial \text{n} = 0$, or generally

$$\frac{\partial E_n}{\partial \text{n}} + \frac{(r_1 + r_2)}{r_1 r_2} E_n = 0$$

If the surface is curved with r1 and r2 the two principal radii of curvature. Therefore, if we consider each of the three field components separately, we may state that a perfect conductor corresponds to a soft boundary for the tangential field components $E_t \ and \ E_l$, and to a nearly hard boundary for the normal field component E_n. To realize a soft surface, let consider a surface with transverse corrugations as shown in Fig. 3.9, where

$$v \ll w + v \ll \lambda/2$$
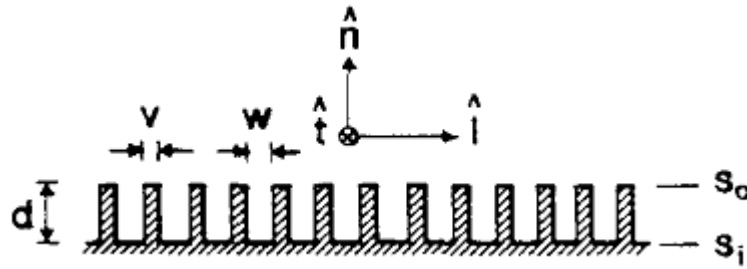
Fig. 3.9 - Transverse corrugations

Where w is the width of the corrugations, v is the width of the edges between them and λ is the wavelength. The corrugations are narrow, so that a number of discrete modes can describe the field solution within them. When the condition $v \ll w + v \ll \lambda/2$ is satisfied there will be only one nonevanescent mode present within the corrugations. This is a TEₙ Mode with an E_l component only, and this component will have no longitudinal variation within each corrugation. Notice that a TEM mode could be present in the grooves but the TEM mode is a degeneration of a TM mode rather than a TE one. The E_l-field inside the corrugations is generally accompanied by H_t and H_n fields, but we can choose the corrugation depth d that transform H_t to

$$H_t = 0 \; or \; equivalently \; |Z_l| = \infty$$

At the outer surface S_0. At the edges between the corrugations $H_t = 0$ as well because there can be no longitudinal currents when v→ 0. The E_t and H_l components at S_0 are determined by the edges between the corrugations. They short circuit E_t very efficiently with strong transverse currents, so that

$$E_t = 0 \ or \ equivalently \ Z_t = 0$$

Therefore from these two condition related to E_t and H_t the transversely corrugated surface is a soft surface, if d is chosen so that $H_t = 0$ is satisfied ad S_0. The value of d is related to the choice of the surface and corrugations. The simplest case is a plane surface with a plane wave incident on it. We let the corrugations be straight and transverse to the direction of incidence of the wave. Then, the E_l field of the TE_n mode within them is given by

$$E_l = \sin(kn + kd)$$

Where k=2π/λ is the wavenumber and n is the dimension variable along $\hat{n}$, with n=-d at the inner surface S_i and n=0 at S_0. E_l satisfies the boundary condition $E_l = 0$ at n=-d. The condition $H_t = 0$ applied to the TE_n mode is by using Maxwell's equation $\vec{V} \cdot \vec{E} = -j\mu\omega\vec{H}$ equivalent to

$$\frac{\partial E_l}{\partial n} = 0 \ at \ S_0$$

That is satisfied and thus the surface is soft when

$$d = \lambda/4$$

3.2.2.2. The hat feed for a cylindrical reflector – Theory

The hat feed used in the antenna shown in Fig. 3.2 is illuminated by a PPW which mainly radiates a TEM mode. In this condition, the hat feed behaves like a soft surface and its working principle relies on its capability to sustain and to guide

surface waves along corrugations and to direct them towards the reflectors, rather than to simply reflect them as it is done in the case of splash plate feed. In fact, in the hat feed waves radiated by the PPW guide are reflected by the cuspid towards the corrugated surface, on which TM surface waves are excited. To better define guidelines to the design of the hat feed, it is useful to ascertain the characteristics of the TM surface waves propagation on a corrugated plane. The analysis presented in the following, it is not rigorous, however numerical software currently available allows the access to meaningful numerical data in short time. What it is presented here will prove useful to have a broader comprehension of the phenomena and to define starting points for the optimization process. In Fig. 3.10 is shown an infinite corrugated conducting plane. The structure extends to infinity in both z and y direction.
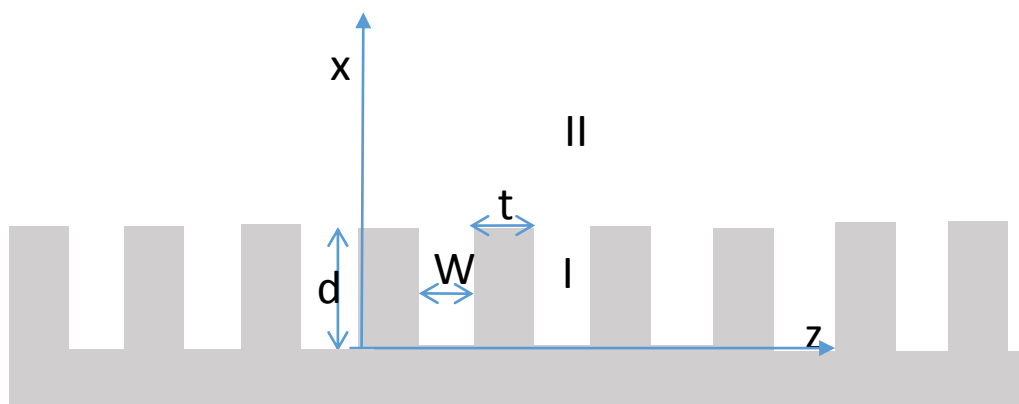
Fig. 3.10 - Infinite corrugated ground plane

As it can be seen, the structure is periodic, with period $L = W + t$ and it extends infinitely along the z axis. Also, it is of an infinite extent along the y axis as well, so we will assume that the fields do not depend on the y coordinate. As the structure is periodic a Floquet expansion of the fields is considered in the region external to the grooves (region II in Fig.3.10). A TEM solution is investigated

within the grooves (region I) and a TM surface waves is considered in region II.

Under these positions the Helmholtz equation for the H_y field is considered

$$\nabla^2 H_y(x,z) + k_0^2 H_y(x,z) = 0 \tag{1}$$

Separation of variables leads to the following two equations for $H_y(x,z) = g(x)f(z)$

$$\frac{\partial^2 g(x)}{\partial x^2} + k_x^2 g(x) = 0$$

$$\frac{\partial^2 f(z)}{\partial z^2} + k_z^2 f(z) = 0 \tag{2}$$

with $k_0^2 = k_x^2 + k_z^2$.

The periodicity of the structure along z induces a degree of periodicity on the solutions as well both region (I) and (II). In region (II) one can pose that $f(z)$ is almost periodic with period L but a phase shift accumulated at each cell:

$$f(z+L) = f(z)e^{-j\psi} \tag{3}$$

$f(z)$ it would be conveniently expressed as a Fourier series. To do this one first consider the function

$$F(z) = f(z)e^{j\left(\frac{\psi}{L}\right)z} \tag{4}$$

$F(z)$ is a periodic function as:

$$F(z+L) = f(z+L)e^{j\left(\frac{\psi}{L}\right)(z+L)} = f(z+L)e^{\frac{j\psi}{L}z}\,e^{j\psi} = f(z)e^{-j\psi}e^{j\frac{\psi}{L}z}e^{j\psi} \tag{5}$$

$$=$$

$$= f(z)e^{j\left(\frac{\psi}{L}\right)x} = F(z)$$

So $F(z)$ is now expressed as Fourier series

$$F(z) = \sum_{n=-\infty}^{n=+\infty} A_n e^{j\frac{2n\pi}{L}z} \tag{6}$$

Substituting expression (3) one has

$$f(z) = \sum_{n=-\infty}^{n=+\infty} A_n e^{j\left(\frac{2n\pi}{L}z - \frac{\psi}{L}z\right)} \tag{7}$$

Expression (7) is the Floquet expansion of $f(z)$. In the following we will make use of the more meaningful notation

$$f(z) = \sum_{n=-\infty}^{n=+\infty} A_n e^{-j\left(\frac{2n\pi}{L}+\beta\right)z} \tag{8}$$

Going back to equations (1), under the assumption that the width of the grooves $W \ll \lambda$ to allow the propagation of TEM mode only, one can write the following solutions

Region (I)

$$H_y^I(x,z) = Ae^{-jk_x^I x} + Be^{jk_x^I x}$$

$$H_y^I(x,z+NL) = H_y(x,z)e^{-j\beta NL}$$

$$\tag{9}$$

$$E_z^I(x,z) = -\frac{k_x^I}{\omega\varepsilon_0}\left(Ae^{-jk_x^I x} - Be^{jk_x^I x}\right)$$

$$E_z^I(x, z + NL) = E_z^I(x, z)e^{-j\beta NL}$$

Region (II)

$$H_y^{II} = \sum_{n=-\infty}^{n=+\infty} A_n e^{-j\left(\frac{2n\pi}{L}+\beta\right)z} e^{-jk_{xn}^{II}x}$$

$$E_x(x, z) = \frac{1}{\omega\varepsilon_0} \sum_{n=-\infty}^{n=+\infty} A_n\left(\frac{2n\pi}{L}+\beta\right)e^{-j\left(\frac{2n\pi}{L}+\beta\right)z}e^{-jk_{xn}^{II}x} \qquad (10)$$

$$E_z(x, z) = -\frac{1}{\omega\varepsilon_0} \sum_{n=-\infty}^{n=+\infty} A_n k_{xn}^{II} e^{-j\left(\frac{2n\pi}{L}+\beta\right)z}e^{-jk_{xn}^{II}x}$$

Under the assumption that $W < \lambda/2$ only a TEM mode is present in the groove and in the set of equations (9) $k_x^I = k_0$. In (9) the second equation states that the electromagnetic field into the grooves do not change but a phase contribution which is accumulated at each cell. This is essential to satisfy the matching of tangential components between internal and external tangential fields at the grooves aperture. In (10) one has

$$k_0^2 = k_{xn}^{II}{}^2 + \left(\frac{2n\pi}{L}+\beta\right)^2 \qquad (11)$$

Considering a surface waves which attenuates along x direction one can pose $k_{xn}^{II} = -j\alpha_{xn}^{II}$. Equation (11) then becomes

$$k_0^2 = -\alpha_{xn}^{II}{}^2 + \left(\frac{2n\pi}{L}+\beta\right)^2 \qquad (12)$$

The expansion presented in equations (9) and (10) have to be matched at the interface between region (I) and region (II).

$$H_y^I(d,z) = H_y^{II}(d,z) \qquad NL + t < z < NL + W$$

$$E_x^{II}(d,z) = 0 \qquad NL < z < NL + t$$

$$\text{(13)}$$

$$E_x^I(d,z) = E_x^{II}(d,z) \qquad NL + t < z < NL + W$$

$$E_x^I(0,z) = 0 \qquad NL + t < z < NL + W$$

The last of equation in (13) states that the tangential components of the electric field is zero at $x = 0$. When this condition is used the expressions for H_y and E_z in (9) become

$$H_y^I(x,z) = 2A\cos(k_0 x)$$

$$\text{(14)}$$

$$E_z^I(x,z) = 2jA\frac{k_x^I}{\omega\varepsilon_0}\sin(k_0 x)$$

The continuity of the electric and magnetic tangential components for $x = d$ results into the following equations

$$A\cos(k_0 d) = \sum_{n=-\infty}^{n=+\infty} A_n e^{-j\left(\frac{2n\pi}{L}+\beta\right)z} e^{-jk_{xn}^{II}d} \qquad NL$$

$$+ (L - W) < NL + W$$

$$jA\frac{k_0}{\omega\varepsilon_0}\sin(k_0 d) \qquad \text{(15)}$$

$$= -\frac{1}{\omega\varepsilon_0}\sum_{n=-\infty}^{n=+\infty} A_n k_{xn}^{II} e^{-j\left(\frac{2n\pi}{L}+\beta\right)z} e^{-jk_{xn}^{II}d} \quad NL$$

$$+ (L - W) < NL + L$$

$$0 = -\frac{1}{\omega\varepsilon_0} \sum_{n=-\infty}^{n=+\infty} A_n k_{xn}^{II} e^{-j\left(\frac{2n\pi}{L}+\beta\right)z} e^{-jk_{xn}^{II}d} \qquad NL < z$$

$$< NL + (L - W)$$

where the factor 2 is now included in the coefficient A. It is easy to demonstrate that functions $e^{-j\left(\frac{2n\pi}{L}+\beta\right)z}$ are orthogonal on the interval $[0, L]$ having

$$\int_0^L e^{j\left(\frac{2m\pi}{L}+\beta\right)z} e^{-j\left(\frac{2n\pi}{L}+\beta\right)z} dz = \delta_{nm} L$$

Testing equations (15) with $e^{j\left(\frac{2m\pi}{L}+\beta\right)z}$ and integrating along z between $-L/2$ and $L/2$ (for convenience the origin of the axis is now considered at the center of the groove) one has

$$A\cos(k_0 d)\, sinc(\beta_m d) = A_m e^{-jk_{xm}^{II}d}$$

(16)

$$jAk_0 \sin(k_0 d)\, sinc(\beta_m)d = -A_m k_{xm}^{II} e^{-jk_{xm}^{II}d}$$

where $\beta_m = 2m\pi/L + \beta$.

Considering now that for a surface wave in region (II) one has $k_{xm}^{II} = -j\alpha_{xm}^{II}$ with $\alpha_{xm}^{II} > 0$, by dividing the second equation in (16) by the first one, one obtains the following dispersion relation

$$k_0 \tan(k_0 d) = \alpha_{xm}^{II}$$

(17)

Equation (17) is not useful to exactly determine the propagation constant β, but it shows that a surface wave may propagate in region (II) only if $\tan(k_0 d) > 0$, which means that TM surface waves on a corrugated conducting plane have a bandpass/stopband characteristic. In particular, one has surface wave propagation if $n\lambda/2 < d < (2n + 1)\lambda/4$, in particular for $d < \lambda/4$.

The corrugated plane permits also the propagation of waves which are not bound to the conducting surface but that may radiate. Those waves, named leaky waves or fast waves, to distinguish them from the surface waves which propagates with a speed lower than the speed of light, may be excited under certain conditions. In this case the propagation constant along z direction β_n has no more the form taken in the case of surface waves but it can be written as $\beta_n - j\alpha$, which states that as the wave propagates along the corrugations it loses power in form of radiated fields. In this case the propagation constant along x can be expressed as

$$k_{xn}^{II}{}^2 = k_0^2 - \beta_n^2 + 2j\alpha\beta_n \qquad (18)$$

Considering the relation (18) for $\alpha = 0$ and $n = 0$ the $(k_0 L, \beta_0 L)$ plane can be considered.
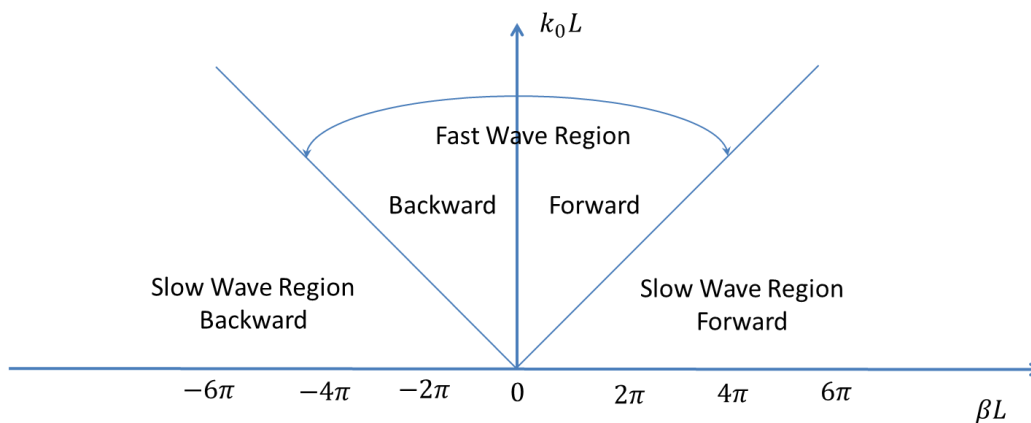

Fig. 3.11 - Radiation and surface wave regions in the k_0 L-β_0 L plane

The regions in Fig. 3.11 correspond to the conditions:

- Fast waves (Radiation) $k_0 > \beta_0 \; or \; k_0/\beta_0 \; > 1$

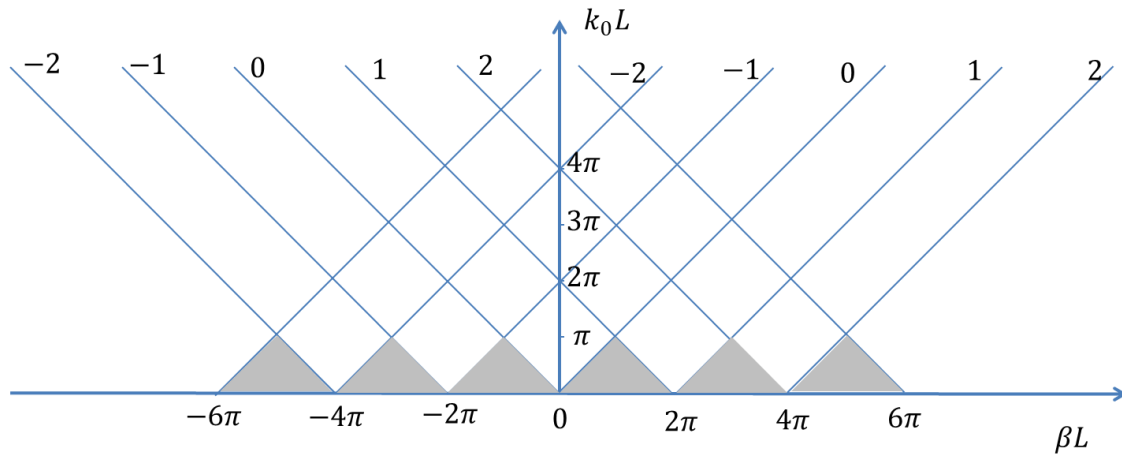- Slow waves (Surface waves) $k_0 < \beta_0 \; or \; k_0/\beta_0 \; < 1$

Fig. 3.12 - Radiation and surface wave regions in the k_0L-β_nL diagram

Considering Floquet harmonics other than $n = 0$, the diagram is periodic as shown in Fig.3.12, where the index of the harmonics up to $n = \pm 3$ is shown. The gray regions correspond to surface waves regions. As it can be seen surface waves do not exist for $k_0L > \pi$, i.e., $L > \lambda/2$.

The considerations shown up to know defined a starting point for the design and the optimisation of the hat feed. In particular one needs grooves with $d < \lambda/4$ and $W < \lambda/2$.

3.2.2.3. Single and Dual and hat feed for a cylindrical reflector

In this section is presented the design of a dual band hat feed for a cylindrical reflector. It is anticipated that a double corrugations is adopted in order to obtain a good performance in terms of both impedance matching and radiation pattern in the bands of interest.
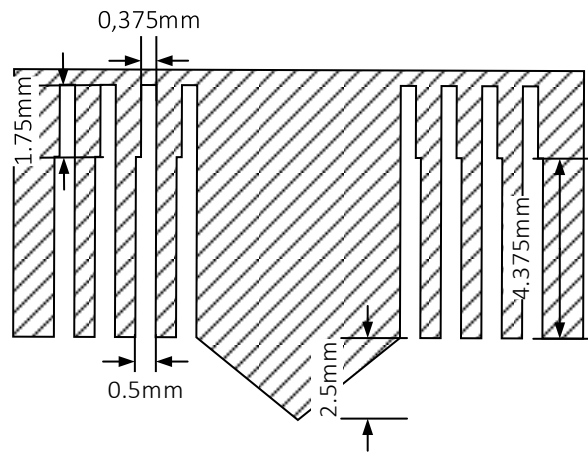
Fig. 3.13 - Dual band Hat feed

As a starting point a first attempt to illuminate the reflector by a hat feed with a single corrugation was done. The had feed has been designed considering only the radiation on the plane of interest (E-plane). The structure of the hat feed is shown in Fig. 3.14. Corrugation depth was firstly set to λ/4 and then quickly optimized. An attempt to find a corrugation length that could be used in both bands of interest was done. The feed has been optimized adjusting length and width of the cusp and length and width of corrugation. To ease a future fabrication process corrugations have been taken of equal length and width instead of using corrugations with different length and width.
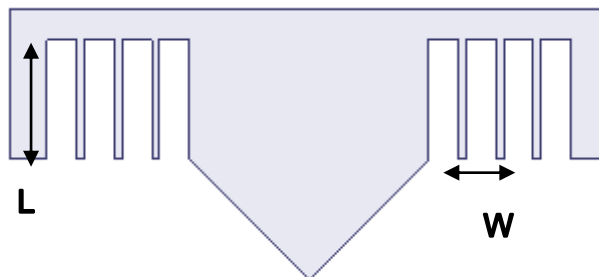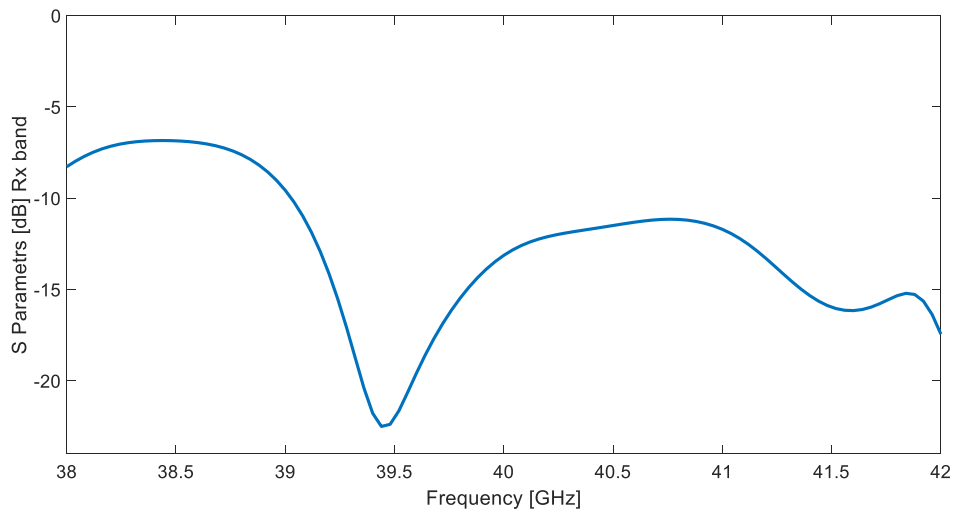

Fig. 3.14 - Hat Feed with a single corrugation

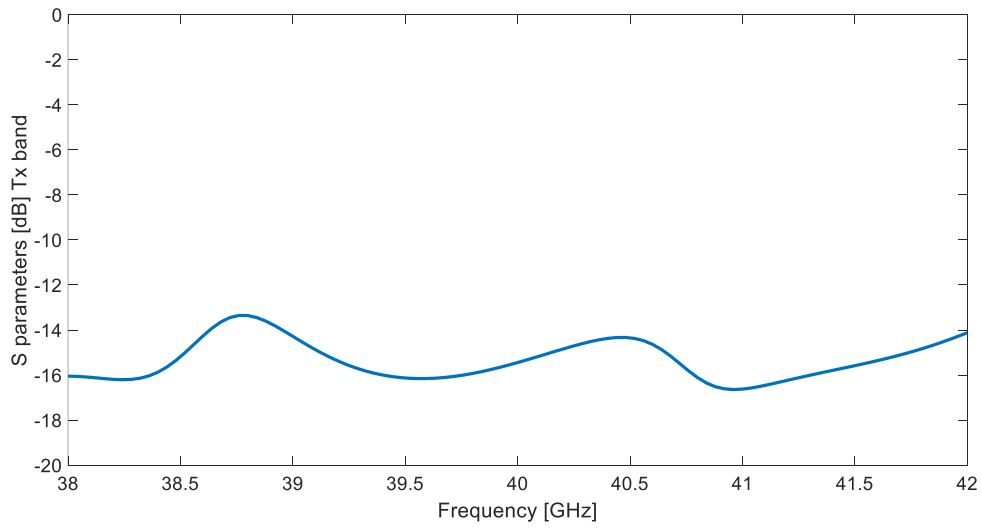*Fig. 3.15 - Reflection coefficient in Rx-band*

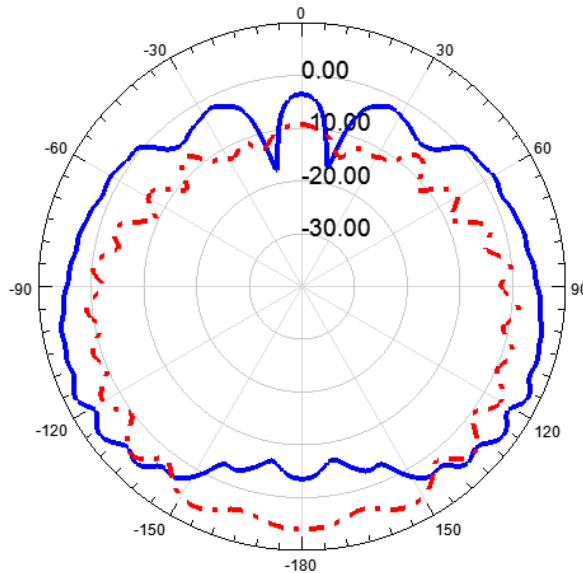*Fig. 3.16 - Reflection coefficient in Tx-band*

Fig. 3.17 - Simulated radiation pattern of the Hat Feed at the 40GHz and 60GHz

The optimized hat feed has a depth (L) of 1mm and width (w) 3mm. Fig. 3.15 and Fig. 3.16 show the simulated S_{11} parameters on the two bands of interest. S_{11} has been considered at the input of the parallel plate that illuminates the feed. Furthermore, in Fig. 3.17 are shown the radiation patterns of the hat feed at 40GHz and 60GHz. As it can be observed, the feed has a good radiation pattern at the lower frequency, with a 8dB roll off, but at the highest frequency the pattern deviates considerably from the other one. This would results in a degraded pattern of the overall antenna with a high level of side lobes. In order to obtain a dual band hat feed two possible solutions could be applied: the using of a dielectric inside the corrugations or the using of a double corrugations. Following the second choice, the previous structure has been modified adding a second corrugation as it is shown in Fig. 3.13. While the depth of both corrugations affect the feed performances, one can say that the shortest corrugation controls the higher band while the longer one controls the lower band. The starting point of the optimization was set the resonance points exactly at the two-mid bands. In

(Fig. 3.18) is shown the input impedance of Fig. 3.14) , length L and width W were chosen to make the structure resonate as shown in Fig. 3.18.

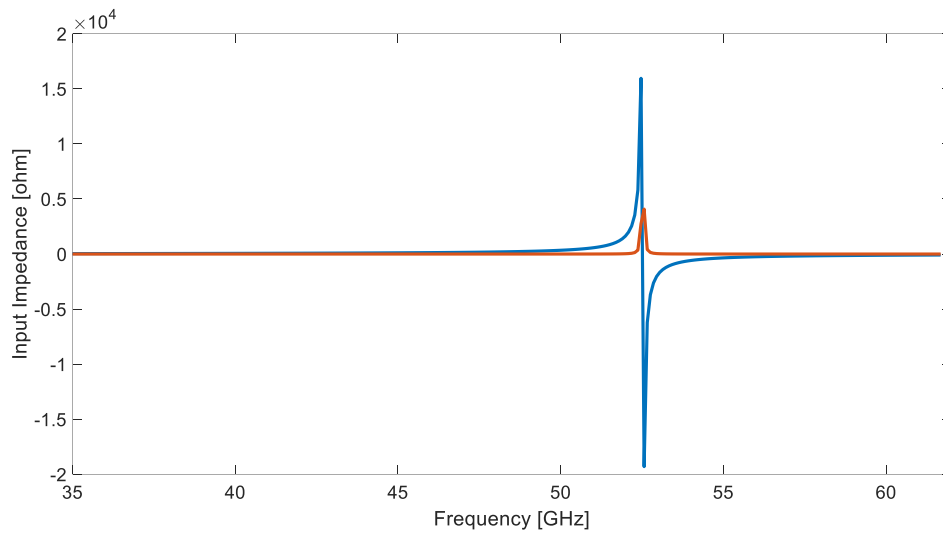*Fig. 3.18 - Input impedance of the single corrugation*

A lengthy optimisation process gave the following geometry:

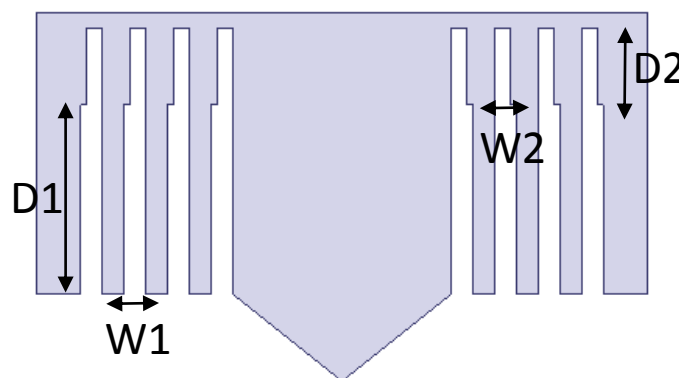$$d_1 = 4.375mm, d_2 = 1.75mm, w_1 = 0.5mm, w_2 = 0.375mm$$

Fig. 3.19 - Hat Feed with a dual corrugations

Where d_1 and d_2 are respectively the depth of the longer corrugation and of the shorter one while w_1 and w_2 are the width (Fig. 3.19).

Length and width of the grooves were optimised trying to have a good level of side lobes and good efficiency over the two bands. Considering the input impedance of the corrugation, as it was done for the starting structure, it is possible to verify that in order to have a propagation of the TM mode, the resonance point is shifted toward to frequencies lower than the starting values (Fig. 3.20).
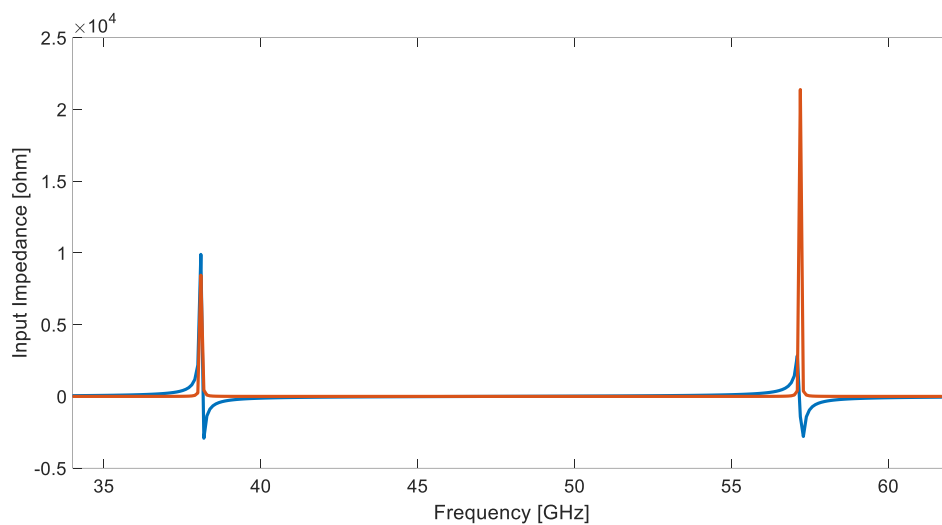
Fig. 3.20 - Input impedance of the dual corrugation at the optimal point

The ratio between the depth of the lower corrugation and the higher one gives the possibility to obtain good performance in both frequency range without degradation on the pattern of the antenna. In order to optimize the illumination of the reflector, a tapering of 8 dB has been realized on the radiation pattern of the hat feed (Fig. 3.21). This behaviour makes possible the reduction of the spillover losses of the overall antenna.

Fig. 3.21 - Simulated radiation pattern of the hat feed with two corrugations at the centre frequency of the two bands

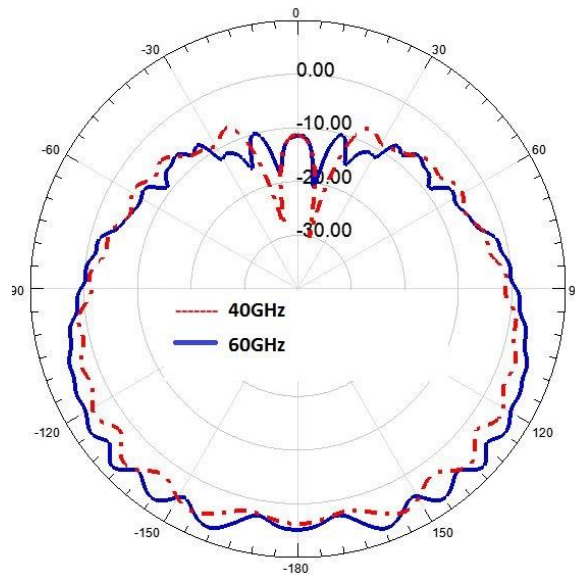A further optimization, in order to minimize the effects of multiple reflections between reflector and feed a Gaussian vertex plate was introduced.

3.2.2.4. Gaussian Vertex plate

Multiple reflections between reflector and feed may have a critical effect on the reflection coefficient and the radiation pattern. By introducing a flat vertex plate at the centre of the reflector, the multiple reflections can be reduced and the reflection coefficient improved. Positive effects have also been seen in terms of reduction of side-lobes levels and increased directivity due to reduced centre blockage and multiple reflections between reflector and feed as investigated in [12]. The contribution of the multiple reflections and its influence on G/T was analysed further in [13] using the method of moment. The evolution of the vertex plates eventually lead to a Gaussian shape for improved performance [14]. The Gaussian vertex plate can make the reflected field from the reflector a null at the focus of the reflector where its feed is located, and this therefore minimizes the degrading effect of the multiple reflections and reduces the diffractions from the

brim of the hat. In addition to this, the Gaussian vertex plate reduces the far-out sidelobes. The derivations lead to the following design formulas for the shape of the Gaussian vertex plate (Fig. 3.22):

$$t = t_0 e^{-(\frac{\rho}{\rho_0})^2},$$

With

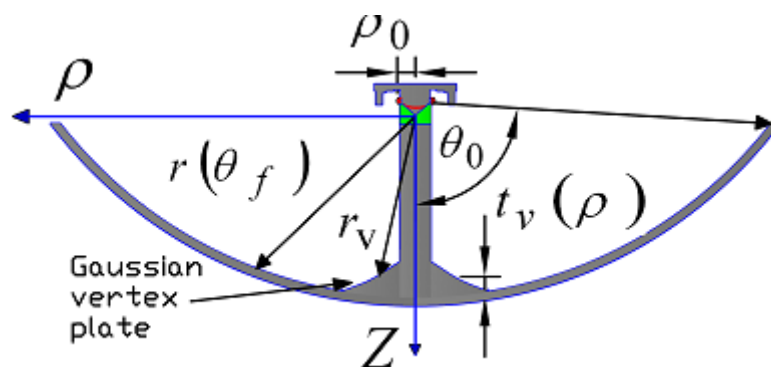$$t_0 = 0.15\lambda \qquad\qquad \rho_0 = 0.5\sqrt{(F\lambda)}$$

Fig. 3.22 - Gaussian vertex plate in a reflector antenna

3.2.3. Cylindrical reflector realization and measurements

Once that all the components of the antenna has been optimized, the dual band cylindrical reflector was simulated, manufactured and measured. The overall structure is proposed in Fig. 3.23- Fig. 3.24
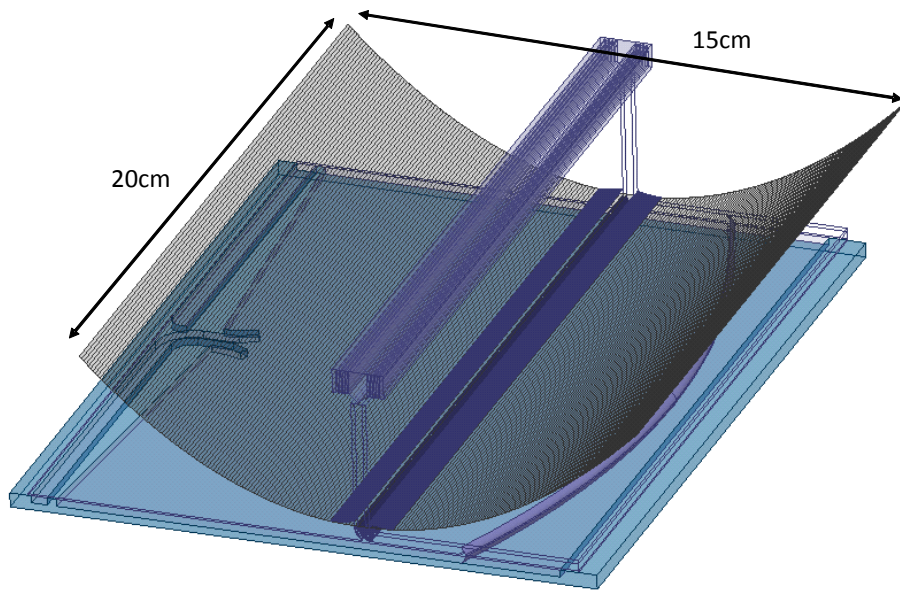
Fig. 3.23 - Simulated structure of the overall antenna in Q-V bands
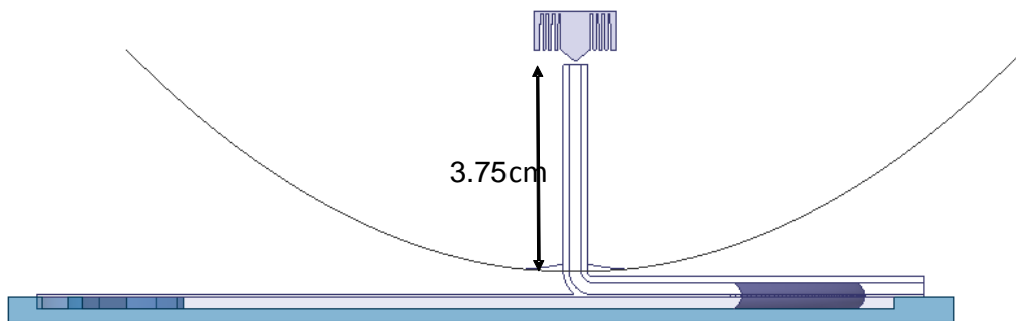
Fig. 3.24 -Frontal view of the overall antenna in Q-V bands

As it was already mentioned, the structure has been designed and simulated in the frequency range of Q-V bands in order to obtain a good candidate for backhaul point of 5G architecture. Due to the high cost of manufacturing, the high precision request in the realization of all component and the difficult to measure the terminal in an anechoic chamber with a good level of precision, it was realized a scaled version of the presented terminal working in the frequency range of 19-21GHz and 29-31GHz. The prototype realized is suitable for the man

transportable antenna application because it has all the requirements explained

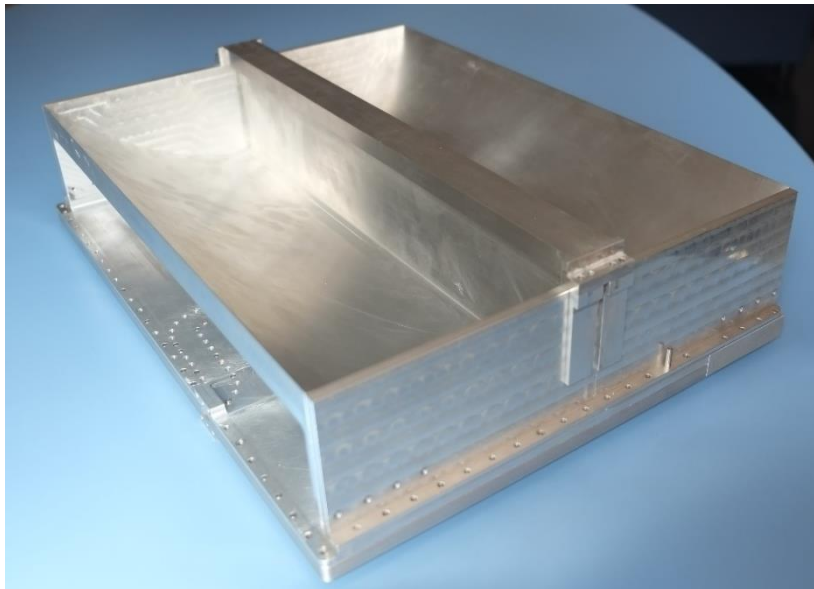previously. The realized prototype is shown in Fig. 3.25 - Fig. 3.26 - Fig. 3.27

Fig. 3.25 - Realized prototype antenna in Ka band

Fig. 3.26 - Top view of the realized antenna in Ka band

Fig. 3.27 - Feeding structure of the realized antenna

The prototype antenna was realized in aluminium and, as it can be seen from the pictures, the simulated structure and realized structure are slightly different because during the designing process it was necessary to add additional components in order to guaranty the structural strength of the prototype. The scaled realized prototype has good performance both in impedance matching and in term of radiation pattern, as it possible to evaluate from the image listed below. In particular, the simulated and measured radiation pattern are in a good agreement in both the bands of interest (Fig. 3.30-38). Furthermore, the behaviour in frequency of the gain is quite good, in fact it presents approximately 0.5dB of losses respect to the simulated behaviour. This is probably due to the manufacturing process of the prototype (Fig. 3.39-Fig. 3.40).

Fig. 3.28 - Measured S11 (Rx band)
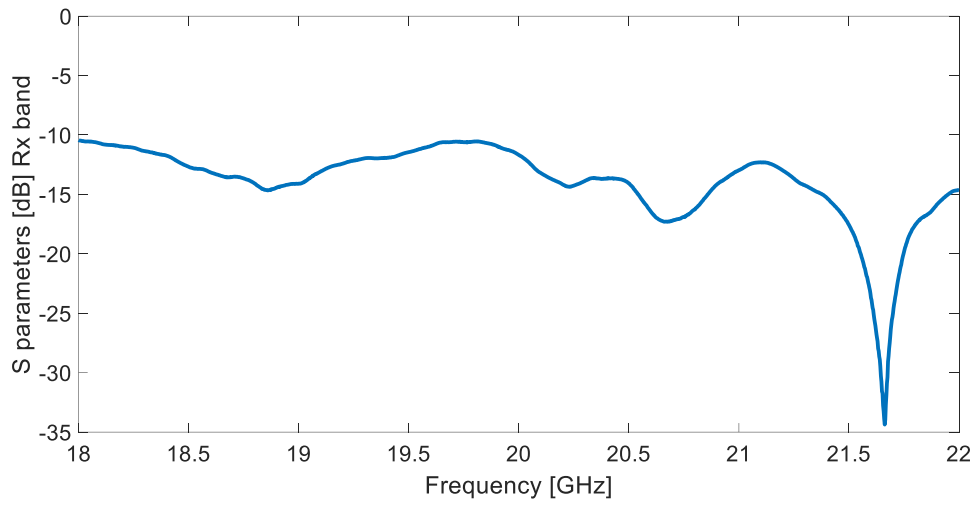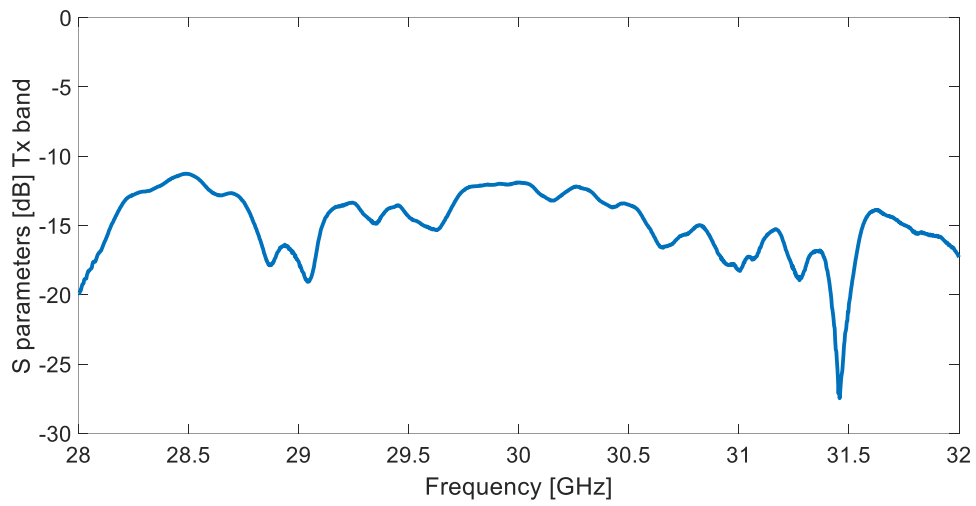

Fig. 3.29 - Measured S11 (Tx band)

Fig. 3.30 - Comparison between simulated and measured results (Plane E) at 19GHz

Fig. 3.31 - Comparison between simulated and measured results (Plane H) at 19GHz

Fig. 3.32 - Comparison between simulated and measured results (Plane H) at 20GHz

Fig. 3.33 - Comparison between simulated and measured results (Plane E) at 20GHz
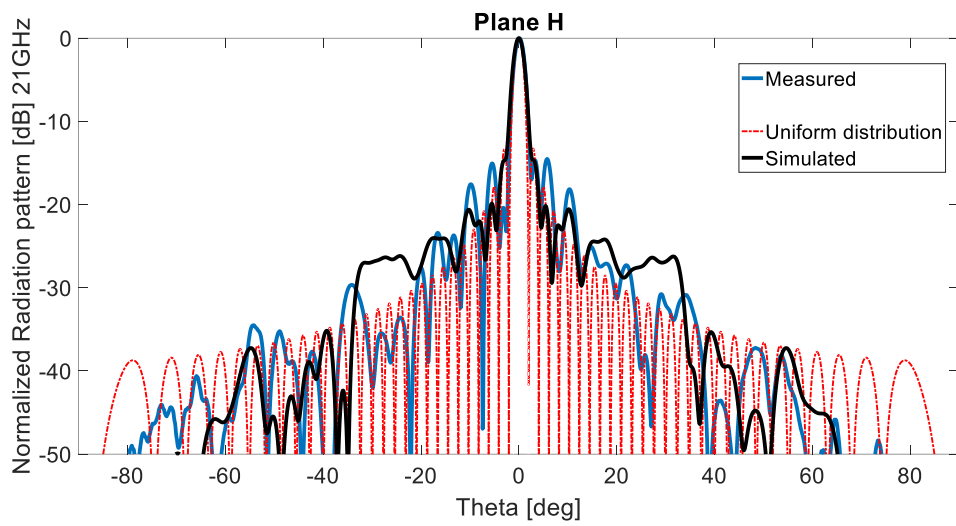
Fig. 3.34 - Comparison between simulated and measured results (Plane H) at 21GHz
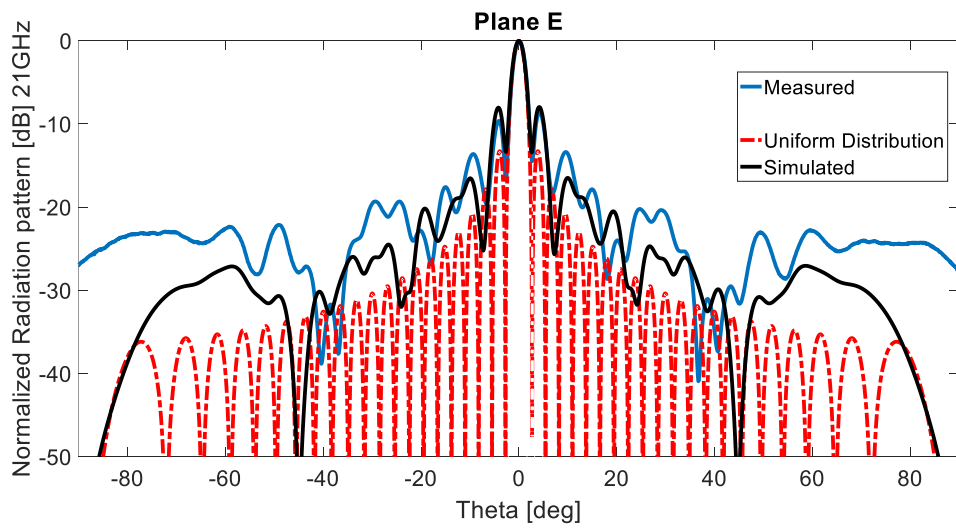
Fig. 3.35 - Comparison between simulated and measured results (Plane E) at 21GHz
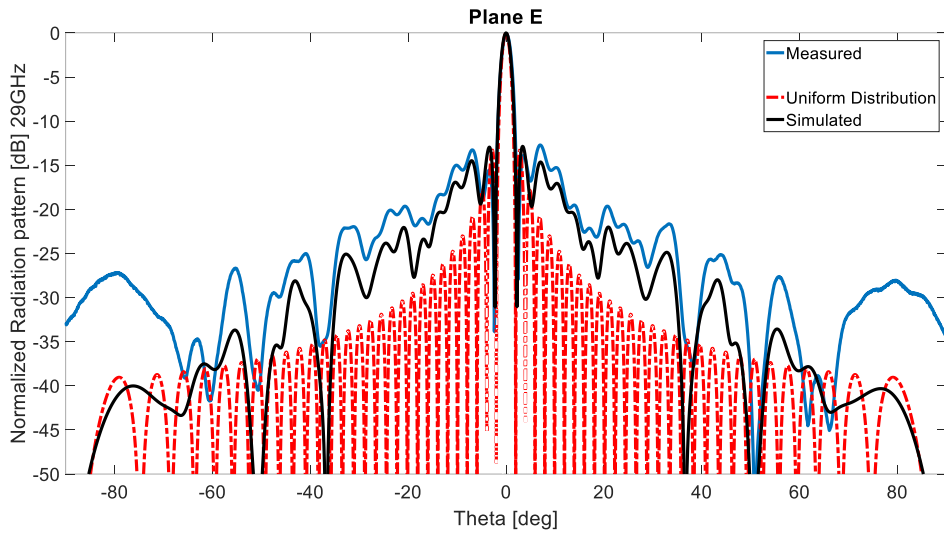
Fig. 3.36 - Comparison between simulated and measured results (Plane E) at 29GHz
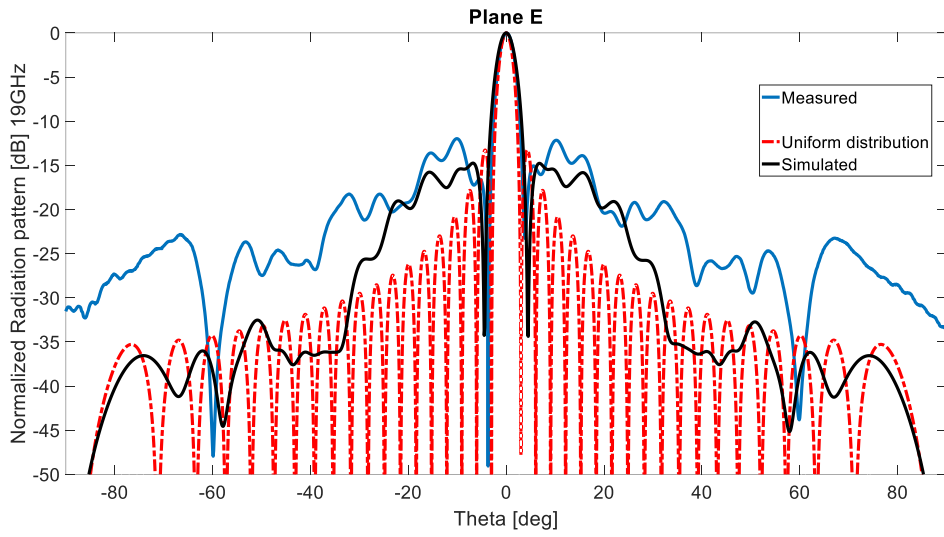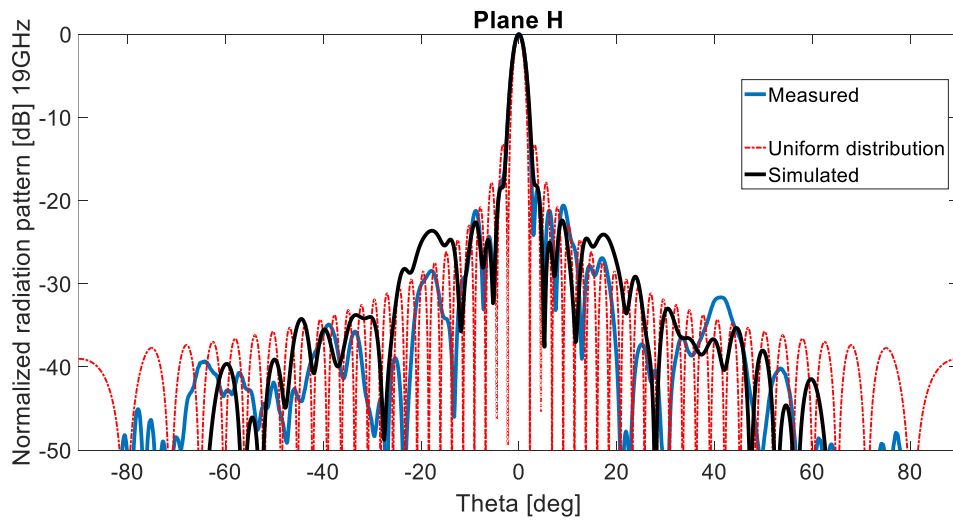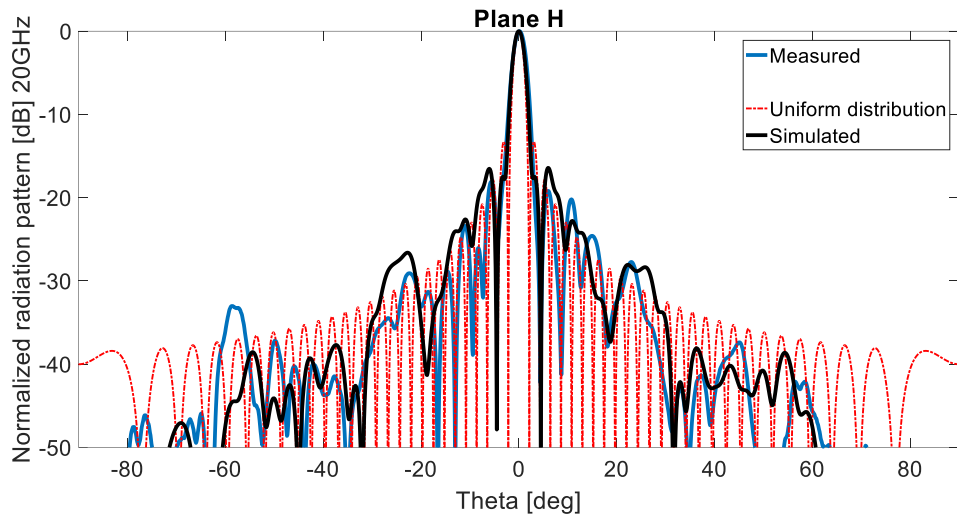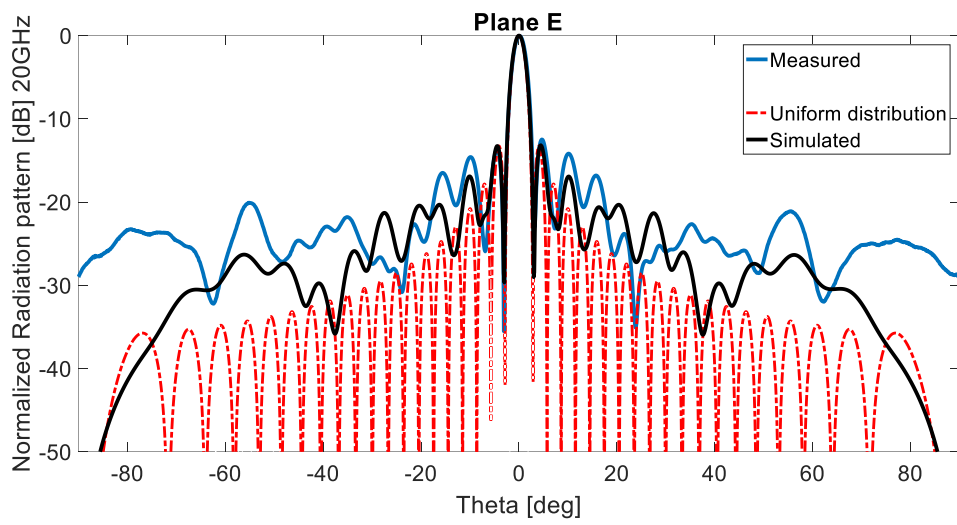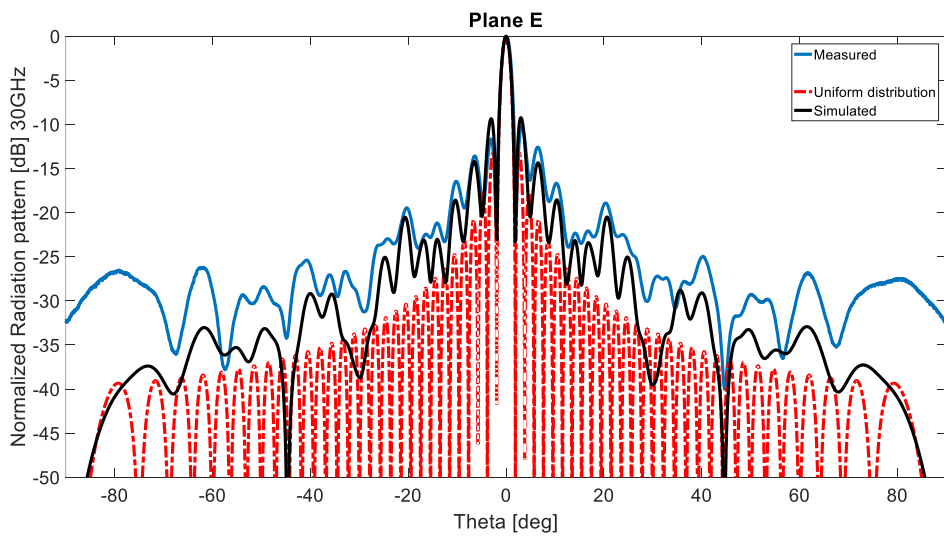

Fig. 3.37 - Comparison between simulated and measured results (Plane E) at 30GHz
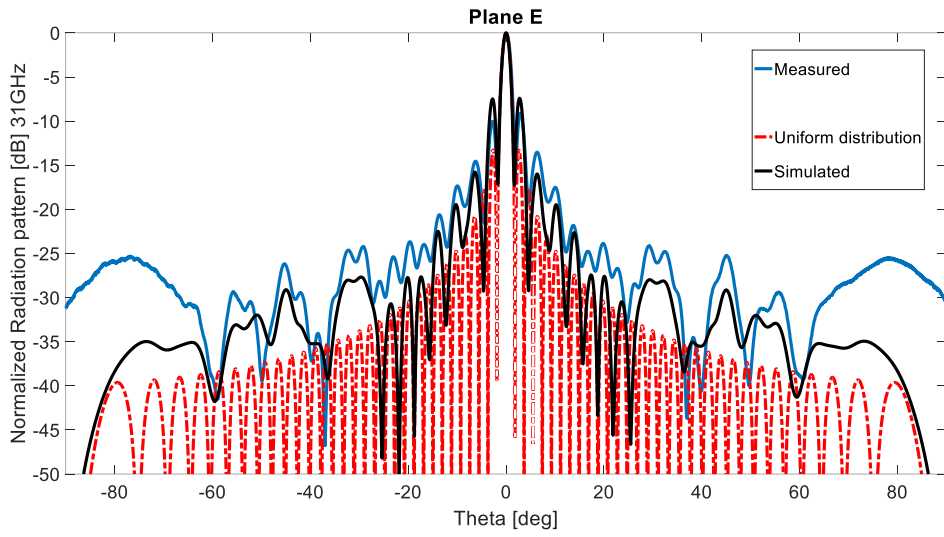
Fig. 3.38 - Comparison between simulated and measured results (Plane E) at 31GHz
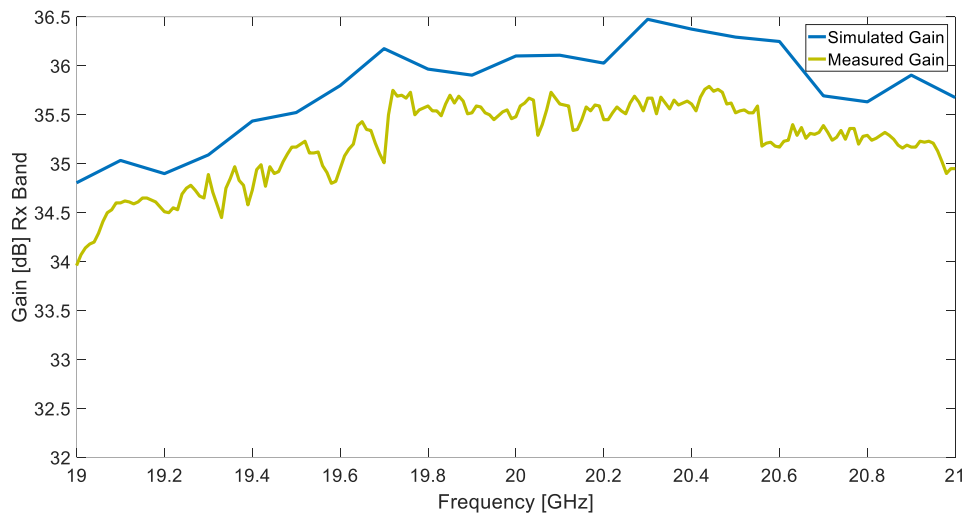
Fig. 3.39 -Comparison between simulated and measured gain (Rx Band)
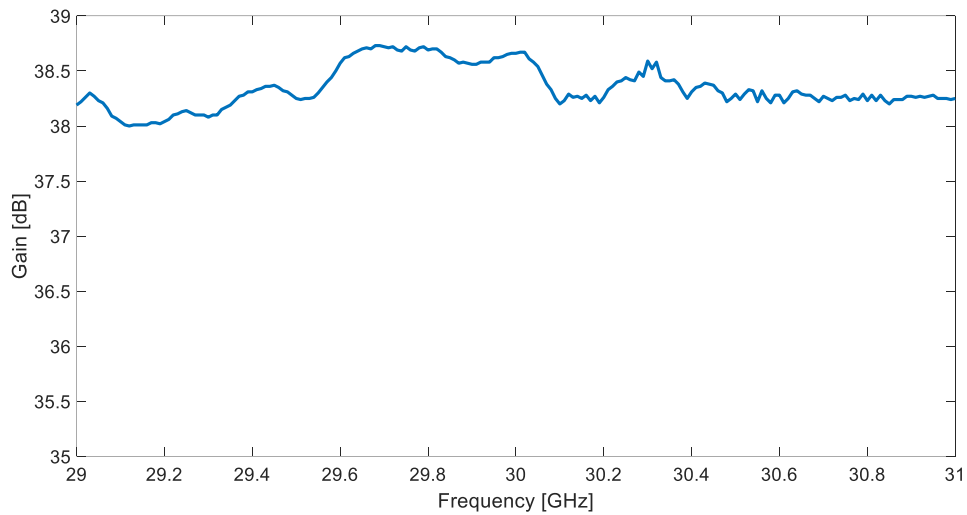
Fig. 3.40 - Measured gain (Tx Band)

The scaled, Ka band, prototype is intended to be used in satcom applications. In these applications is important evaluate how the radiation patterns fits the regulations on Power Spectral Density masks. Fig.3.41 provides a comparison of ESD mask restrictions defined in the ETSI, ITU-R, MIL-STD and FCC regulatory standards. As it can be seen, commercial Ka band ESD are particularly stringent. This restriction is adopted to enable commercial Ka-band satellites to achieve 2-degree separation across the orbital arc, to allow Ka-band satellite frequency reuse.
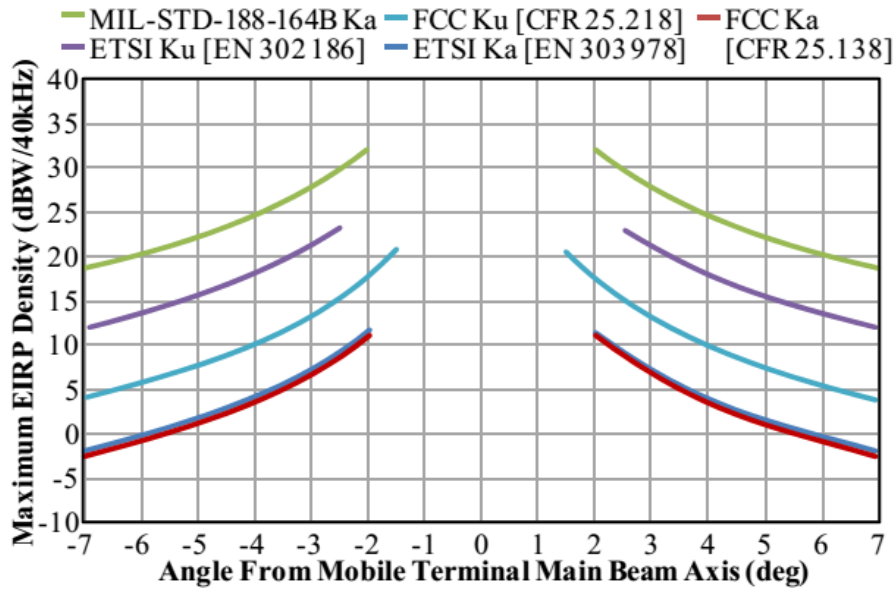
Fig. 3.41 - Mask Comparison

The evaluation of the EIRP Spectral Density is done outside principal plane and considering the plane at 45°. Fig. 3.42-43-44 show the performance of the prototype along the plane 45°. As it possible to see, the radiation pattern of the antenna along this plane respects the restriction imposed by ETSI standard.
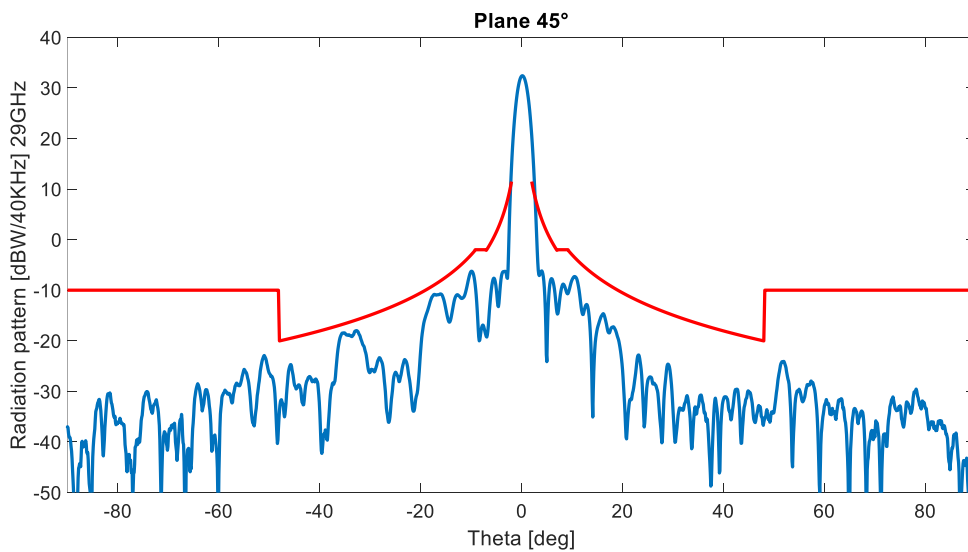
Fig. 3.42 - Radiation pattern of the terminal along the plane 45° at 29GHz
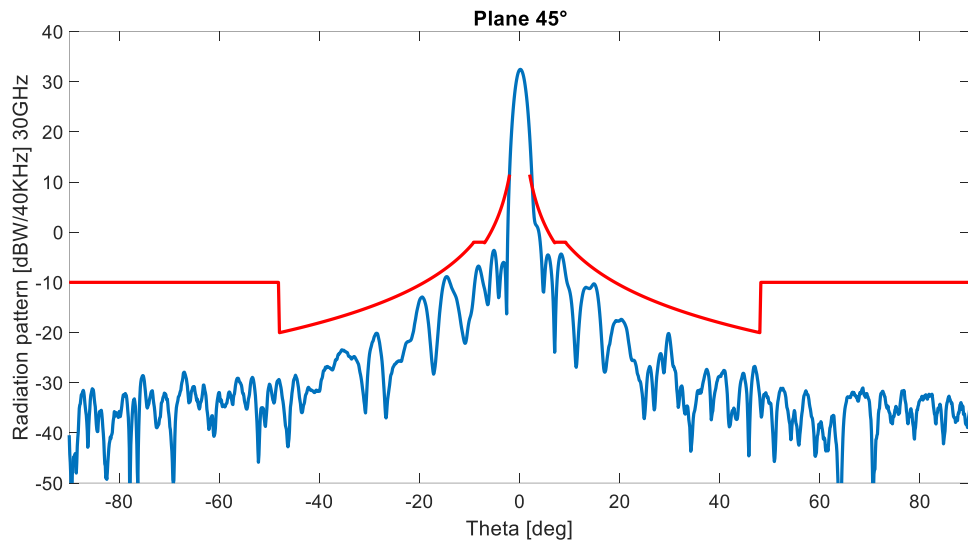
Fig. 3.43 - Radiation pattern of the terminal along the plane 45° at 30GHz
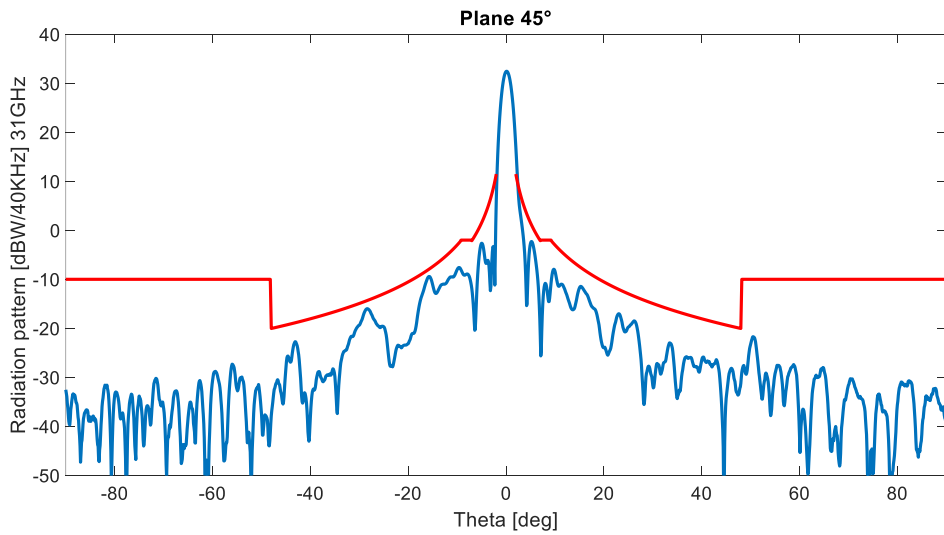
Fig. 3.44 - Radiation pattern of the terminal along the plane 45° at 31GHz

4. Segmented Reflectarray

As it was already stated in the previous chapter, the main characteristics of the man transportable antenna is the lightweight and its reduced profile. The cylindrical reflector presented in the previous chapter is limited by the f/D factor. In fact, once height and diameter of the antenna are given, f/D is fixed. A larger diameter would then results in a higher antenna profile. In order to solve the problem and to have larger aperture without increasing the antenna height, a novel approach is evaluated in which the parabolic reflector is replaced with a segmented reflectarray. As it will be shown, this allows for with a larger aperture without moving the feed position.

4.1. State of the art

Reflectarrays combine some of the advantages of reflector and of array antennas. A feed illuminates a usually planar reflecting surface with locally controlled surface impedance to produce a fixed or reconfigurable radiation pattern. In practice, the reflecting surface is often a planar array where the power accepted by each element is re-radiated with a prescribed phase. Element phases can be fixed to produce a fixed beam or tuneable to scan or reconfigure a beam. The advantage over regular phased arrays are simplicity and low loss of the power distribution scheme, potentially associated with the low cost and mass of a printed structure. Also, for a large aperture, a reflectarray in flat panel can easier manufactured and deployed than a large/shaped reflector. Main limitations are the narrow bandwidth, the uncontrolled reflection of some of the incident power.

The protrusion of the feed can also be a problem, in particular for vehicle antennas. Phase or time shifter losses, control and costs are also issues. Fixed beam reflectarrays were proposed for pencil beam or shaped beam applications where they can potentially achieve lower mass, easier deployment and/or lower cost than (large) reflectors or array that would produce the same beam. In early designs, patches with stubs of unequal lengths were proposed by Munson et al [15] and implemented by Huang [16] [17]. Patches and printed dipoles of variable size were analysed and promoted by Pozar [18]. These single layer design have a few percent of bandwidth. They can optimistically provide 55% aperture efficiency for a pencil beam and can produce shaped beam.

4.2.   Segmented reflectarray

The segmented reflectarray is shown in Fig. 4.1 (a) – (b) .The structure is derived from the Ka band reflector presented in the previous section with only the reflectors changed. So, in this case also a TEM wave is lauched by an H plane horn in a parallel plate waveguide which radiates toswards a feed which in turn illuminates the reflectr. The targeted frequency is 20GHz. No specifications on bandwidth is given as the design has an evaluation purpose only.
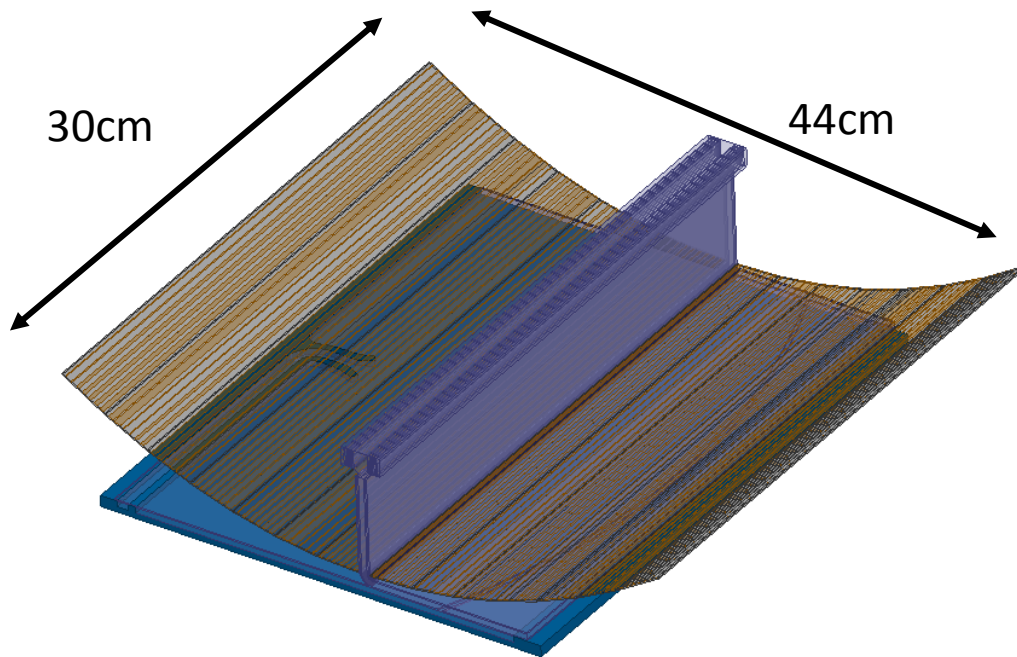
Fig. 4.1(a) - Segmented Reflectarray
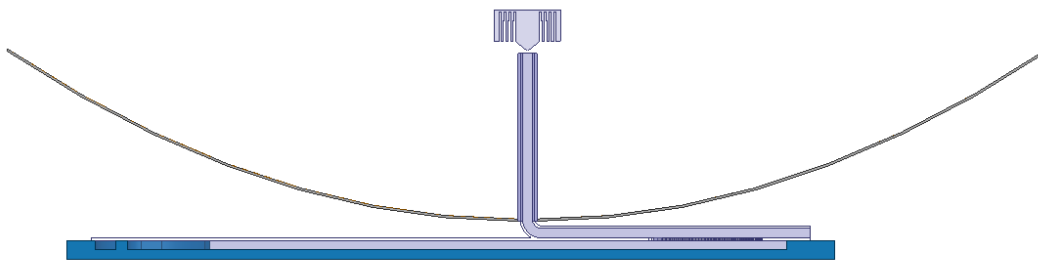
Fig. 4.1 (b) - Section view of the Segmented Reflectarray

Reflectarray elements are striplines which resonate along the antenna E-plane direction. This choice for the radiating elements maintains the antenna linear polarization and facilitate the optimization of the radiators. The structure of the unit cell is proposed in Fig.4.2. The unit cell was simulated with Ansoft HFSS. A periodic boundary condition (Master and Slave) was applied to the elementary cells along the E-plane while H condition where applied on the other boundaries. The cell was illuminated by a plane wave with different angles of incidence.
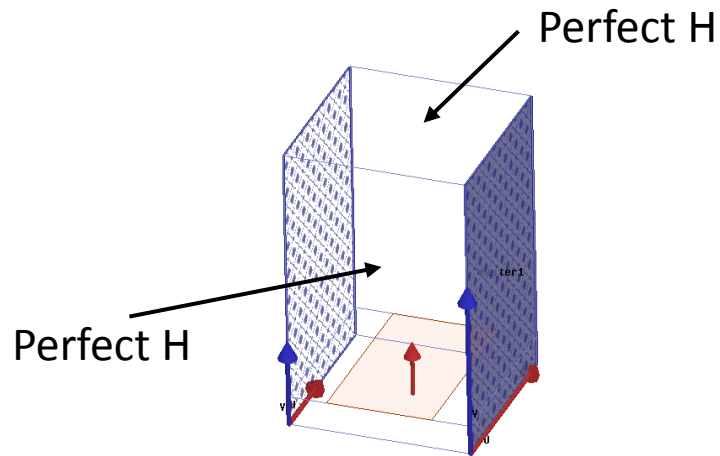
Fig. 4.2 - Boundary conditions for the simulations of the unit cell of the reflectarray

An extensive campaign of simulations was performed to relate strip width, angle of incidence and strip resonant frequency. The performance of the unit cell in terms of phase and amplitude of the reflection signal are reported in Fig.4.3and Fig.4.4. To obtain a beam in the broad side direction, the following phase condition must be satisfied for each cell of the reflectarray:

$$\varphi = -kr + \varphi_s = 0$$

where kr is the phase shifting related to the distance between the element and the feed while φ_s is the compensated phase obtained varying the dimension of the re-irradiating element.
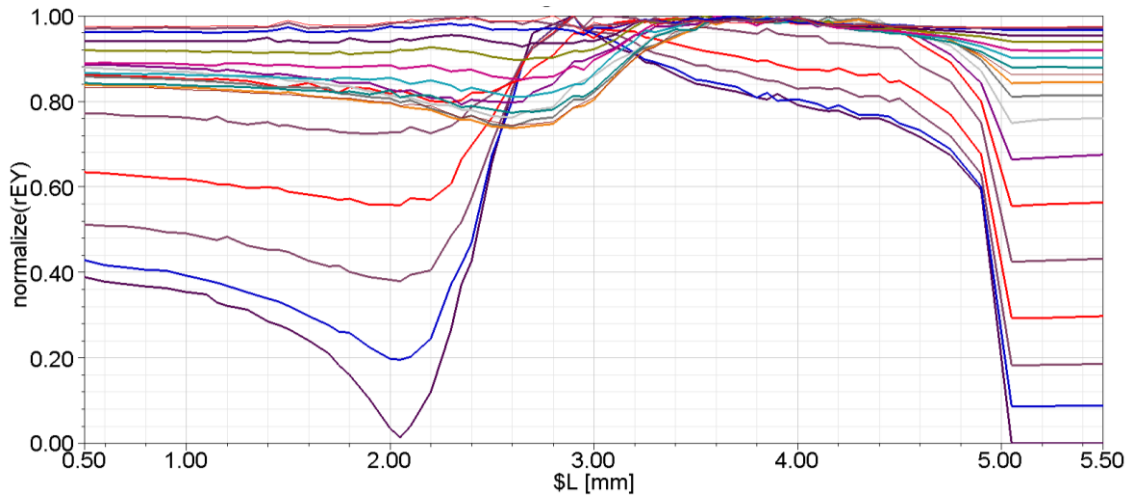
Fig. 4.3 - Amplitude response of the reflection signal of the unit cell
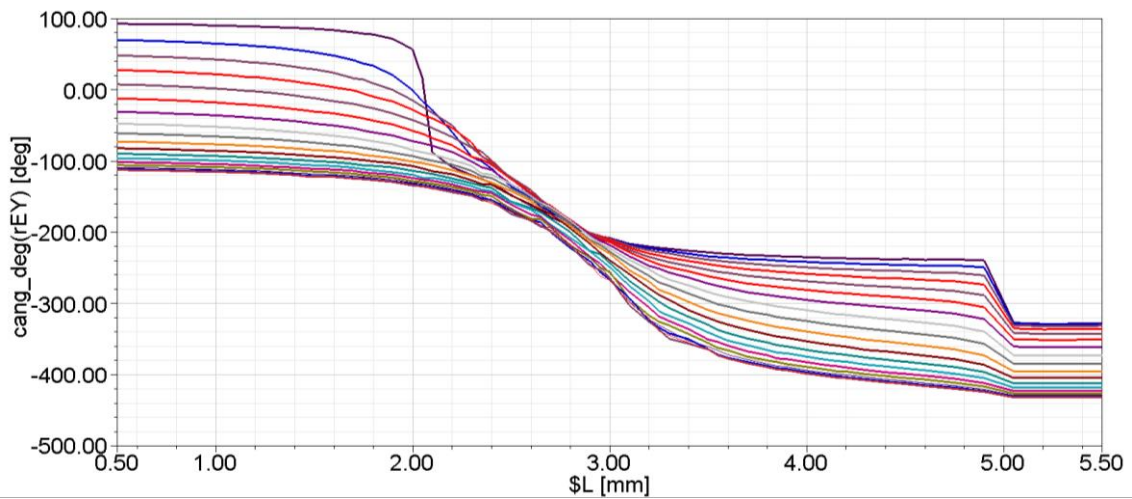
Fig. 4.4 - Phase response of the reflection signal of the unit cell

The results of the unit cell show a stable behaviour both in phase and amplitude and it is possible to obtain a phase shifting of 300°.

In order to maximize the power collected by each cell of the transmitarray, it is important to evaluate the distance between each element and the pattern of the feed. Thanks to the previous results, it was calculated the energy captured by each patch as mentioned in [39]. The efficiency of the overall structure was evaluated as following:

$$\eta = \eta_{SO} + \eta_{IL}$$

Where η_{SO} is the spillover efficiency $\left(\frac{P2}{P1}\right)$, that is the power captured by the reflectarray divided by the total power radiated by the feed, while $\eta_{IL} = \left(\frac{P3}{P1}\right)$ is the insertion loss of the unit cell as shown in the Fig. 4.5.
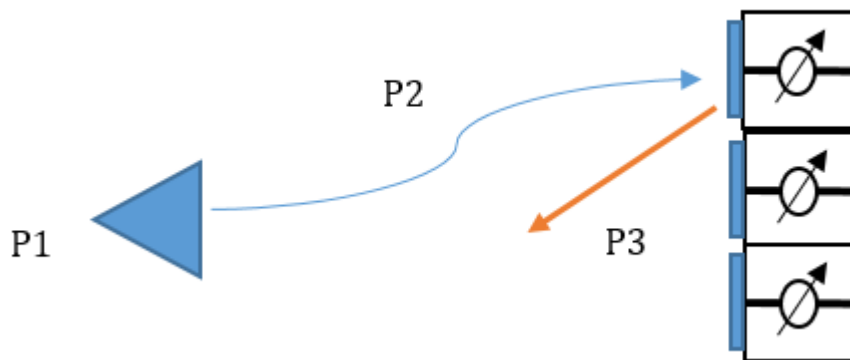
Fig. 4.5 - Schematic structure of the reflectarray

In Fig. 4.6- Fig. 4.7(b) is shown the efficiency of the overall structure under test in two different situation respectively. In the first one it was considered the efficiency related to the element spacing (Fig. 4.6) while the second one shows the efficiency considering the variation of the radiation pattern through which the structure is illuminated.
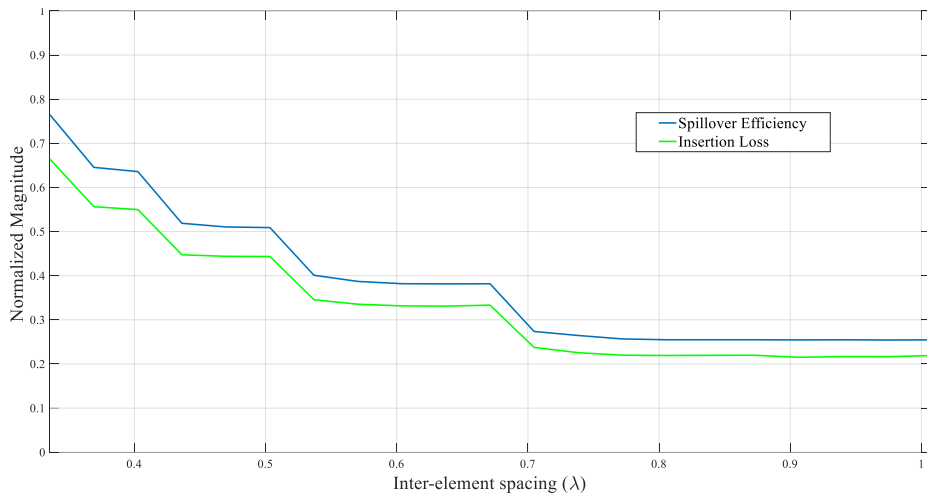
Fig. 4.6 - Efficiency of the reflectarray related to the inter-element spacing
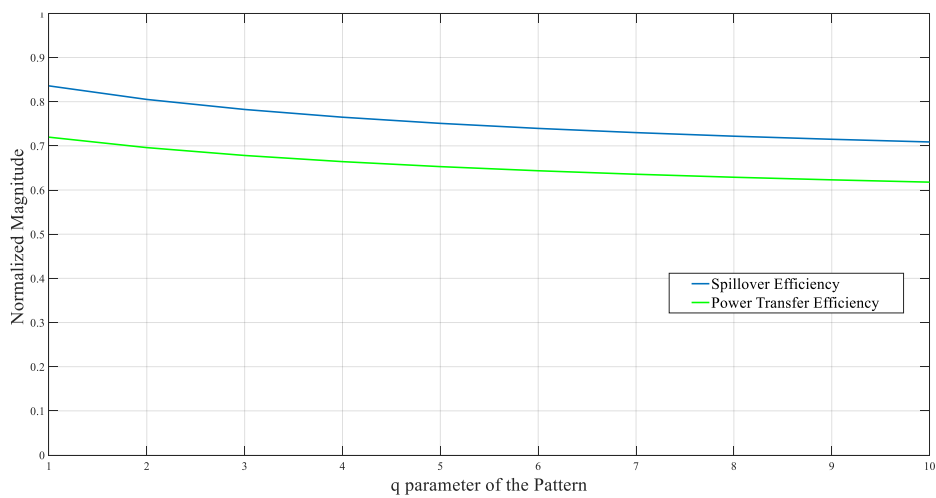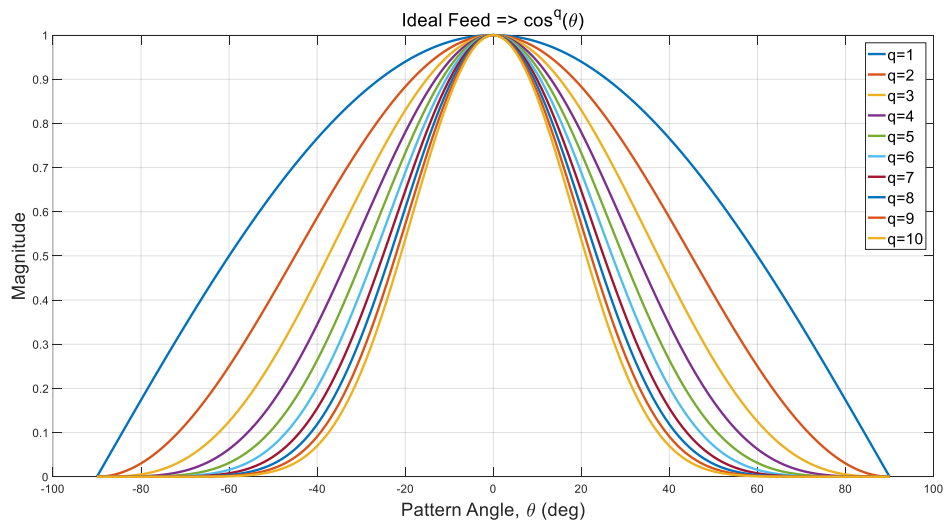
Fig. 4.7 - Efficiency of the reflectarray(b) considering different radiation pattern (a)

The results show that the efficiency is higher when the distance between the elements is lower. This behaviour depends on the increased energy captured by each patch. Furthermore, a lower inter-element spacing reduces the effect of the reflection of the ground plane that could produce unwanted effects in the radiation pattern of the antenna. In Fig.4.7 (b) it is possible to evaluate that the using of a non-directive beam increase the efficiency of the overall structure.
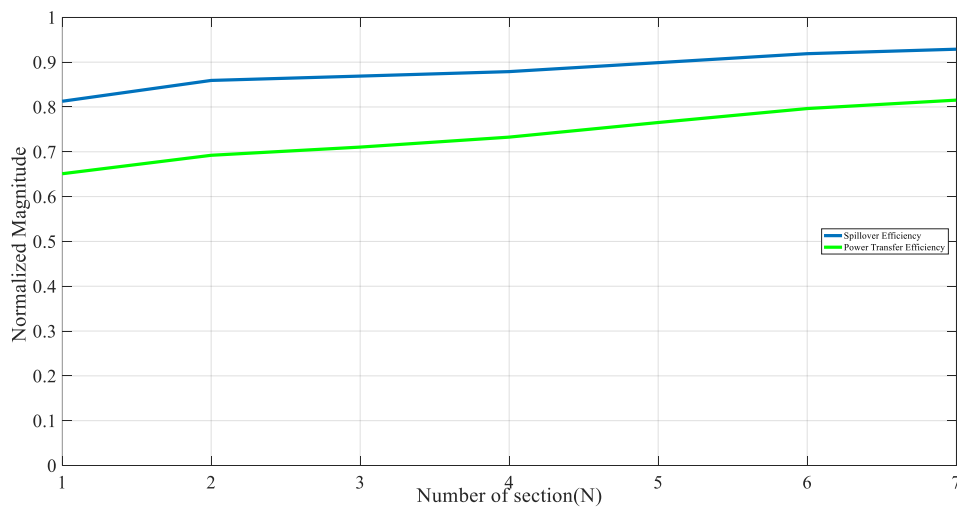
Fig. 4.8 - Efficiency of Reflectarray related to number of segment

A further analysis refer to the number of elements in the segmented reflector. In Fig.4.8 is shown the aperture efficiency of a segmented reflectarray vs the number of segment used to realize the reflector. The reflector diameter is 44cm. The reflector is illuminated with a feed corresponding to a $\cos^q(\theta)$ distribution with q=1. As it is possible to see from Fig.4.8, the aperture efficiency increases as the number of segment increases.

Based on the previous consideration a 14 segments reflectors (7 segments per side) has been designed. The inter-element spacing od the strip was taken at $\lambda/3$. In principle a feed should be designed to improve the radiation

characteristics of the antenna. However, to speed up the production phase and to reduce costs of the experiments the Hat Feed designed for the Parabolic Cylindrical Reflector, presented in the previous chapter, has been used to illuminate the reflectarray.

4.3.　　Simulated and measured results

The segmented reflectors has been simulated with HFSS. In figure Fig.4.9 is shown the return considered at the mouth of the feeding parallel plate. The structure has a good impedance matching (Fig.4.9) on the Ka RX band (19-21GHz). To better understand how the segmented reflectarray works, the distribution of the field both in magnitude and phase has been evaluated at midline along the aperture and compared with the ones of the conventional cylindrical reflector. The two cases, presented in Fig. 4.10 and Fig. 4.11, compares well in both phase and amplitude. The largest difference is found in points just below the feed where the segmented structure suffer of a larger blockage. This is probably due the absence of the vertex. In Fig.4.12 is shown the Gain of the reflectarray vs. frequency. Unlike the parabolic reflector, the gain of the reflectarray is more narrow band (20GHz). This is obviously explained as the reflector relies on the strip resonances.
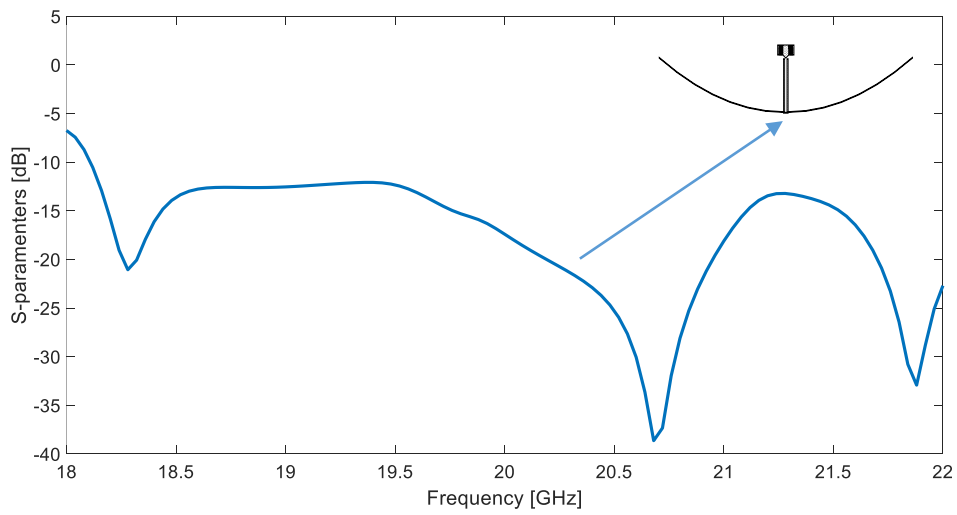
Fig. 4.9 - S-parameters of Segmented Reflectarray
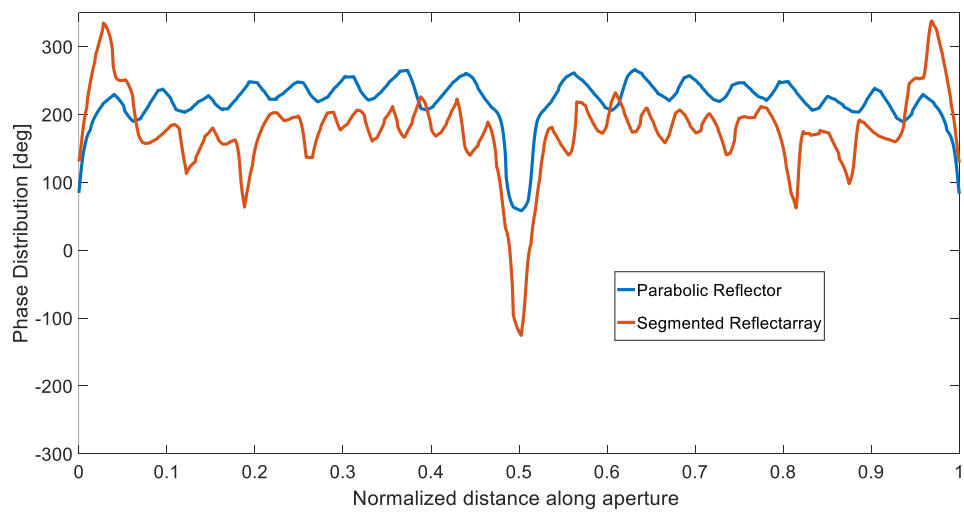
Fig. 4.10 - Comparison of phase distribution along the aperture in the Parabolic Reflector and Segmented Reflectarray
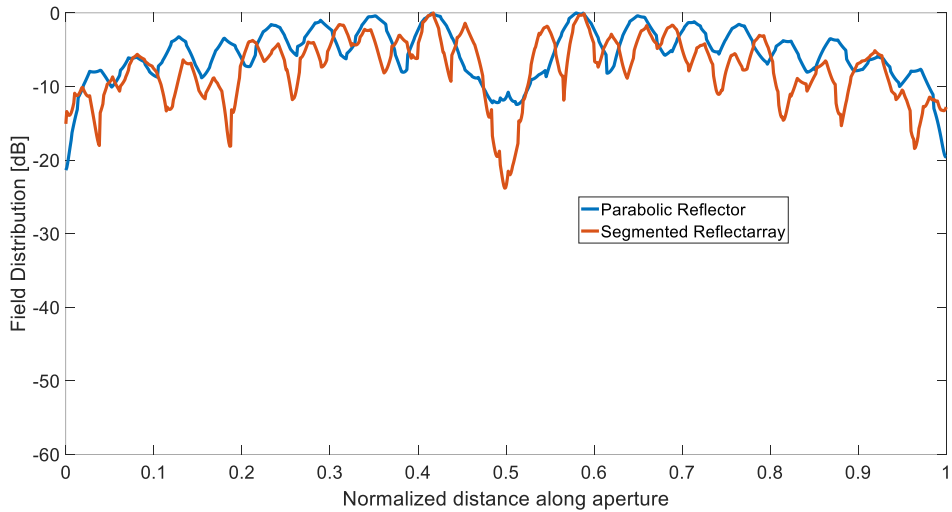
Fig. 4.11 - Comparison of field distribution along the aperture in the Parabolic Reflector and Segmented Reflectarray
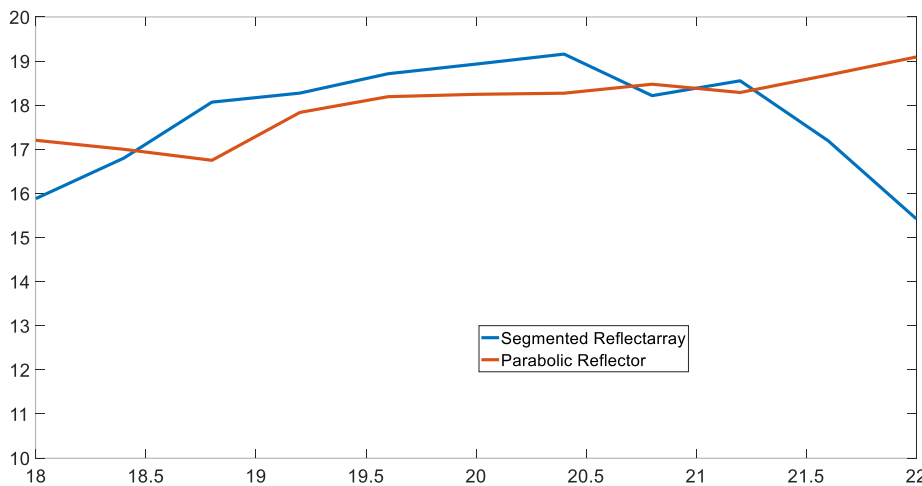
Fig. 4.12 - Comparison of gain performance along the band of interest in the Parabolic Reflector and Segmented Reflectarray

A prototype of the segmented reflectarray has been realized, as shown in and Fig. 4.13. The feeding structure of the cylindrical reflector antenna presented previously has been used. The measurements process has been started but only the radiation pattern of the overall structure has been evaluated yet. As it is possible to see from Fig. 4.14, the measured radiation pattern at the working

frequency of 20GHz presents a relatively good agreement with the simulated radiation pattern.
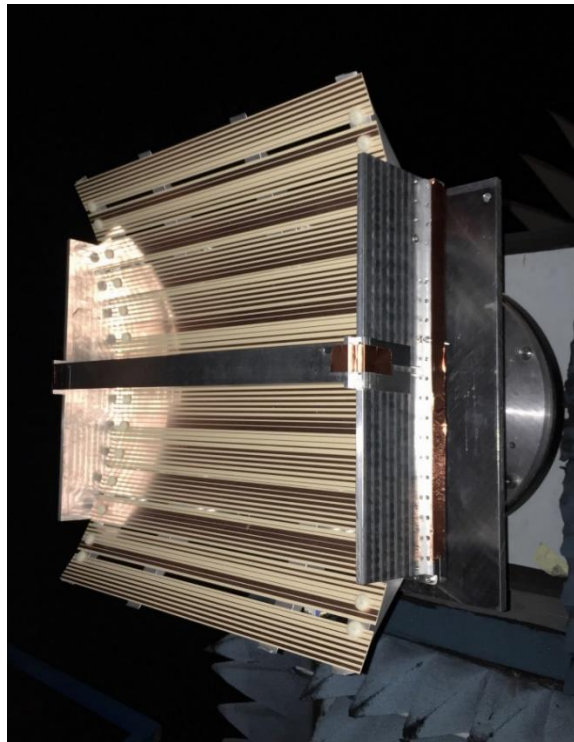
Fig. 4.13 - Section view of the segmented reflectarray
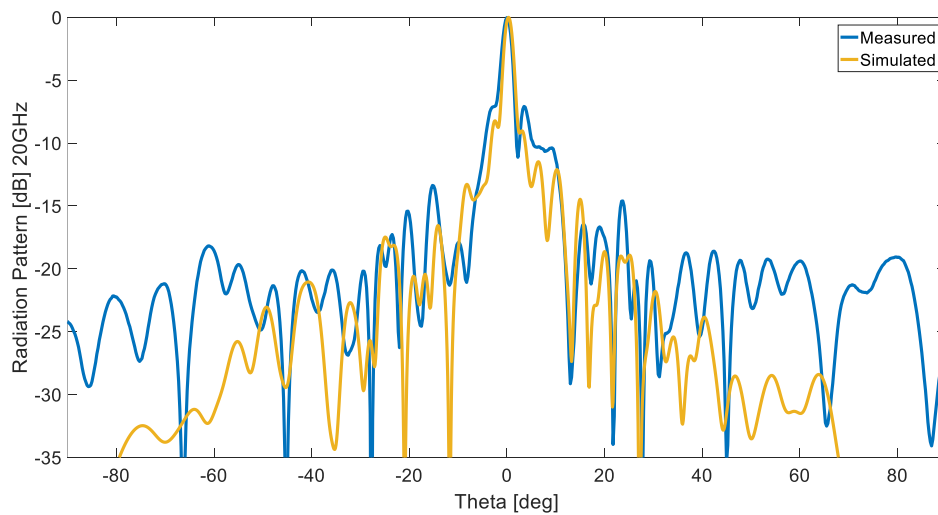
Fig. 4.14 - Comparison between measured and simulated radiation pattern at center band (20GHz)

The discrepancies between simulated and measured patterns are mainly due to the manufacturing errors which may be also seen in figure 4.14. The most evident is the distance between the stripline panels which are not the

one prescribed and present gaps too large. A check of the metallic supports has also shown that they are not of the prescribed length and they have not the inclination specified to the manufacturer. These discrepancies strongly affect the radiation pattern and the antenna efficiency. So, no further measurements have been done and a new prototype will be realized and measured.

5. Transmitarray antenna for Radar Automotive applications

5.1.   Transmitarray theoretical model

Thanks to their spatial feeding technique, reflectarray antennas and transmitarray represent a very attractive solutions compared to the traditional phased arrays. In particular, transmitarray antennas have excellent capabilities for beam steering and could be employed in a number of telecommunications systems. The behaviours of transmitarray are similar to reflectarray in fact the phase distribution along the aperture plane of the transmitarray must be equal for every possible radiation path in order to produce a pencil beam. The main difference between these two system is that in a reflectarray all of the incident power will be reflected on the surface while in a transmitarray most of the power will be transmitted (Fig. 5.1.
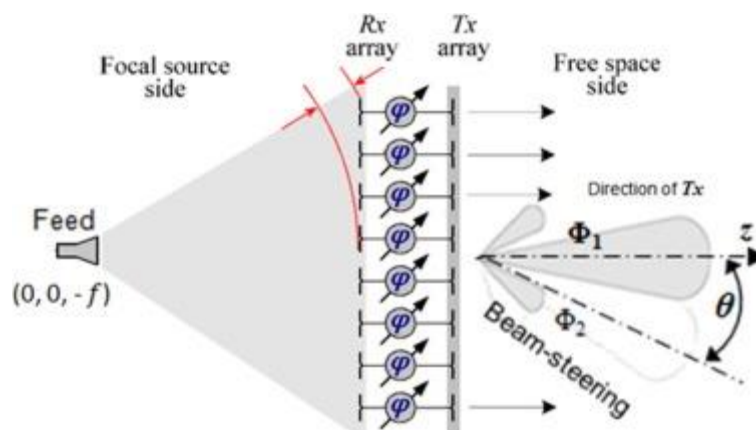
Fig. 5.1 - Theoretical structure of Transmitarray antenna [20]

A transmitarray uses the antenna elements on its surface to re-phase the incoming spherical wave and the re-transmit the signal as a plane wave in a given direction. The amount of phase adjustment needed at each antenna elements depends on the phase delay of the incident way has accumulated travelling between the feed and the transmittarray surface.

In this chapter, a new configuration of transmitarray in package will be introduced. The proposed configuration is designed for short range automotive radar applications operating at 77 GHz. The transmitarray is designed to be fully integrated in a standard QFN package in place of its top cover. The proposed transmitarray can be employed to focus the beam of an on-chip antenna without adding any additional structural element (as it would be in the case of dielectric lenses) and without requiring any vertical transition.

5.2. State of the art

5.2.1. Transmitarray antenna configurations

Transmitarray antennas can be implemented using different approaches which reflect the configuration employed to control the phase between the two transmitarray sides. In the following, the four most common configurations are briefly described.

5.2.2. Discrete Lens Arrays

The discrete lens arrays are the most conventional implementation of transmitarray antennas. They consist of two back-to back antenna elements interconnected with a transmission line which provides the required phased delay. One side is called the radiating side and generates the far-field pattern of the lens while the other side, called the deed side, faces the feed. The transmission lines are of different electrical lengths: the larger delay at the central element with respect to the external ones mimics an optical lens, ticker in the centre and thinner in the periphery [21]. The position of the elements on the radiating side sets the feature of the far field radiation pattern; the spacing of elements is chosen to satisfy the radiation specifications such as grating lobes, side lobes and beam-width.

5.2.3. Antenna Filer Antenna (AFA)

Another configuration which can be adopted for the implementation of transmitarray antennas is based on so-called Antenna-Filter-Antennas (AFAs). An AFA is an integrated module composed of two microstrip patch antennas coupled to a sandwiched coplanar waveguide (CPW) resonant structure. It acts as a bandpass filter with two radiative ports [22]. Each AFA cell can be designed to work as a reconfigurable filter, where the input and the output are TX and RX antennas. The phase delay at the cell level can be controlled acting on a reconfigurable circuit which connects the two radiating elements. There are two types of reconfigurable AFA elements: the first one is based on slot antennas coupled to a stripline resonator controlled by an electronic mechanism that

permits to obtain variable phase responses (e.g. switches, varactors and phase shifters); the second class of AFAs produces variations of continuous phase by two varactor-loaded patch radiators coupled through a varactor-tuned slot [23]. In Fig. 5.2 it is shown a case where the radiative elements in the AFA are two back-to-back microstrip patch antennas. The middle resonant structure is an ensemble of CPW resonators fabricated in the common ground plane. The coupling between the antennas and the CPW resonators is achieved through coupling slots in the CPW later to form a bandpass filter between the radiative ends[24].
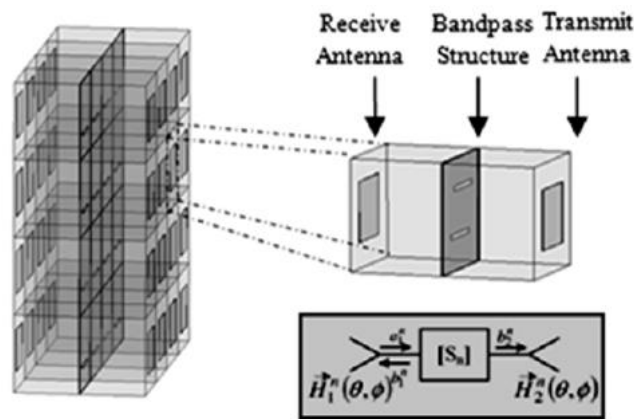
Fig. 5.2 - An antenna-filter-antenna array composed of patch antennas [25]

5.2.4. Multilayer Antenna Filter Antenna (MAFA)

Another approach which has been introduced for the implementation of transmitarray antennas is based on multilayer antenna filter antennas (MAFAs). The MAFA concept is an extension of the AFA concept, when multiple reconfigurable antennas are cascaded to form a space-based tunable beam-former. At variance of AFAs, MAFAs do not require a coupling resonant structure.

Indeed, they can be seen as a spatial filter where each layer is a resonator. When several layers are cascaded using a quarter-wavelength spacing, MAFAs act as a pass-band filter. As such, the in-band phase has a linear variation which can employed to control the phase of the transmitted field. Such structures are inspired by frequency selective surface (FSS) elements that are well known for their filtering characteristic at microwave, millimetre wave and infrared frequency. MAFAs can be implemented using cascading arrays of tuneable antennas exited by a feed horn; each MAFA layer consists of a dielectric slab having relative dielectric permittivity ε_r, thickness h and inter-layer distance d; the use of materials with higher dielectric permittivity can be important to reduce the inter-layer distance and the longitudinal length of MAFA array. The field propagates through all the layers and it is radiated into free space by the last layer; each radiating element in the array is a rectangular slot antenna. A general configuration of MAFA structure is shown in Fig. 5.3.
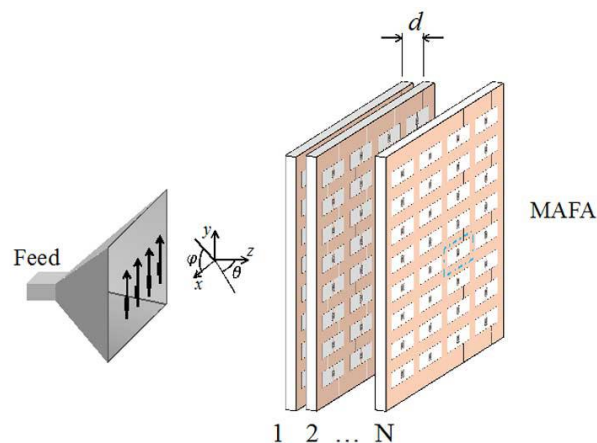
Fig. 5.3 - MAFA structure [26]

5.2.5. Frequency Selective Surface (FSS)

Frequency Selective Surfaces (FSSs) are a periodical structure, which exhibits different reflection and transmission properties as a function of frequency (Fig. 5.4); i.e. these structures resonate at a designed frequency and attain spectral selectivity. FSS structures can be divided in two categories based on the element geometry. To the first category belong substrates loaded with metallic patches, which are usually referred to as capacitive FSSs. These structures exhibit low-pass filter characteristics. The other type of FSS structure comprises arrays of apertures on a metallic screen, which normally act as an inductive FSSs exhibiting high-pass filter configurations.
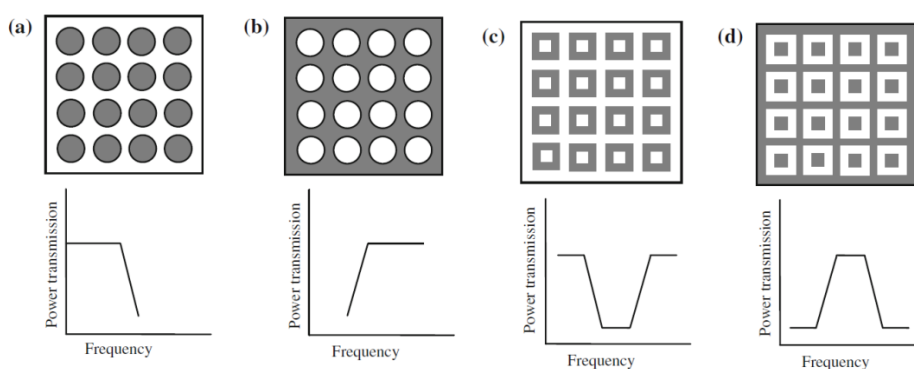
Fig. 5.4 - Typical FSS types and their frequency response characteristics [27]

The low-pass and high pass FSS structures are complementary surfaces and they can be combined to form four types of configurations. One characteristics of FSS is that the size of the resonant elements and their spacing are comparable to half wavelength or more at the frequencies of operations.

5.3.   Transmitarray antenna for radar automotive

The transmitarray antenna proposed in this chapter is conceived as a focusing element to be employed, in different parts of the car for short range automotive radar applications. The idea is to use the same type of radar chip and the same type of package for different applications (e.g. blind spot detection or park assistance) and in different areas around the car (e.g. bumpers or fenders). The transmitarray thus replaces the top cover of a standard QFN package and it can be employed to focus the beam of an on-chip antenna towards different directions as dictated by the application.

Two alternative solutions that might be used for the application at hand. The most natural solution to have a focused beam is to use a dielectric lens on top of the MMIC as shown in Fig. 5.5. Although lens antennas can provide the required focusing effect, the control of the beam direction is more complex. Moreover, the direct integration in the package can be also a critical limiting effect whereas the transmitarray achieves the focusing effect by simply replacing the top-cover of standard QFN packages (Fig. 5.7)
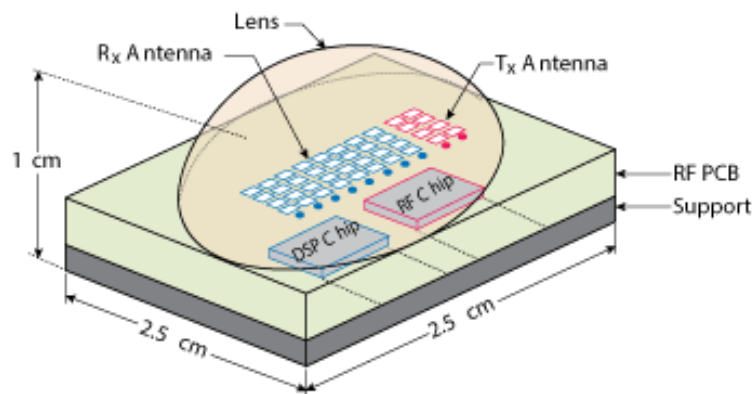
Fig. 5.5 - Chip on board integration [28]
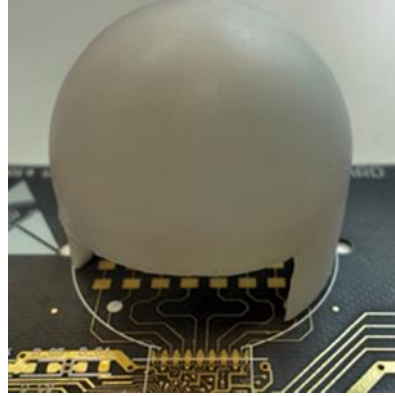
Fig. 5.6 - Lens antenna on chip [29]
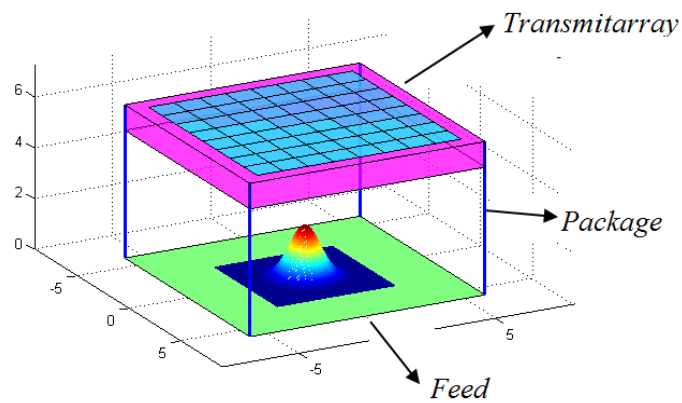
Fig. 5.7 – Concept of transmitarray integrations in package

Therefore, transmitarray antennas can provide a valid solution, easily integrable in standard components with high efficiency and low cost. Moreover, they can be simply designed to point the beam in a different direction by simply redesigning the radiating elements.

A transmitarray can be thought as a planar array of cells in the xy plane, each cell having a size d_x x d_y and being the centre of the m-th cell equal to (x_m, y_m). In a transmitarray structure, the feeding antenna is usually placed quite near to the structure, in terms of wavelength (< 5λ). For this reason, the arising wave front in

the structure is spherical being the sphere centre in the feeding antenna phase centre located in as shown in Fig. 5.8.
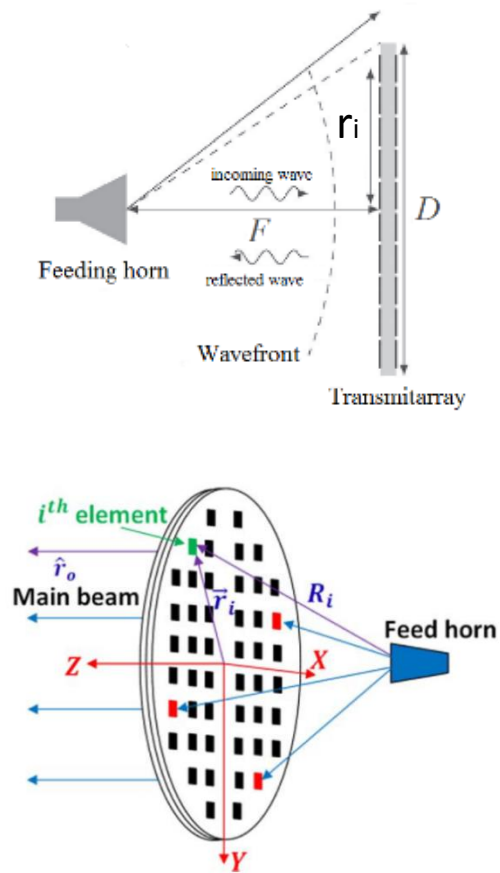
Fig. 5.8 - Transmitarray structure

Let's assume that the transmitarray is configured to point the scattered beam direction in a direction given by $\hat{r}_o$ as depicted in Fig. 5.8. The total phase of the scattered field at each transmitarray element (φ_i), corresponds to the phase shift produced by each element (φ_i) and the phase shift due the propagation from the feed. It can be written as:

$$\varphi = -k_o\sqrt{F^2 + r_i^2} + \varphi_i$$

$$\varphi = -k_o R_i + \varphi_i$$

where R_i is the distance from the phase center of the feed to the resonator whose position on the array is determined by a set of (x, y) coordinates. The free space propagation constant is denoted by k_o and φ_i is the phase shift produced by each transmitarray element. This phase shift should be chosen so as to restitute a planar phase front in the pointing direction. It should therefore compensate for the several phase delays introduced by the individual path differences, such that the fields are all in phase at any plane perpendicular to the desired direction of transmission (i.e. the desired phase front).

According to Fig. 5.8, the phase error correction needed at each cell is determined by the difference in cell distance to feeding horn, defined as follow

$$\Delta r = \sqrt{F^2 + r_i{}^2} - F$$

The phase error correction is fundamental in transmitarray design. Assuming a spherical phase front generated in the feed phase centre, each transmitarray element is classified into concentric rings around the central transmitarray point; all the cells in the same ring receive the incident wave with the same phase and, therefore, they have to experience the same phase correction (Fig. 5.9).
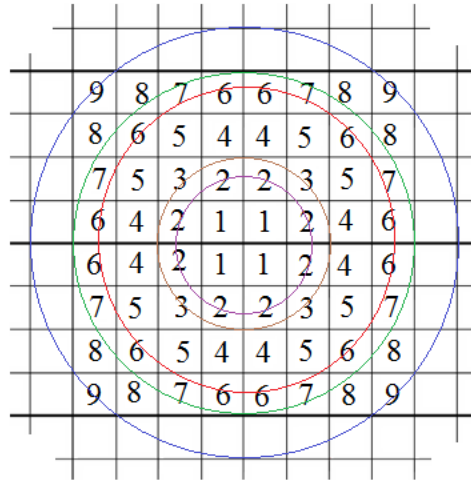
Fig. 5.9 - Ring cell classification around the transmitarray central point

The basic theory of operation of transmitarray is to collimate the feed spherical electromagnetic incident wave into planar wave front at the radiating aperture. The electromagnetic wave coming from the feed antenna is incident on each element in the array with a phase difference related to the distance between the elements. These phase differences should be compensated by tuning the phase of each element at a specific value. The required transmission phase value of each element φi should satisfy the following equation:

$$\varphi_i = -k_0 \Delta r + 2n\pi, \qquad n = 0,1,2,..N$$

Where φi is the required phase of an individual cell, Δr has is the distance between the i-cell and the feed and k_0 is the wavenumber in free space.

The required phase compensation value of the unit cell depends on the incident wave angle and its location on the surface of the array. Fig. 5.10 shows a general case of the required phase shift for each cell as a function of its position.
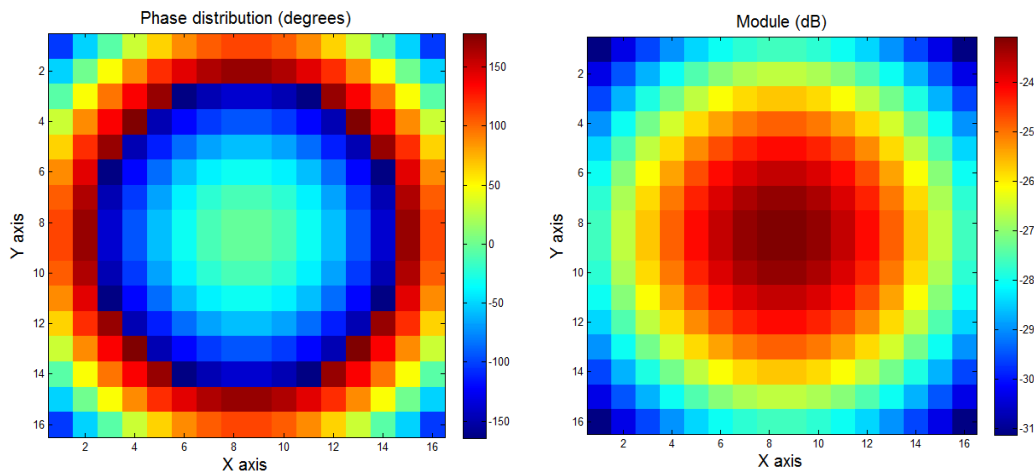
Fig. 5.10 - Field distribution in the transmitarray

In order to estimate the efficiency of transmitarray antenna is important to evaluate the power budget of the overall system. The transmitarray model is composed by four parts in cascade namely:

- Focal Source

- Intermediate space between the focal source and the Rx array

- The unit cells

- The free space regions

Ideal configurations with lossless and matched unit cells are considered to identify the ultimate performance of such transmitarray. To compute the transmitarray efficiency four parameters are defined: P_1 is the total input power of the focal source, P_2 is the total power radiated by focal source, P_3 is the incident power collected by the Rx-side of the array and P_4 is the power radiated by the Tx side of the array (Fig. 5.11). The antenna efficiency is defined as:

$$\eta = \frac{P_4}{P_1} = \eta_{FS}\eta_{SO}\eta_{IL}$$

Where, $\eta_{FS} = P1/P2$ is the realized efficiency of the focal array, $\eta_{SO} = P3/P2$ is the spillover efficiency and $\eta_{IL} = P4/P2$ stands for the insertion loss of the unit cells.
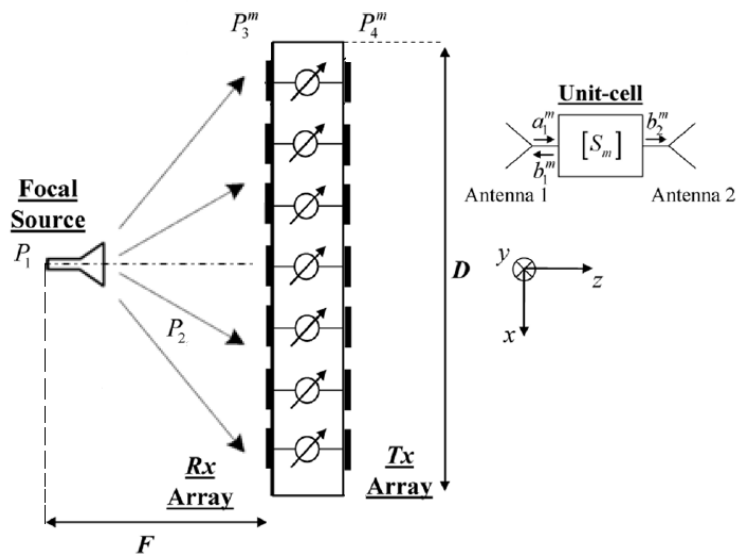
Fig. 5.11 - Schematic view and power budget of a transmitarray

Spillover is the fraction of power lost due to the energy from the feed spilling over around the edges of the surface. A diagram is shown in Fig. 5.12.The spillover efficiency, η_{SO} is therefore the fraction of total power that is captured and collimated by the surface. It can be expressed as

$$\eta_{SO} = \frac{Power\ captured\ by\ surface}{Total\ power\ radiated\ by\ feed}$$
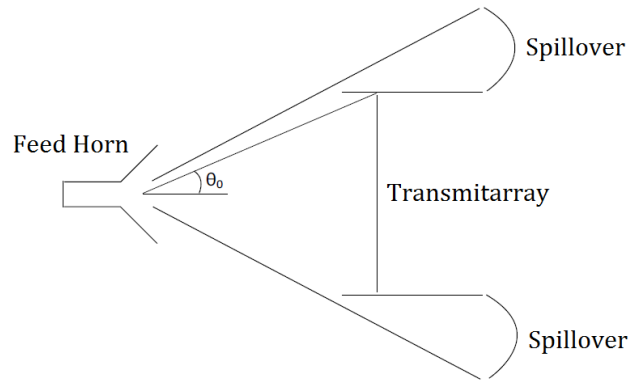
Fig. 5.12 - Graphical view of Spillover Efficiency.

5.3.1. Transmitarray efficiency performance

In order to optimize the directivity and spillover efficiency it is necessary to study the behavior of transmitarray with the variation of the design parameters (F and D), as well as the number of elements and the distance between them. To model the system is considered an ideal horn antenna, where it is assumed that the behavior is given by $cos^q\theta$ function with a parameter $q = 4$.

In Fig. 5.13 are shown the results that have been obtained for a spacing between elements equal to $\lambda/3$. In this case, it is noted that when the transmitarray moves away from the feed antenna, the spillover efficiency decrease because the maximum angle of the power feeder is reduced and more energy radiated is lost due to the limits of the surface. In the other hand, the directivity increases when the parameter F/D increase until a uniform amplitude value.

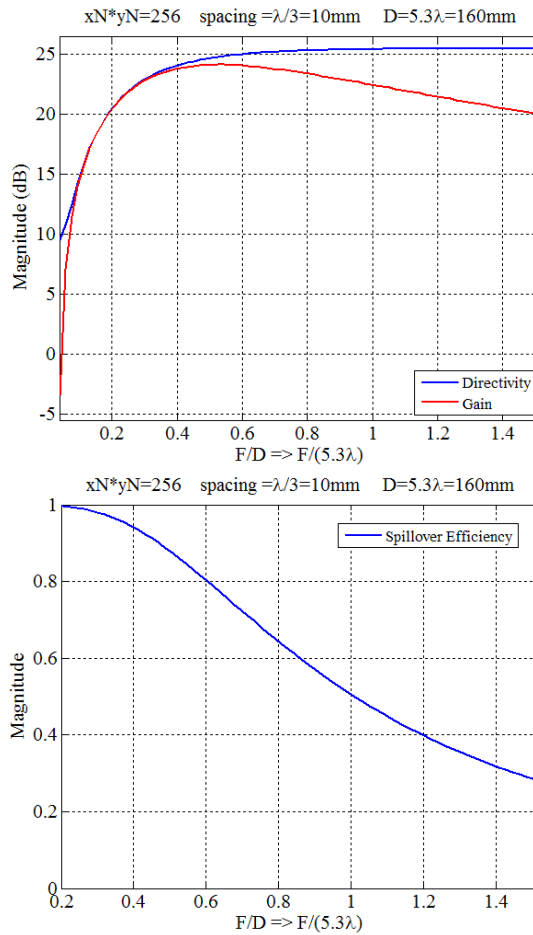*Fig. 5.13 - Results for the study of different values of the parameter F/D*

The analysis of the performance of transmitarrays can be performed for different values of q in the model of feed that has been taken as it mentioned above ($cos^q\theta$). In this case, the feeder will be more steering as the value q increase, as shown in Fig. 5.14.
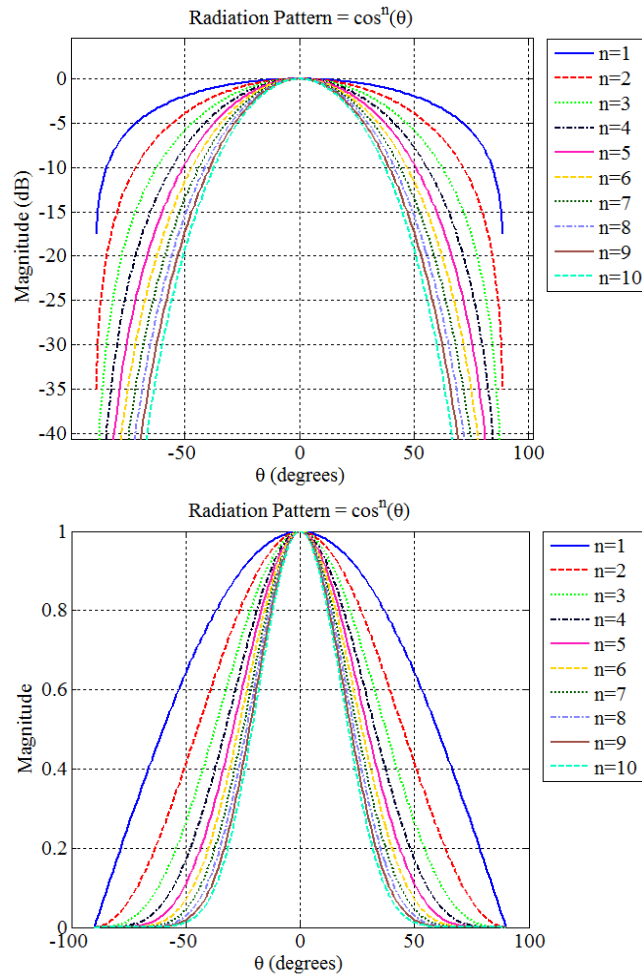
Fig. 5.14 - Radiation pattern with the model $\cos^n \theta$

Fig. 5.15 shows the directivity and efficiency result obtained with different value of the *n* parameter. As is can be observed, by increasing the directivity of the feed, the maximum value of the transmitarray directivity is reached for larger values of F/D. Likewise, it is possible to observe that the behavior of spillover efficiency where the value is closer to 100 % when a feed with higher directivity is used. This happens because the power is concentrated in the center of transmitarray and less power is lost outside the aperture.
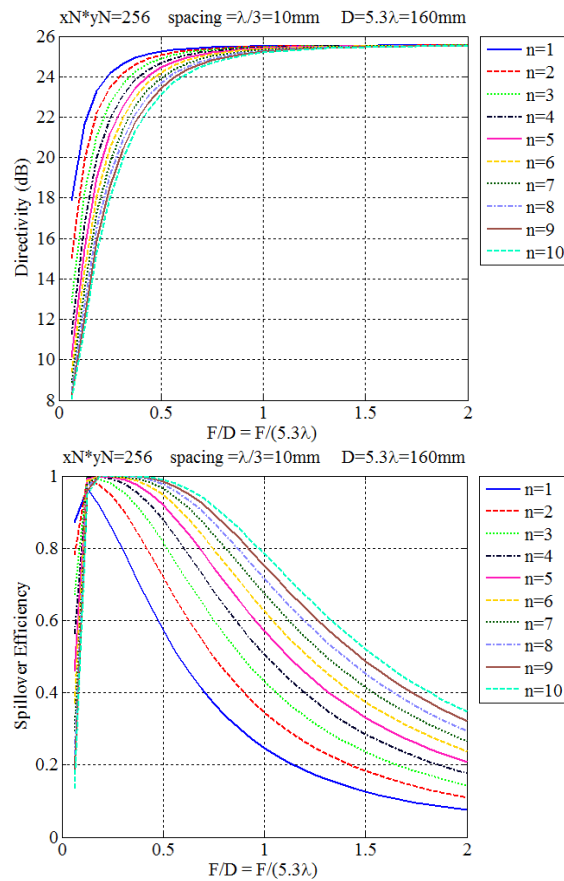
Fig. 5.15 - Results obtained for directivity and spillover efficiency,
depending of n

The behavior of directivity for different values of n is similar, i.e. the directivity increases as a function of the focal distance (F/D) and converges toward a maximum value for large focal distances corresponding to a uniform aperture illumination of the array. Thanks to the results showed in Fig. 5.15, it is possible to evaluate the efficiency when the ratio between F and D is very low. In order to obtain a compact structure for the transmitarray with an high efficiency, a value of $F/D = 0.5$ has been chosen.

Another variable which can affect the transmitarray behavior is the cell size for a given F/D value. The influence of the element spacing on the transmitarray directivity is represented in Fig. 5.16. As expected, minimizing the element

spacing is desirable in order to collect the radiation from the feeding source with maximum efficiency.
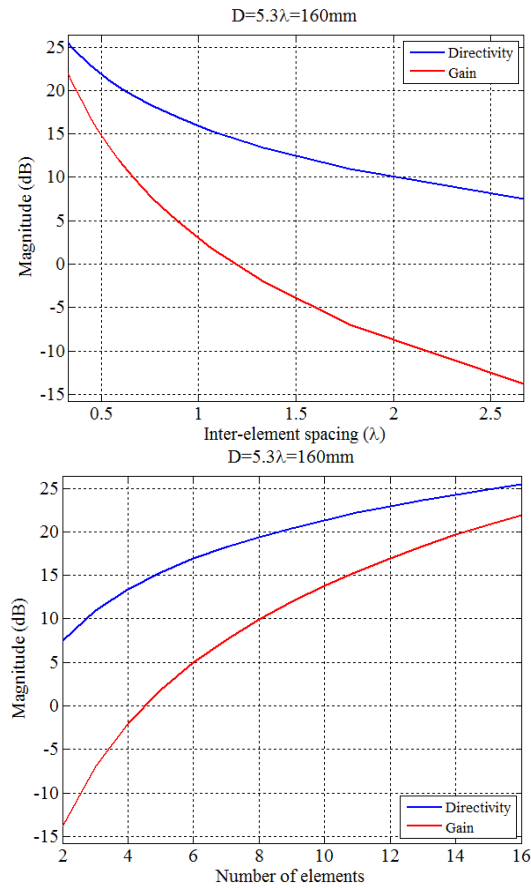
Fig. 5.16 - Impact of element spacing in the directivity

To perform the proposed analysis, the inter-element spacing has been varied from $\lambda/3$ to $2.5\,\lambda$. As the separation between the cells increases, the number of the elements in the transmitarray decreases while the directivity increases when the number of elements increases (Fig. 5.16). This directivity variation is not the same, i.e. there is no linear relationship between the directivity and the number of elements.

5.3.2. Designing procedure of the transmitarray antenna

For the design of the transmitarray, it is very important to choice the unit cell which in turn affects also the number of elements to be used in the radiating surface. For the case at hand, the unit cells of the transmitarray are realized utilizing a a stacked patches show in Fig. 5.17. Two couples of stacked square patches are printed on the receiveing and transmiting surface of the transmitarray. A slot couples the transmitting and the receiving section while the angle of the transmission coefficient is controlled by the size of the patches, s. Fig. 5.18 shows the behaviour of this unit cell in terms of phase and amplitude of the transmission coefficient. As it can be observed, the phase is relatively stable even when the incidence angle is varied from the broadside direction. This type of cell provides a phase range of about 300° when the angle of incidence remains under 60°.
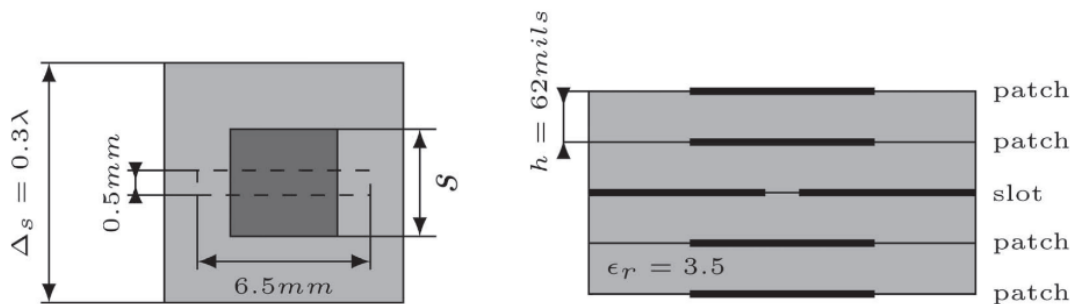
Fig. 5.17 - Scheme of the unit cell of transmitarray antenna
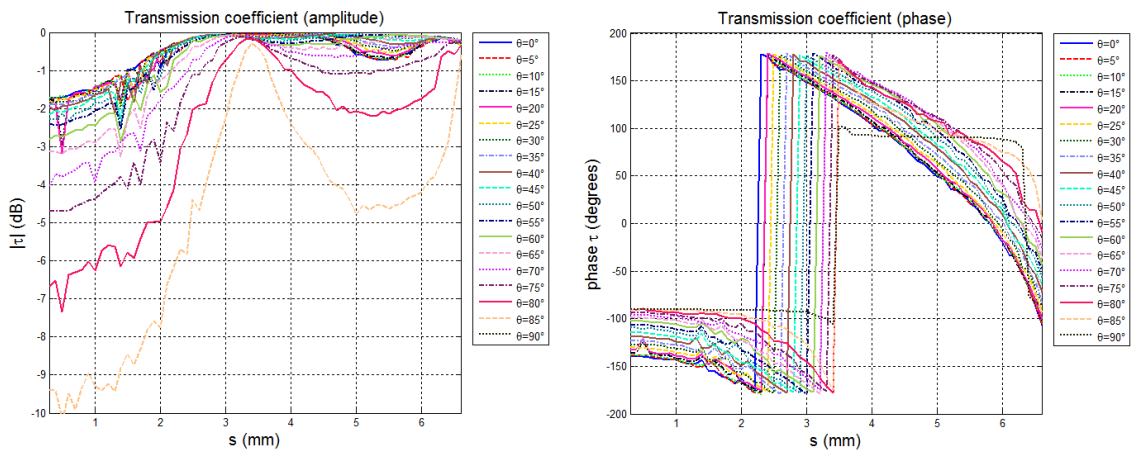
Fig. 5.18 - Transmission coefficient as a function of patch side: Amplitude and Phase

The unit cell shown in Fig. 5.17 has a size of 1.3mm which corresponds to λ/3 at 77GHz. The transmitarray will be used as a cover of standard QFN packages. For the case at hand, the package M-QFN80T was taken as a reference. This component, whose dimensions are shown in Fig. 5.19, leaves a square area of $12mm \, x \, 12mm$ available for the integration of the transmitarray. The focal distance F, can be controlled using a standard plastic support.
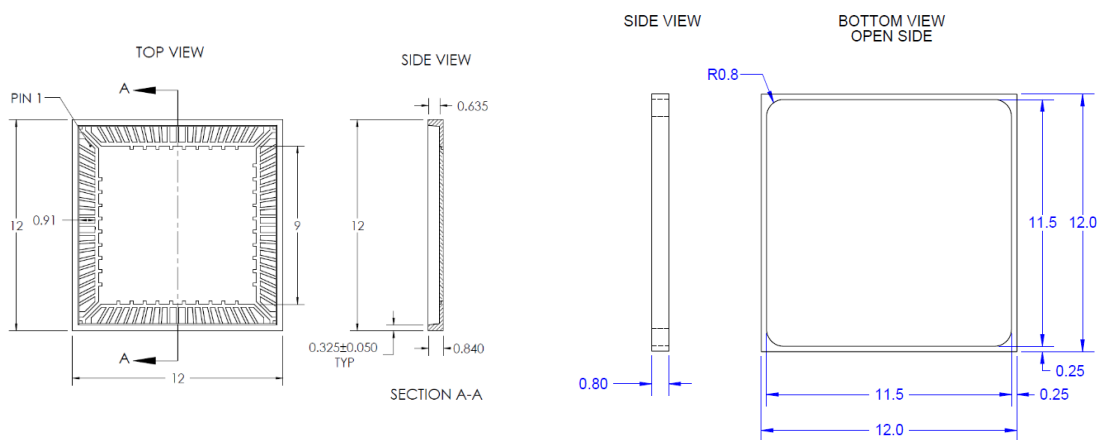
Fig. 5.19 - Footprint of the M-QFN80T.5 package

Considering the area available on top of the package, a transmitarray with $8 \, x \, 8 \, elements$ has been designed.

Fig. 5.20 - A generic scheme of the chosen transmitarray

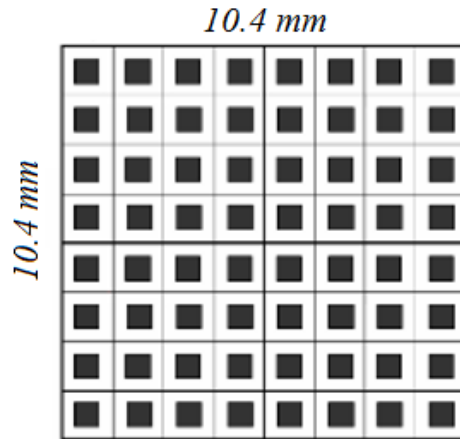Based on the available spacers for the QFN top cover, the focal distance has been fixed to $F = 0.5\lambda$ corresponding to a distance of 1.98mm at 77GHz (Fig. 5.21).
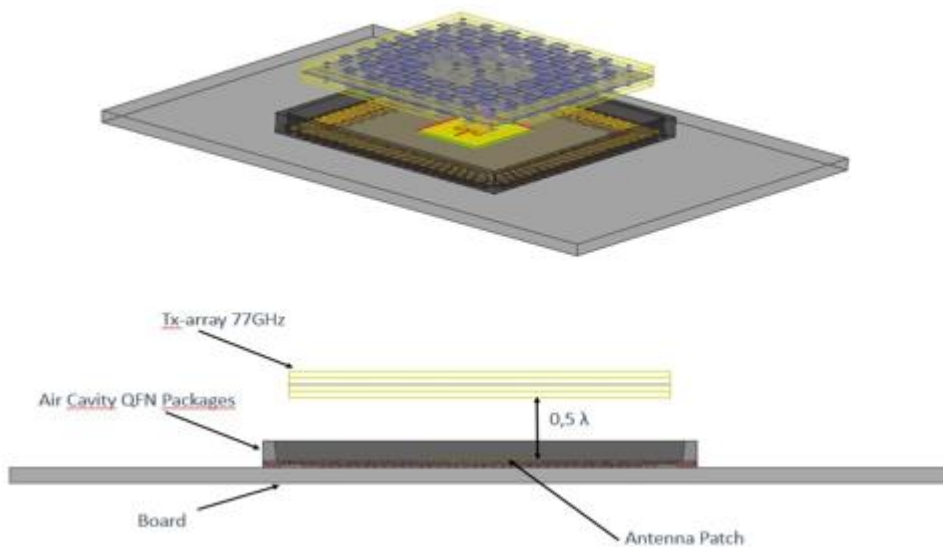

Fig. 5.21 - Section view of the transmitarray at 77GHz

In the final demo, the transmitarray antenna will be fed directly by the MMIC using an on-chip antenna. However, to simplify the experimental phase, a standard PCB patch antenna has been designed. This elements, shown in Fig. 5.21, will be integrated in the package through bondwires. In order to limit the length of the bondwires, the patch has been designed with a microstrip line which connects the radiator, located in the centre of the package, towards the package periphery close to its pads. Unfortunately, this configuration along with the surface waves launched in the dielectric causes a distortion of the radiation pattern which can observed in Fig. 5.23. Due to this constriction, the length of the line feed of the patch have to be increased (Fig. 5.22). The high length of the line feed, the high dimensions of the dielectric and a low value of dielectric thickness generates the problem of the surface wave propagation that cause undesirable effect in the radiation pattern of the patch antenna.

The non-symmetric radiation pattern of the patch antenna (Fig. 5.23) causes a non-correct illumination of the transmitarray, as it can be observed from Fig. 5.24.
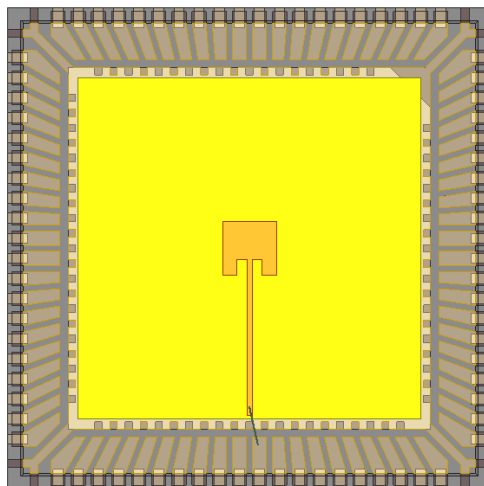
Fig. 5.22 - Integration between QFN package and patch antenna
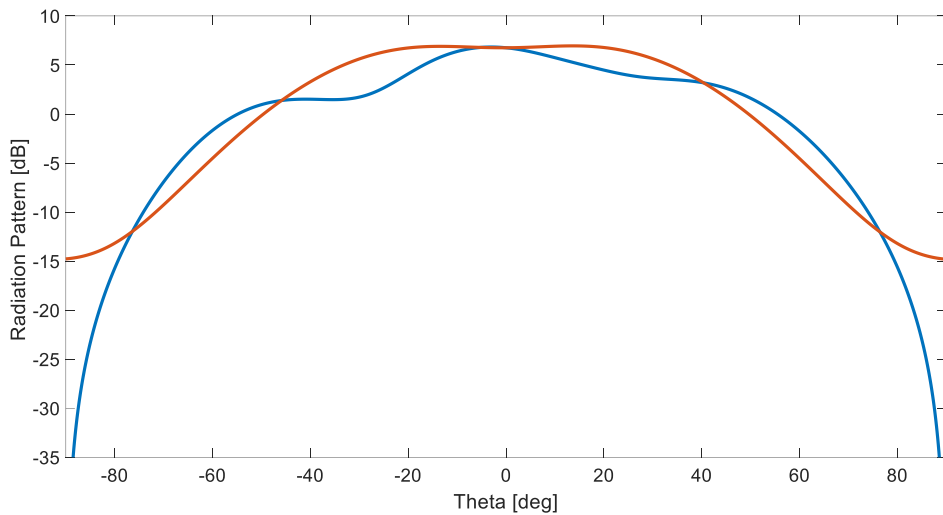
Fig. 5.23 - Surface wave effect on the radiation pattern of the patch at 77GHz
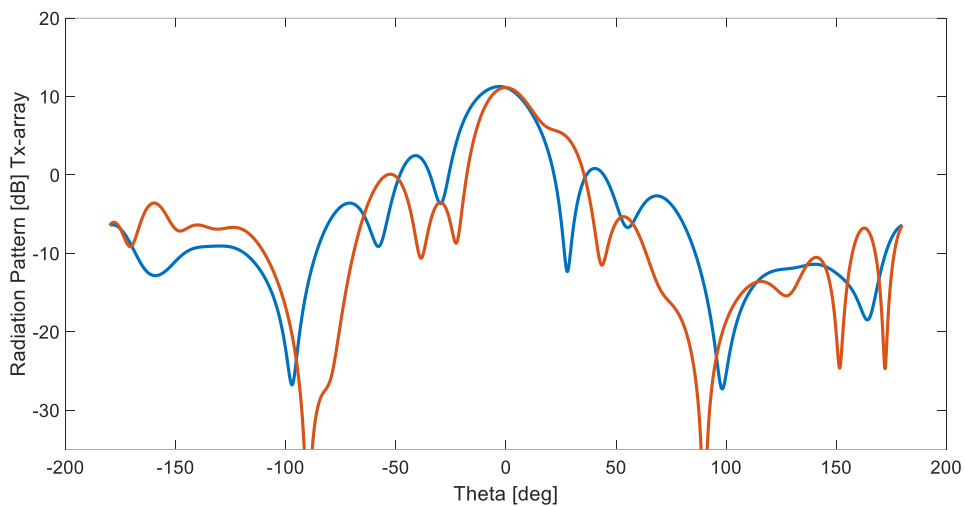
Fig. 5.24 - Surface wave effect on the radiation pattern of the Transmitarray at 77GHz

To avoid this problem it was necessary to surround the patch with an EBG (Electromagnetic Band Gap) structure [30]. EBGs are periodic structures which interact with electromagnetic waves in different ways. In particular, their use is proposes in this particular configuration with the intent to inhibit the propagation of surface waves in the dielectric thus avoiding the issues shown in Fig. 5.23 and

Fig. 5.24. The mushroom type EBG configuration has been designed to have a bandgap in the 77GHz band. The mushroom cell has been designed with Ansoft-HFSS using periodic boundary conditions on the unit cell and an impedance boundary on the top. Fig. 5.25 shows the geometry of the structure.
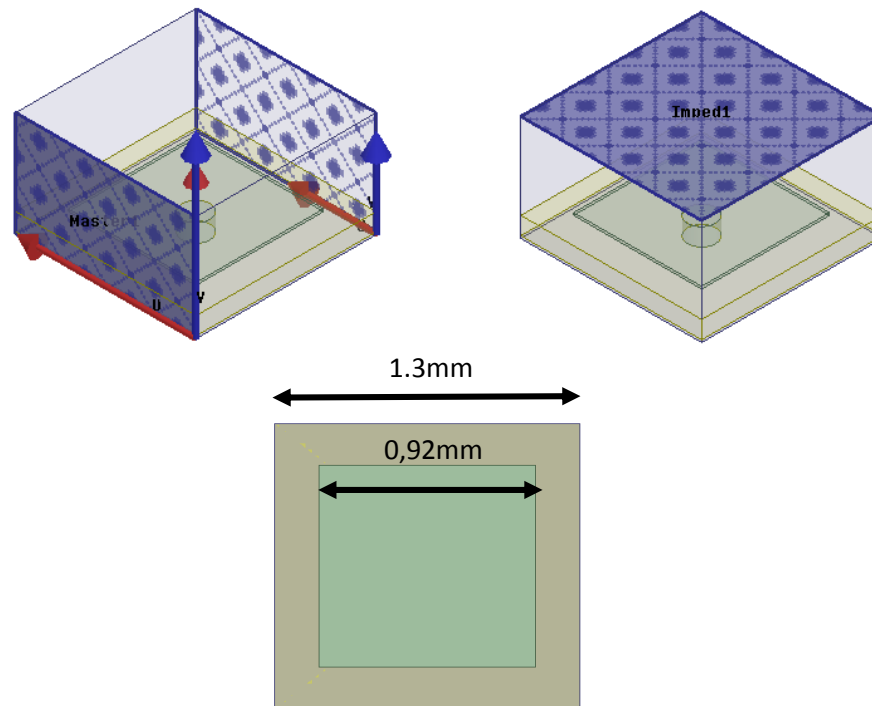
Fig. 5.25 - Structure of the Electromagnetic Band Gap
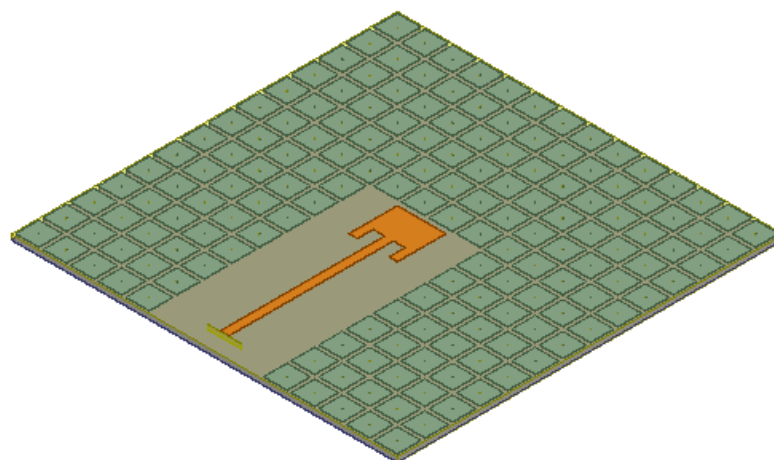
Fig. 5.26 - Patch antenna with Mushroom EBG
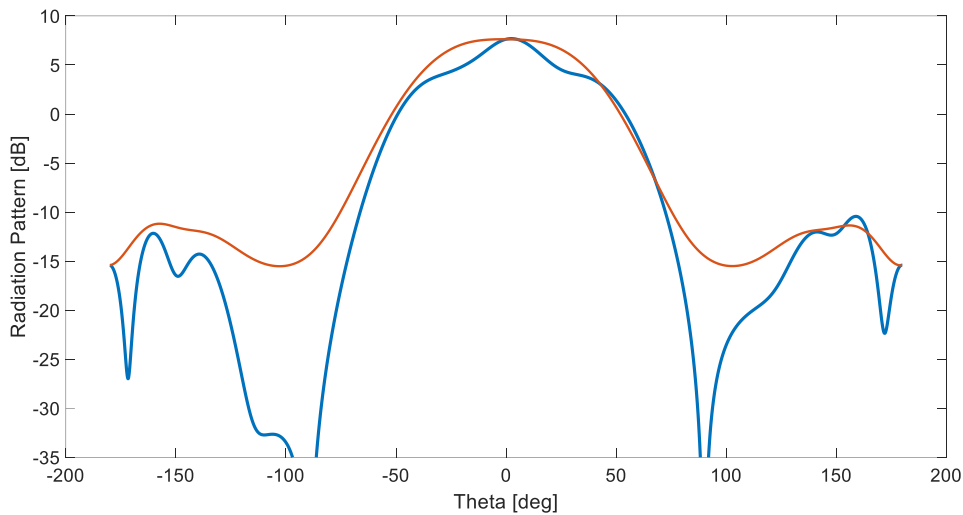
Fig. 5.27 - Radiation pattern of the Patch with EBG at 77GHz

As it can be seen in Fig. 5.27, the EBG structure provides a focusing effect in the patch radiation pattern with a gain of 7.5dBi. The patch antenna shown in Fig. 5.26 has been employed to feed the transmitarray as shown in in Fig. 5.28. The transmitarray radiation pattern, shown in Fig. 5.29, has a half-power beamwidth of 17degree and a maximum gain of 17.6dBi thus resulting in a radiation efficiency of approximately 70%.
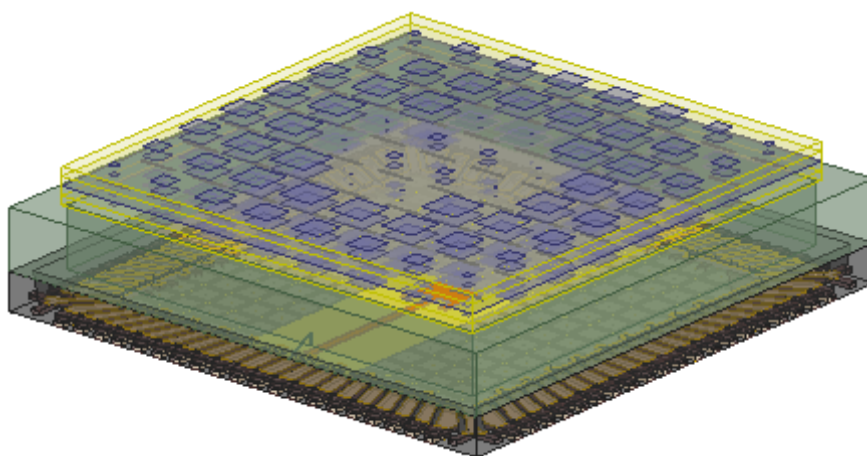
Fig. 5.28 - Transmitarray antenna with a QFN package at 77GHz
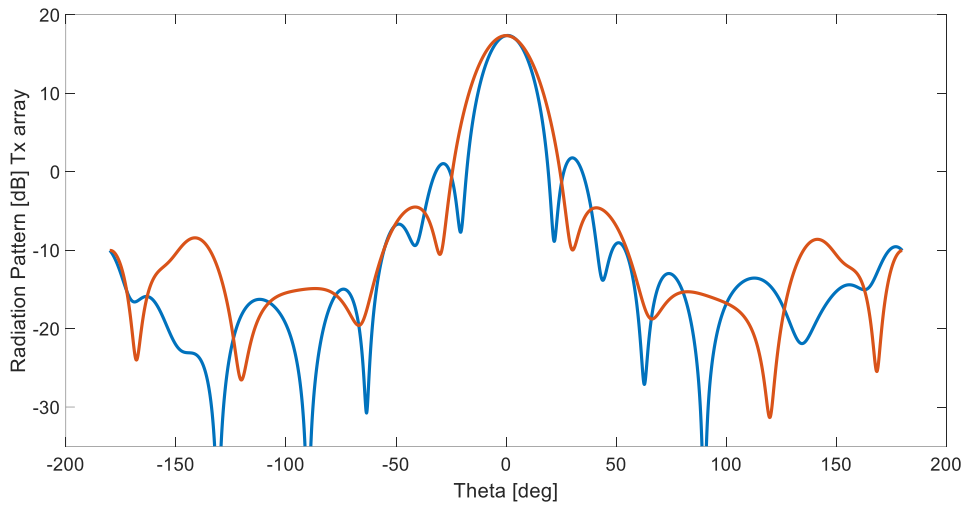
Fig. 5.29 - Radiation pattern of the Tx array feeding by patch antenna with EBG at 77GHz

Conclusions and future work

In this thesis four antenna designs have presented. The Dual Band Dual Polarized antenna presented in this thesis was an extension of the work of my Master Thesis. The prototype has been realized and only partially measured. The results obtained are quite promising. If they will be confirmed the proposed design will represent the first example of a dual band dual polarized radiating element operating for satellite applications at Ka band.

The second antenna was the Cylindrical Reflector Parabolic Antenna. This terminal represent a good solution both for the backhaul point of the 5G architecture (Q-V bands) and for man transportable antenna (Ka band). The measured results were in good agreement with the simulations. The antenna has good measured characteristics as it is both efficient and complying with power density masks. The antenna promises to become a real solution to be marketed but it requires a major effort to reduce weight to make it suitable for man transportable terminals. Exploiting the parallel plate feeding structure used for the cylindrical reflector antenna, a segmented reflectarray has been invesitgated. This solution has been designed to create a more compact terminal with a larger aperture. Inaccuracies in manufacturing prevented an exhaustive measurements campaign. However, the limited results shown are encouraging. The antenna is single band, but dual band can obtained designing dual or wide band radiators.

Finally, a transmittarray for automotive radar applications has been presented. The overall structure has been realized but not measured yet. If it will show a good agreement with the simulated results, a possible future work could be the design of a feed in order to obtain a transmitarray with a steerable beam able to recognize different target in a restricted range.

Bibliografia

[1] T. Shroyer, "Satcom-on-the-move why one size doesn't fit all," in *MILCOM 2012 - 2012 IEEE Military Communications Conference*, 2012, pp. 1–6.

[2] F. Khan, *LTE for 4G Mobile Broadband: Air Interface Technologies and Performance*, 1 edition. Cambridge, UK ; New York: Cambridge University Press, 2009.

[3] A. V. Shishlov, "Vehicular antennas for satellite communications," in *2011 VIII International Conference on Antenna Theory and Techniques*, 2011, pp. 34–39.

[4] J. Remez, A. Segal, and R. Shansi, "Dual-polarized wideband widescan multibeam antenna system from tapered slotline elements array," *IEEE Antennas Wirel. Propag. Lett.*, vol. 4, pp. 293–296, 2005.

[5] D. Cavallo *et al.*, "Ku-band dual-polarized array of connected dipoles for satcom terminals: Theory and hardware validation," in *2013 7th European Conference on Antennas and Propagation (EuCAP)*, 2013, pp. 459–460.

[6] F. Greco, G. Amendola, E. Arnieri, L. Boccia, and A. I. Sandhu, "A dual-band, dual-polarized array element for Ka band satcom on the move terminals," in *The 8th European Conference on Antennas and Propagation (EuCAP 2014)*, 2014, pp. 2432–2435.

[7] V. Dyadyuk, Y. J. Guo, and J. D. Bunton, "Multi-gigabit wireless communication technology in the E-band," in *2009 1st International Conference on Wireless Communication, Vehicular Technology, Information Theory and Aerospace Electronic Systems Technology*, 2009, pp. 137–141.

[8] C. Granet, "Designing axially symmetric Cassegrain or Gregorian dual-reflector antennas from combinations of prescribed geometric parameters," *IEEE Antennas Propag. Mag.*, vol. 40, no. 2, pp. 76–82, Apr. 1998.

[9] P. J. B. Clarricoats and G. T. Poulton, "High-efficiency microwave reflector antennas - A review," *Proc. IEEE*, vol. 65, no. 10, pp. 1470–1504, Oct. 1977.

[10] M. Narasimhan, V. Anantharam, and K. Prasad, "A note on the shaping of dual reflector antennas," *IEEE Trans. Antennas Propag.*, vol. 29, no. 3, pp. 551–552, May 1981.

[11] C. Granet, "A simple procedure for the design of classical displaced-axis dual-reflector antennas using a set of geometric parameters," *IEEE Antennas Propag. Mag.*, vol. 41, no. 6, pp. 64–72, Dec. 1999.

[12] P. S. Kildal, "A small dipole-fed resonant reflector antenna with high efficiency, low cross polarization, and low sidelobes," *IEEE Trans. Antennas Propag.*, vol. 33, no. 12, pp. 1386–1391, Dec. 1985.

[13] A. Moldsvor and P. S. Kildal, "Systematic approach to control feed scattering and multiple reflections in symmetrical primary-fed reflector antennas," *Antennas Propag. IEE Proc. H - Microw.*, vol. 139, no. 1, pp. 65–71, Feb. 1992.

[14] J. Yang and P.-S. Kildal, "Gaussian vertex plate improves return loss and far-out sidelobes in prime-focus reflector antennas," *Microw. Opt. Technol. Lett.*, vol. 21, no. 2, pp. 125–129, Apr. 1999.

[15] R. E. Munson, H. A. Haddad, and J. W. Hanlen, "Microstrip reflectarray for satellite communication and radar cross-section enhancement or reduction," US4684952 A, 04-Aug-1987.

[16] D. M. Pozar, S. D. Targonski, and H. D. Syrigos, "Design of millimeter wave microstrip reflectarrays," *IEEE Trans. Antennas Propag.*, vol. 45, no. 2, pp. 287–296, Feb. 1997.

[17] J. Huang and R. J. Pogorzelski, "A Ka-band microstrip reflectarray with elements having variable rotation angles," *IEEE Trans. Antennas Propag.*, vol. 46, no. 5, pp. 650–656, May 1998.

[18] D. M. Pozar and T. A. Metzler, "Analysis of a reflectarray antenna using microstrip patches of variable size," *Electron. Lett.*, vol. 29, no. 8, pp. 657–658, Apr. 1993.

[19] A. Clemente, L. Dussopt, R. Sauleau, P. Potier, and P. Pouliguen, "Focal Distance Reduction of Transmit-Array Antennas Using Multiple Feeds," *IEEE Antennas Wirel. Propag. Lett.*, vol. 11, pp. 1311–1314, 2012.

[20] "High-Efficiency Wideband Transmit-array Antenna with Linear Polarization in Q-Band," *ResearchGate*.

[21] "Multibeam Spatially-Fed Antenna Arrays with Amplitude-Controlled Beam Steering (PDF Download Available)," *ResearchGate*.

[22] A. Abbaspour-Tamijani, K. Sarabandi, and G. M. Rebeiz, "Antenna-filter-antenna arrays as a class of bandpass frequency-selective surfaces," *IEEE Trans. Microw. Theory Tech.*, vol. 52, no. 8, pp. 1781–1789, Aug. 2004.

[23] A. Abbaspour-Tamijani, K. Sarabandi, and G. M. Rebeiz, "A millimetre-wave bandpass filter-lens array," *Antennas Propag. IET Microw.*, vol. 1, no. 2, pp. 388–395, Apr. 2007.

[24] ". An array of antenna-filter-antenna modules as a bandpass... - Figure 1 of 2." [Online]. Available: https://www.researchgate.net/figure/283582414_fig1_Fig-1-An-array-of-antenna-filter-antenna-modules-as-a-bandpass-frequency-selective. [Accessed: 02-Feb-2017].

[25] "Bandpass Antenna-Filter-Antenna Arrays for Millimeter-Wave Filtering Applications (PDF Download Available)," *ResearchGate*.

[26] L. Boccia, I. Russo, G. Amendola, and G. D. Massa, "Multilayer Antenna-Filter Antenna for Beam-Steering Transmit-Array Applications," *IEEE Trans. Microw. Theory Tech.*, vol. 60, no. 7, pp. 2287–2300, Jul. 2012.

[27] R. Mittra, C. H. Chan, and T. Cwik, "Techniques for analyzing frequency selective surfaces-a review," *Proc. IEEE*, vol. 76, no. 12, pp. 1593–1615, Dec. 1988.

[28] I. D. Robertson, S. Lucyszyn, and I. of E. Engineers, *RFIC and MMIC Design and Technology*. IET, 2001.

[29] J. du Preez and S. Sinha, *Millimeter-Wave Antennas: Configurations and Applications*. Springer, 2016.

[30] S. D. Assimonis, T. V. Yioultsis, and C. S. Antonopoulos, "Computational Investigation and Design of Planar EBG Structures for Coupling Reduction in Antenna Applications," *IEEE Trans. Magn.*, vol. 48, no. 2, pp. 771–774, Feb. 2012.